

11 Radiation Shielding and Radiological Protection

J. Kenneth Shultis · Richard E. Faw

Department of Mechanical and Nuclear Engineering, Kansas
State University, Manhattan, KS, USA

jks@ksu.edu

fawre@triad.rr.com

1	<i>Radiation Fields and Sources</i>	1316
1.1	Radiation Field Variables	1317
1.1.1	Direction and Solid Angle Conventions	1317
1.1.2	Radiation Fluence	1318
1.1.3	Radiation Current or Net Flow	1319
1.1.4	Directional Properties of the Radiation Field	1320
1.1.5	Angular Properties of the Flow and Flow Rate	1320
1.2	Characterization of Radiation Sources	1321
1.2.1	General Considerations	1321
1.2.2	Neutron Sources	1322
1.2.3	Gamma-Ray Sources	1328
1.2.4	X-Ray Sources	1336
2	<i>Conversion of Fluence to Dose</i>	1339
2.1	Local Dosimetric Quantities	1340
2.1.1	Energy Imparted and Absorbed Dose	1340
2.1.2	Kerma	1341
2.1.3	Exposure	1341
2.1.4	Local Dose Equivalent Quantities	1342
2.2	Evaluation of Local Dose Conversion Coefficients	1345
2.2.1	Photon Kerma, Absorbed Dose, and Exposure	1345
2.2.2	Neutron Kerma and Absorbed Dose	1345
2.3	Phantom-Related Dosimetric Quantities	1346
2.3.1	Characterization of Ambient Radiation	1346
2.3.2	Dose Conversion Factors for Geometric Phantoms	1347
2.3.3	Dose Coefficients for Anthropomorphic Phantoms	1349
2.3.4	Comparison of Dose Conversion Coefficients	1352
3	<i>Basic Methods in Radiation Attenuation Calculations</i>	1353
3.1	The Point-Kernel Concept	1353
3.1.1	Exponential Attenuation	1354
3.1.2	Uncollided Dose from a Monoenergetic Point Source	1354
3.2	Uncollided Doses for Distributed Sources	1356
3.2.1	The Superposition Procedure	1356

3.2.2	Example Calculations for Distributed Sources	1356
4	<i>Photon Attenuation Calculations</i>	1359
4.1	The Photon Buildup-Factor Concept	1359
4.2	Isotropic, Monoenergetic Sources in Infinite Media	1360
4.3	Buildup Factors for Point and Plane Sources	1362
4.3.1	Empirical Approximations for Buildup Factors	1365
4.3.2	Point-Kernel Applications of Buildup Factors	1365
4.4	Buildup Factors for Heterogenous Media	1369
4.4.1	Boundary Effects in Finite Media	1369
4.4.2	Treatment of Stratified Media	1370
4.5	Broad-Beam Attenuation of Photons	1372
4.5.1	Attenuation Factors for Photon Beams	1372
4.5.2	Attenuation of Oblique Beams of Photons	1372
4.5.3	Attenuation Factors for X-Ray Beams	1373
4.5.4	The Half-Value Thickness	1376
4.6	Shield Heterogeneities	1376
4.6.1	Limiting Case for Small Discontinuities	1377
4.6.2	Small Randomly Distributed Discontinuities	1378
5	<i>Neutron Shielding</i>	1378
5.1	Neutron Versus Photon Calculations	1379
5.2	Fission Neutron Attenuation by Hydrogen	1379
5.3	Removal Cross Sections	1382
5.4	Extensions of the Removal Cross Section Model	1384
5.4.1	Effect of Hydrogen Following a Nonhydrogen Shield	1384
5.4.2	Homogenous Shields	1385
5.4.3	Energy-Dependent Removal Cross Sections	1386
5.5	Fast-Neutron Attenuation Without Hydrogen	1387
5.6	Intermediate and Thermal Fluences	1389
5.6.1	Diffusion Theory for Thermal Neutron Calculations	1389
5.6.2	Fermi Age Treatment for Thermal and Intermediate-Energy Neutrons	1391
5.6.3	Removal-Diffusion Techniques	1392
5.7	Capture-Gamma-Photon Attenuation	1394
5.8	Neutron Shielding with Concrete	1396
5.8.1	Concrete Slab Shields	1396
6	<i>The Albedo Method</i>	1400
6.1	Differential Number Albedo	1401
6.2	Integrals of Albedo Functions	1402
6.3	Application of the Albedo Method	1402
6.4	Albedo Approximations	1403
6.4.1	Photon Albedos	1403
6.4.2	Neutron Albedos	1405
7	<i>Skyshine</i>	1407
7.1	Approximations for the LBRF	1408
7.1.1	Photon LBRF Approximation	1409
7.1.2	Neutron LBRF Approximation	1409

7.2	Open Silo Example	1409
7.3	Shielded Skyshine Sources	1411
7.4	Computational Resources for Skyshine Analyses	1412
8	<i>Radiation Streaming Through Ducts</i>	1412
8.1	Characterization of Incident Radiation	1413
8.2	Line-of-Sight Component for Straight Ducts	1414
8.2.1	Line-of-Sight Component for the Cylindrical Duct	1414
8.2.2	Line-of-Sight Component for the Rectangular Duct	1415
8.3	Wall-Penetration Component for Straight Ducts	1415
8.4	Single-Scatter Wall-Reflection Component	1416
8.5	Photons in Two-Legged Rectangular Ducts	1418
8.6	Neutron Streaming in Straight Ducts	1420
8.7	Neutron Streaming in Ducts with Bends	1421
8.7.1	Two-Legged Ducts	1421
8.7.2	Neutron Streaming in Ducts with Multiple Bends	1423
8.8	Empirical and Experimental Results	1423
9	<i>Shield Design</i>	1424
9.1	Shielding Design and Optimization	1424
9.2	Shielding Materials	1425
9.2.1	Natural Materials	1425
9.2.2	Concrete	1427
9.2.3	Metallic Shielding Materials	1428
9.2.4	Special Materials for Neutron Shielding	1428
9.2.5	Materials for Diagnostic X-Ray Facilities	1429
9.3	A Review of Software Resources	1429
9.4	Shielding Standards	1430
10	<i>Health Physics</i>	1430
10.1	Deterministic Effects from Large Acute Doses	1431
10.1.1	Effects on Individual Cells	1431
10.1.2	Deterministic Effects in Organs and Tissues	1431
10.1.3	Potentially Lethal Exposure to Low-LET Radiation	1432
10.2	Hereditary Illness	1433
10.2.1	Classification of Genetic Effects	1434
10.2.2	Estimates of Hereditary Illness Risks	1435
10.3	Cancer Risks from Radiation Exposures	1435
10.3.1	Estimating Radiogenic Cancer Risks	1436
10.4	The Dose and Dose-Rate Effectiveness Factor	1437
10.4.1	Dose-Response Models for Cancer	1437
10.4.2	Average Cancer Risks for Exposed Populations	1438
10.5	Radiation Protection Standards	1439
10.5.1	Risk-Related Dose Limits	1440
10.5.2	The 1987 NCRP Exposure Limits	1441
	<i>References</i>	1442

Abstract: This chapter deals with shielding against nonionizing radiation, specifically gamma rays and neutrons with energies less than about 10 MeV, and addresses the assessment of health effects from exposure to such radiation. The chapter begins with a discussion of how to characterize mathematically the energy and directional dependence of the radiation intensity and, similarly, the nature and description of radiation sources. What follows is a discussion of how neutrons and gamma rays interact with matter and how radiation doses of various types are deduced from radiation intensity and target characteristics. This discussion leads to a detailed description of radiation attenuation calculations and dose evaluations, first making use of the point-kernel methodology and then treating the special cases of “skyshine” and “albedo” dose calculations. The chapter concludes with a discussion of shielding materials, radiological assessments, and risk calculations.

1 Radiation Fields and Sources

The transmission of directly and indirectly ionizing radiation through matter and its interaction with matter is fundamental to radiation shielding design and analysis. Design and analysis are but two sides of the same coin. In *design*, the source intensity and permissible radiation dose or dose rate at some location are specified, and the task is to determine the type and configuration of shielding that is needed. In *analysis*, the shielding material is specified, and the task is to determine the dose, given the source intensity, or the latter, given the former.

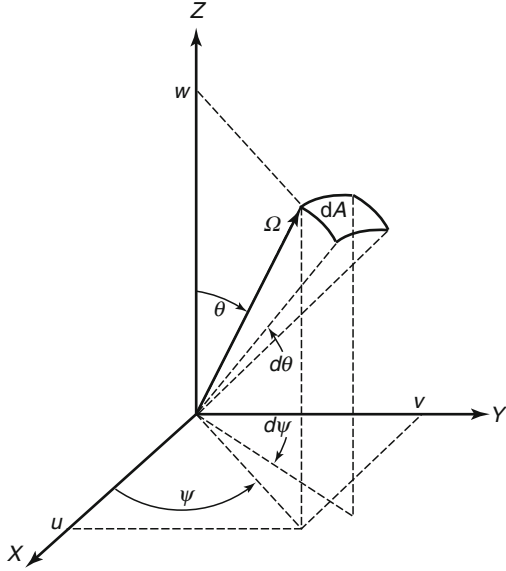
The radiation is conceptualized as particles – photons, electrons, neutrons, and so on. The term *radiation field* refers collectively to the particles and their trajectories in some region of space or through some boundary, either per unit time or accumulated over some period of time.

Characterization of the radiation field, for any one type of radiation particle, requires a determination of the spatial variation of the joint distribution of the particle’s energy and direction. In certain cases, such as those encountered in neutron scattering experiments, properties such as spin may be required for full characterization. Such infrequent and specialized cases are not considered in this chapter.

The sections to follow describe how to characterize the radiation field in a region of space in terms of the particle fluence and how to characterize the radiation field at a boundary in terms of the particle flow. The fluence and flow are called *radiometric* quantities, as distinguished from *dosimetric* quantities. The fluence and flow concepts apply both to measurement and calculation. Measured quantities are inherently stochastic, in that they involve enumeration of individual particle trajectories. Measurement, too, requires finite volumes or boundary areas. The same is true for fluence or flow calculated by Monte Carlo methods, because such calculations are, in large part, computer simulations of experimental determinations. In the methods of analysis discussed in this chapter, the fluence or flow is treated as a deterministic point function and should be interpreted as the expected value, in a statistical sense, of a stochastic variable. It is perfectly proper to refer to the fluence, flow, or related dosimetric quantity at a point in space. But it must be recognized that any measurement is only a single estimate of the expected value.

1.1 Radiation Field Variables

1.1.1 Direction and Solid Angle Conventions

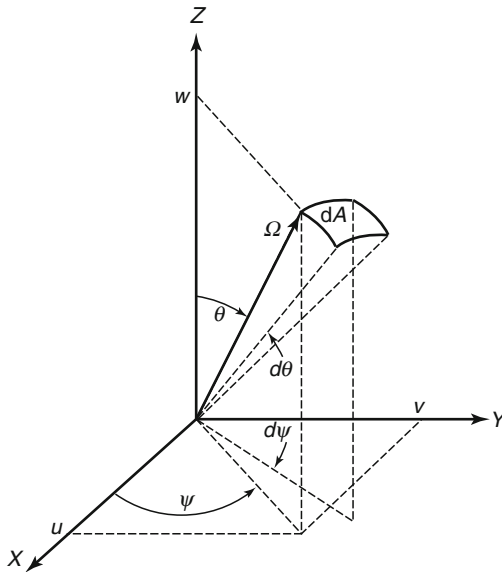
The directional properties of radiation fields are commonly described using spherical polar coordinates as illustrated in  Fig. 1. The direction vector is a unit vector, given in terms of the orthogonal Cartesian unit vectors \mathbf{i} , \mathbf{j} , and \mathbf{k} by

$$\mathbf{\Omega} = \mathbf{i}u + \mathbf{j}v + \mathbf{k}w = \mathbf{i} \sin \theta \cos \psi + \mathbf{j} \sin \theta \sin \psi + \mathbf{k} \cos \theta. \quad (1)$$

An increase in θ by $d\theta$ and ψ by $d\psi$ sweeps out the area $dA = \sin \theta d\theta d\psi$ on a sphere of unit radius. The solid angle encompassed by a range of directions is defined as the area swept out on the surface of a sphere divided by the square of the radius of the sphere. Thus, the differential solid angle associated with the differential area dA is $d\Omega = \sin \theta d\theta d\psi$. The solid angle is a dimensionless quantity. Nevertheless, to avoid confusion when referring to a directional distribution function, units of *steradians*, abbreviated sr, are attributed to the solid angle.

A substantial simplification in notation can be achieved by making use of $w \equiv \cos \theta$ as an independent variable instead of the angle θ , so that $\sin \theta d\theta = -dw$. The benefit is evident when one computes the solid angle subtended by “all possible directions,” namely,


$$\Omega = \int_0^\pi d\theta \sin \theta \int_0^{2\pi} d\psi = \int_{-1}^1 dw \int_0^{2\pi} d\psi = 4\pi. \quad (2)$$




■ Figure 1

Spherical polar coordinate system for specification of the unit direction vector Ω , polar angle θ , azimuthal angle ψ , and associated direction cosines (u, v, w)

1.1.2 Radiation Fluence

A fundamental way of characterizing the intensity of a radiation field is in terms of the number of particles that enter a specified volume. To make this characterization, the radiometric concept of *fluence* is introduced. The particle fluence, or simply fluence, at any point in a radiation field may be thought of in terms of the number of particles ΔN_p that, during some period of time, penetrate a hypothetical sphere of cross section ΔA centered on the point, as illustrated in  Fig. 2a. The fluence is defined as

$$\Phi \equiv \lim_{\Delta A \rightarrow 0} \left[\frac{\Delta N_p}{\Delta A} \right]. \quad (3)$$

An alternative, and often more useful definition of the fluence, is in terms of the sum $\sum_i s_i$ of path-length segments within the sphere, as illustrated in  Fig. 2b. The fluence can also be defined as

$$\Phi \equiv \lim_{\Delta V \rightarrow 0} \left[\frac{\sum_i s_i}{\Delta V} \right]. \quad (4)$$

Although the difference quotients of (3) and (4) are useful conceptually, beginning in 1971, the ICRU prescribed that the fluence should be given in terms of differential quotients, in recognition that ΔN_p is the expectation value of the number of particles entering the sphere. Thus, $\Phi \equiv dN_p/dA$, where dN_p is the number of particles which penetrate into a sphere of cross-sectional area dA .

The fluence rate, or *flux*, is expressed in terms of the number of particles entering a sphere, or the sum of path segments traversed within a sphere, per unit time, namely,

$$\phi \equiv \frac{d\Phi}{dt} = \frac{d^2 N_p}{dA dt}. \quad (5)$$

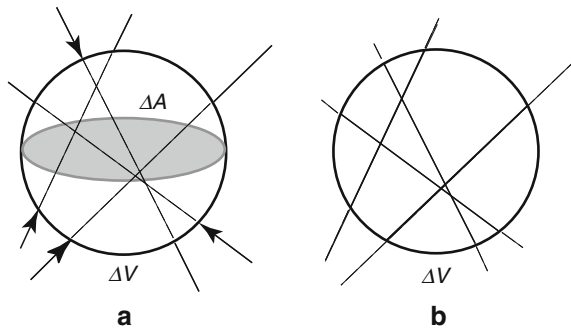
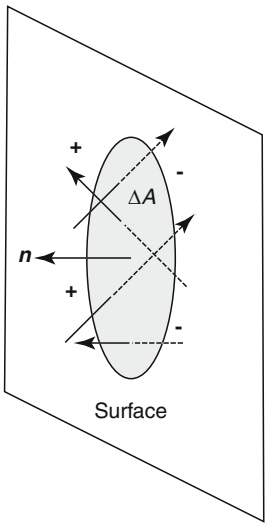


 Figure 2

Element of volume ΔV in the form of a sphere with cross-sectional area ΔA . In (a) the attention is on the number of particles passing through the surface *into* the sphere. In (b) the attention is on the paths traveled within the sphere by particles passing through the sphere

1.1.3 Radiation Current or Net Flow

Another radiometric measure of a radiation field is the net number of particles crossing a surface with a well-defined orientation, as illustrated in  Fig. 3. The *net particle flow* (or simply *net flow*) at a point on a surface is the net number of particles in some specified time interval that flow across a unit differential area on the surface, in the direction specified as positive. As shown in the figure, one side of the surface is characterized as the positive side and is identified by a unit vector \mathbf{n} normal to the area ΔA . If the number of particles crossing ΔA from the negative to the positive side is ΔM_p^+ and the number from the positive to the negative side is ΔM_p^- , then the *net* number crossing toward the positive side is $\Delta M_p \equiv \Delta M_p^+ - \Delta M_p^-$. The net flow at the given point is designated as J_n , with the subscript denoting the unit normal \mathbf{n} from the surface, and is defined as

$$J_n \equiv \lim_{\Delta A \rightarrow 0} \frac{\Delta M_p}{\Delta A} = \frac{dM_p}{dA}. \quad (6)$$

The total flow of particles in the positive and negative directions, J_n^+ and J_n^- , are defined in terms of ΔM_p^+ and ΔM_p^- in a similar manner. The relation between the net flow and the positive and negative flows is $J_n \equiv J_n^+ - J_n^-$.

The net flow *rate* is expressed in terms of the net number of particles crossing an area perpendicular to unit vector \mathbf{n} , per unit area and per unit time, namely, $j_n \equiv j_n^+ - j_n^-$.

The concepts of fluence and particle flow appear to be very similar, both being defined in terms of a number of particles per unit area. However, for the concept of the fluence, the area presented to incoming particles is independent of the direction of the particles, whereas for the particle flow concept, the orientation of the area is well defined.

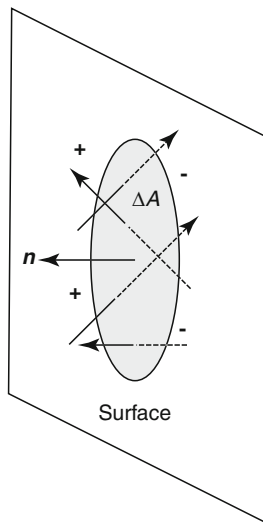


 **Figure 3**
Element of area ΔA in a surface. Particles cross the area from either side

1.1.4 Directional Properties of the Radiation Field


The computed fluence is a point function of position \mathbf{r} . Measurement of the fluence requires a radiation detector of finite volume; therefore, there is not only uncertainty due to experimental error but also ambiguity in identification of the “point” at which to attribute the measurement. The nature of the particles is implicit, and the argument \mathbf{r} in $\Phi(\mathbf{r})$ is sometimes implicit. With no other arguments, Φ or $\Phi(\mathbf{r})$ represents the total fluence irrespective of particle energy or particle direction, that is, integrated over all particle energies and directions.

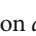
In many circumstances, it is necessary to broaden the concept of the fluence to include information about the energies and directions of particles. To do so requires the use of *distribution functions*. Particle energies and directions require, in general, fluences expressed as distribution functions. For example, $\Phi(\mathbf{r}, E) dE$ is, at point \mathbf{r} , the *fluence energy spectrum* – the fluence of particles with energies between E and $E + dE$.

The angular dependence of the fluence is a bit more complicated to write. The angular variable itself is the vector direction Ω . The direction is a function of the polar and azimuthal angles, θ and ψ . Similarly, the differential element of solid angle is a function of the same two variables, namely $d\Omega = \sin \theta d\theta d\psi = d\omega d\psi$. Thus, $\Phi(\mathbf{r}, \Omega) d\Omega$ or $\Phi(\mathbf{r}, \omega, \psi) d\omega d\psi$ is, at point \mathbf{r} , the angular fluence – the fluence of particles with directions in $d\Omega$ about Ω . The joint energy and angular distribution of the fluence is defined in such a way that $\Phi(\mathbf{r}, E, \Omega) dE d\Omega$ is the fluence of particles with energies in dE about E and with directions in $d\Omega$ about Ω .

In the system of notation adopted here, it is necessary that the energy and angular variables appear specifically as arguments of Φ to identify the fluence as a distribution function in these variables. The ICRU notation refers to the energy distribution as the *spectral distribution* and to the angular distribution as the *radiance*.

1.1.5 Angular Properties of the Flow and Flow Rate

Just as it is very often necessary to account for the variation of the fluence with particle energy and direction, the same is true for the flow and flow rate. Treatment of the energy dependence is no different from the treatment used for the fluence, so here only the angular dependence of the flow is examined. With an element of area and its orientation as illustrated in  Fig. 3, it is perfectly proper to define the angular flow in such a way that $J_n(\mathbf{r}, \Omega) d\Omega$ is the flow of particles through a unit area with directions in $d\Omega$ about Ω . The corresponding angular flow rate is written as $j_n(\mathbf{r}, \Omega)$.

 Figure 4 illustrates particles within a differential element of direction $d\Omega$ about direction Ω crossing a surface perpendicular to unit vector \mathbf{n} . Also shown in the figure is a sphere whose surface just intercepts all the particles. It is apparent that if ΔA is the cross-sectional area of the sphere, then the corresponding area in the surface is $\Delta A \sec \theta$, where $\cos \theta = \mathbf{n} \cdot \Omega$. Thus, because the same number of particles pass through the sphere and through the area in $J_n(\mathbf{r}, \Omega) \Delta A = \cos \theta \Delta A \Phi(\mathbf{r}, \Omega)$, or

$$J_n(\mathbf{r}, \Omega) = \mathbf{n} \cdot \Omega \Phi(\mathbf{r}, \Omega). \quad (7)$$

The net flow is given by

$$\begin{aligned} J_n(\mathbf{r}) &\equiv \int_{4\pi} d\Omega J_n(\mathbf{r}, \Omega) \\ &= \int_{4\pi} d\Omega \mathbf{n} \cdot \Omega \Phi(\mathbf{r}, \Omega). \end{aligned} \quad (8)$$

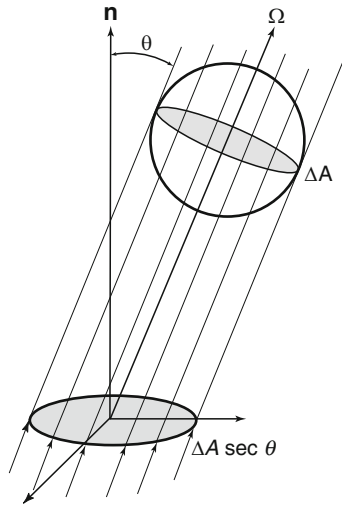


Figure 4
 $J_n(\mathbf{r}, \Omega)$ versus $\Phi(\mathbf{r}, \Omega)$

The fluence is a positive quantity; however, $J_n(\mathbf{r}, \Omega)$ is positive or negative as $\mathbf{n} \cdot \Omega$ is positive or negative. That part of the integral for which $\mathbf{n} \cdot \Omega$ is positive is the flow $J_n^+(\mathbf{r})$, and that part for which $\mathbf{n} \cdot \Omega$ is negative is $-J_n^-(\mathbf{r})$. The algebraic sum of the two parts gives the net flow $J_n(\mathbf{r})$.

1.2 Characterization of Radiation Sources

1.2.1 General Considerations

The most fundamental type of source is a point source. A real source can be approximated as a point source provided that (1) the volume is sufficiently small, that is, with dimensions much smaller than the dimensions of the attenuating medium between the source and detector, and (2) there is negligible interaction of radiation with the matter in the source volume. The second requirement may be relaxed if source characteristics are modified to account for source self-absorption and other source-particle interactions.

In general, a point source may be characterized as depending on energy, direction, and time. In almost all shielding practices, time is not treated as an independent variable because the time delay between a change in the source and the resulting change in the radiation field is usually negligible. Therefore, the most general characterization of a point source used here is in terms of energy and direction, so that $S_p(E, \Omega) dE d\Omega$ is the number of particles emitted with energies in dE about E and in $d\Omega$ about Ω . Common practical units for $S_p(E, \Omega)$ are $\text{MeV}^{-1} \text{sr}^{-1}$ or $\text{MeV}^{-1} \text{s}^{-1}$.

Most radiation sources treated in the shielding practice are isotropic, so that source characterization requires only knowledge of $S_p(E) dE$, which is the number of particles emitted with energies in dE about E (per unit time), and has common practical units of MeV^{-1} (or $\text{MeV}^{-1} \text{s}^{-1}$). Radioisotope sources are certainly isotropic, as are fission sources and capture gamma-ray sources.

A careful distinction must be made between the activity of a radioisotope and its source strength. *Activity* is precisely defined as the expected number of atoms undergoing radioactive transformation per unit time. It is *not* defined as the number of particles emitted per unit time. Decay of two very common laboratory radioisotopes illustrate this point. Each transformation of ^{60}Co , for example, results in the emission of two gamma rays, one at 1.173 MeV and the other at 1.333 MeV. Each transformation of ^{137}Cs , accompanied by a transformation of its decay product ^{137m}Ba , results in emission of a 0.662-MeV gamma ray with probability 0.85.

The SI unit of activity is the becquerel (Bq), equivalent to 1 transformation per second. In medical and health physics, radiation source strengths are commonly calculated on the basis of *accumulated activity*, Bq s. Such time-integrated activities account for the cumulative number of transformations in some biological entity during the transient presence of radionuclides in the entity. Of interest in such circumstances is not the time-dependent dose rate to that entity or some other nearby region, but rather the total dose accumulated during the transient. Similar practices are followed in dose evaluation for reactor transients, solar flares, nuclear weapons, and so on.

Radiation sources may be distributed along a line, over an area, or within a volume. Source characterization requires, in general, spatial and energy dependence, with $S_l(\mathbf{r}, E) dE$, $S_a(\mathbf{r}, E) dE$, and $S_v(\mathbf{r}, E) dE$ representing, respectively, the number of particles emitted in dE about E per unit length, per unit area, and per unit volume. Occasionally, it is necessary to include angular dependence. This is especially true for effective area sources associated with computed angular flows across certain planes. Clearly, for a fixed surface, $S_a(\mathbf{r}, E, \Omega)$ and $J_n(\mathbf{r}, E, \Omega)$ are equivalent specifications.

Energy dependence may be discrete, such as for radionuclide sources, or continuous, as for bremsstrahlung or fission neutrons and photons. When discrete energies are numerous, an energy multigroup approach is often used. The same multigroup approach may be used to approximately characterize a source whose emissions are continuous in energy.

1.2.2 Neutron Sources

Fission Sources

Many heavy nuclides fission after the absorption of a neutron, or even spontaneously, producing several energetic fission neutrons. Fission neutrons may produce secondary radiation sources, such as inelastic-scattering photons and capture gamma photons, and may transmute stable isotopes into radioactive ones.

Almost all of the fast neutrons produced from a fission event are emitted within 10^{-7} s of the fission event. Less than 1% of the total fission neutrons are emitted as *delayed neutrons*, which are produced by the neutron decay of fission products at times up to many minutes after the fission event. Except for very specialized situations, these delayed neutrons, which are emitted with significantly less energy than the prompt neutrons, are of little importance in shield design because of their relatively small yield and low energies.

As the energy of the neutron which induces the fission in a heavy nucleus increases, the average number of fission neutrons also increases. Yields in thermal-neutron induced fission of ^{235}U , ^{239}Pu , and ^{233}U are respectively 2.43, 2.87, and 2.48. See Keepin (1965) for information on epithermal- and fast-neutron induced fission.

Many transuranic isotopes have appreciable, spontaneous fission probabilities; and consequently, they can be used as very compact sources of fission neutrons. For example, 1 g of ^{252}Cf releases 2.3×10^{12} neutrons per second, and very intense neutron sources can be made from this isotope, limited in size only by the need to remove the fission heat through the necessary encapsulation. Properties of the spontaneously fissioning isotopes of greatest importance in spent nuclear fuel are listed in [Table 1](#). Almost all of these isotopes decay much more rapidly by α emission than by spontaneous fission.

The energy dependence of the fission neutron spectrum has been investigated extensively, especially that for ^{235}U . All fissionable nuclides produce a distribution of prompt fission-neutron energies which goes to zero at low and high energies and reaches a maximum at about 0.7 MeV. The fraction of prompt fission neutrons emitted per unit energy about E , $\chi(E)$, can be described quite accurately by a modified two-parameter Maxwellian distribution (a Maxwellian corrected for the average energy of the fission fragments in the laboratory coordinate system), namely,

$$\chi(E) = \frac{e^{-(E+E_\omega)/T_\omega}}{\sqrt{\pi E_\omega T_\omega}} \sinh \sqrt{\frac{4E_\omega E}{T_\omega^2}}. \quad (9)$$

In many shielding applications, the spectrum for thermal-neutron-induced fission of ^{235}U has often been used, at least as a first approximation for other fissioning isotopes, although ^{233}U , ^{239}Pu , and ^{252}Cf have somewhat greater high-energy components; and consequently, their fission neutrons are slightly more penetrating than those of ^{235}U . Please refer to [Table 2](#) for parameter values.

Photoneutrons

A gamma photon with energy sufficiently larger to overcome the neutron-binding energy (about 7 MeV in most nuclides) may cause a (γ, n) reaction. Very intense and energetic photoneutron production can be realized in an electron accelerator where the bombardment of an appropriate target material with the energetic electrons produces intense bremsstrahlung with a distribution of energies up to that of the incident electrons.

Table 1

Selected nuclides which spontaneously fission. All also decay by alpha emission, which is usually the only other decay mode

Nuclide	Half-life	Fission prob. per decay (%)	Neutrons per fission	α per fission	Neutrons per (g s)
^{238}Pu	87.7 y	1.9×10^{-7}	2.28	5.4×10^8	2.7×10^3
^{240}Pu	6569 y	5.7×10^{-6}	2.21	2.0×10^7	920
^{242}Pu	3.76×10^5 y	5.5×10^{-4}	2.24	1.8×10^5	1.8×10^3
^{242}Cm	163 d	6.2×10^{-6}	2.70	1.5×10^7	2.3×10^7
^{244}Cm	18.11 y	1.37×10^{-4}	2.77	7.5×10^5	1.1×10^7
^{246}Cm	4730 y	0.02615	2.86	3.8×10^3	8.5×10^6
^{252}Cf	2.645 y	3.092	3.73	31	2.3×10^{12}

Sources: Data compiled from Dillman (1980), Kocher (1981), and Reilly et al. (1991), and from the NuDat data resource of the National Nuclear Data Center at Brookhaven National Laboratory

■ **Table 2**

Parameters for the Watt approximation for the prompt fission-neutron distribution for various fissionable nuclides. Values for ^{252}Cf are from Fröhner (1990). The other values were obtained by a logarithmic fit of the Watt formula to the calculated spectra by Walsh (1989)

Nuclide	Type of fission	Equation (9)	
		E_w	T_w
^{233}U	Thermal	0.3870	1.108
^{235}U	Thermal	0.4340	1.035
^{239}Pu	Thermal	0.4130	1.159
^{232}Th	Fast (2 MeV)	0.4305	0.971
^{238}U	Fast (2 MeV)	0.4159	1.027
^{252}Cf	Spontaneous	0.359	1.175

■ **Table 3**

Important nuclides for photoneutron production

Nuclide	Threshold E_t (MeV) ($-Q$ value)	Reaction
^2H	2.225	$^2\text{H}(\gamma, n)^1\text{H}$
^6Li	3.698	$^6\text{Li}(\gamma, n + p)^4\text{He}$
^6Li	5.664	$^6\text{Li}(\gamma, n)^5\text{Li}$
^7Li	7.251	$^7\text{Li}(\gamma, n)^6\text{Li}$
^9Be	1.665	$^9\text{Be}(\gamma, n)^8\text{Be}$
^{13}C	4.946	$^{13}\text{C}(\gamma, n)^{12}\text{C}$

In reactor shielding analyses, the gamma photons encountered have energies too low, and most materials have a photoneutron threshold too high for photoneutrons to be of concern. Only for a few light elements, listed in ▶ [Table 3](#), are the thresholds for photoneutron production sufficiently low that these secondary neutrons may have to be considered. In heavy water- or beryllium-moderated reactors, the photoneutron source may be very appreciable, and the neutron-field deep within a hydrogenous shield is often determined by photoneutron production in deuterium, which constitutes about 0.015 at% of the hydrogen. Capture gamma photons arising from neutron absorption have particularly high energies and, thus, may cause a significant production of energetic photoneutrons.

The photoneutron mechanism can be used to create laboratory neutron sources by mixing intimately a beryllium or deuterium compound with a radioisotope that decays with the emission of high-energy photons. Alternatively, the encapsulated radioisotope may be surrounded

by a beryllium- or deuterium-bearing shell. One common laboratory photoneutron source is an antimony–beryllium mixture, which has the advantage of being rejuvenated by exposing the source to the neutrons in a reactor to transmute the stable ^{123}Sb into the required ^{124}Sb isotope (half-life of 60.2 days). Other common sources are mixtures of ^{226}Ra and beryllium or heavy water.

One very attractive feature of such (γ, n) sources is the nearly monoenergetic nature of the neutrons if the photons are monoenergetic. However, in large sources, the neutrons may undergo significant scattering in the source material, and thereby degrade the nearly monoenergetic nature of their spectrum. These photoneutron sources generally require careful usage because of their inherently large, photon emission rates. Because only a small fraction of the high-energy photons (typically, 10^{-6}) actually interact with the source material to produce a neutron, these sources generate gamma rays that are of far greater biological concern than the neutrons.

Neutrons from (α, n) Reactions

Many compact neutron sources use energetic alpha particles from various radioisotopes (*emitters*) to induce (α, n) reactions in appropriate materials (*converters*). Although a large number of nuclides emit neutrons if bombarded with alpha particles of sufficient energy, the energies of the alpha particles from radioisotopes are capable of penetrating the Coulombic potential barriers of only the lighter nuclei.

Of particular interest are those light isotopes for which the (α, n) reaction is exothermic ($Q > 0$) or, at least, has a low threshold energy (see [Table 4](#)). For endothermic reactions, the threshold alpha energy is $-Q(1 + 4/A)$. Thus, for an (α, n) reaction to occur, the alpha particle must (1) have enough energy to penetrate the Coulomb barrier, and (2) exceed the threshold energy. Alpha particles emitted by uranium and plutonium range between 4 and 6 MeV and can cause (α, n) neutron production when in the presence of oxygen or fluorine. Neutrons from (α, n) reactions often exceed the spontaneous fission neutrons in UF_6 or in aqueous mixtures of uranium and plutonium such as found in nuclear waste (Reilly et al. 1991).

A neutron source can be fabricated by mixing intimately one of the converter isotopes listed in [Table 4](#) with an alpha-particle emitter. Most of the practical alpha emitters are actinide elements, which form intermetallic compounds with beryllium. Such a compound (e.g., PuBe_{13})

■ **Table 4**

Important (α, n) reactions

Target	Natural abundance (%)	Reaction	energy (MeV) (Q value)	Threshold energy (MeV)	Coulomb barrier (MeV)
^9Be	100	$^9\text{Be}(\alpha, n)^{12}\text{C}$	5.702	Exothermic	2.6
^9Be	100	$^9\text{Be}(\alpha, n)3\alpha$	-1.573	2.272	2.6
^{10}B	19.8	$^{10}\text{B}(\alpha, n)^{13}\text{N}$	1.060	Exothermic	3.2
^{11}B	80.2	$^{11}\text{B}(\alpha, n)^{14}\text{N}$	0.157	Exothermic	3.2
^{18}O	0.2	$^{18}\text{O}(\alpha, n)^{21}\text{Ne}$	-0.697	0.852	4.6
^{19}F	100	$^{19}\text{F}(\alpha, n)^{22}\text{Na}$	-1.950	2.361	5.1

ensures both that the emitted alpha particles immediately encounter converter nuclei, thereby producing a maximum neutron yield, and that the radioactive actinides are bound into the source material, thereby reducing the risk of leakage of the alpha-emitting component. Some characteristics of selected (α, n) sources are listed in ► [Table 5](#).

The neutron yield from an (α, n) source varies strongly with the converter material, the energy of the alpha particle, and the relative concentrations of the emitter and converter elements. The degree of mixing between the converter and emitter, and the size, geometry, and source encapsulation may also affect the neutron yield.

The energy distributions of neutrons emitted from all such sources are continuous below some maximum neutron energy with definite structure at well-defined energies determined by the energy levels of the converter and the excited product nuclei. The use of the same converter material with different alpha emitters produces similar neutron spectra with different portions of the same basic spectrum accentuated or reduced as a result of the different alpha-particle energies.

Generally, neutrons emitted from the ${}^9\text{Be}(\alpha, n)$ reaction have higher energies than those produced by other (α, n) sources because Be has a larger Q value than that of other converters. The structure in the Be-produced neutron spectrum above 1 MeV can be interpreted in terms of structure in the ${}^9\text{Be}(\alpha, n){}^{12}\text{C}$ cross section, which in turn depends on the excitation state in which the ${}^{12}\text{C}$ nucleus is left. A large peak below 1 MeV in the Be neutron spectrum arises not from the direct (α, n) reaction, but from the “breakup” reaction ${}^9\text{Be}(\alpha, \alpha'){}^9\text{Be}^* \rightarrow {}^8\text{B} + n$. As the alpha-particle energy increases, both the fraction of neutrons emitted from the breakup reaction ($E_n < 1$ MeV) and the probability that the product nucleus is left in an excited state ($E_n < 6$ MeV) increase, thereby decreasing slightly the average neutron energy (see ► [Table 5](#)).

In all (α, n) sources, there is a maximum neutron energy corresponding to the reaction in which the product nucleus is left in the ground state and the neutron appears in the same direction as that of the incident alpha particle ($\theta = 0$). Thus, unlike fission neutron sources, there are no very high energy neutrons generated in an (α, n) source.

■ **Table 5**
Characteristics of some (α, n) sources

Source	Half-life	Principal alpha energies (MeV)	Average neutron energy (MeV)	Optimum neutron yield per 10^6 primary alphas ^a
${}^{239}\text{Pu}$ / Be	24100 y	5.155, 5.143, 5.105	4.6	60
${}^{210}\text{Po}$ / Be	138.4 d	5.305	4.5	70
${}^{238}\text{Pu}$ / Be	87.8 y	5.499, 5.457, 5.358	4.5	80
${}^{241}\text{Am}$ / Be	432 y	5.486, 5.443, 5.388	4.4	75
${}^{226}\text{Ra}$ / Be + daughters	1600 y	7.687, 6.003, 5.490 5.304, 4.785, 4.602	3.9	500 ^b

Sources: Jaeger (1968), GPO (1970), and Knoll (1989)

^aYield for alpha particles incident on a target thicker than the alpha-particle ranges

^bYield is dependent on the proportion of daughters present. Value for ${}^{226}\text{Ra}$ corresponds to a 22-year-old source (50% contribution for ${}^{210}\text{Po}$)


With appropriate (α, n) cross-section data for a converter, ideal neutron energy spectra can be calculated for the monoenergetic alpha particles emitter by different alpha emitters (Geiger and Van der Zwan 1975). However, these ideal spectra are modified somewhat in actual (α, n) sources. The monoenergetic alpha particles lose variable amounts of energy through ionization interactions in the source material before inducing an (α, n) reaction. This effectively continuous nature of the alpha-particle energy spectrum tends to smooth out many of the fine features of the ideal neutron spectrum. Further, if the source is physically large as a result of requiring a large activity (e.g., a $^{239}\text{Pu}/\text{Be}$ source emitting 10^7 neutrons per second requires about 73 g of plutonium), neutron interactions within the source itself may alter the emitted neutron spectrum. Neutron scattering, $(n, 2n)$ reactions with beryllium, and even neutron-induced fission of the actinide converter change the neutron energy spectrum slightly. Finally, impurity nuclides, which also emit alpha particles, as well as the buildup of alpha-emitting daughters, affect the neutron energy spectrum. In general, the neutron energy spectrum as well as the yield depend in a very complicated manner on the composition, size, geometry, and encapsulation of the source. Fortunately, in most shielding applications only approximate energy information is needed and idealized spectra are often adequate.

Activation Neutrons

A few highly unstable nuclides decay by the emission of a neutron. The delayed neutrons associated with fission arise from such decay of the fission products. However, there are nuclides other than those in the fission-product decay chain which also decay by neutron emission. Only one of these nuclides, ^{17}N , is of importance in shielding situations. This isotope is produced in water-moderated reactors by an (n, p) reaction with ^{17}O (threshold energy, 8.0 MeV), with a small cross section of about $5.2 \mu\text{b}$ averaged over the fission spectrum. The decay of ^{17}N by beta emission (half-life 4.4 s) produces ^{17}O in a highly excited state, which in turn decays rapidly by neutron emission. Most of the decay neutrons are emitted within ± 0.2 MeV of the most probable energy of about 1 MeV, although a few neutrons with energies up to 2 MeV may be produced.

Fusion Neutrons

Many nuclear reactions induced by energetic charged particles can produce neutrons. Most of these reactions require incident particles of very high energies for the reaction to take place and, consequently, are of little concern to the shielding analyst. Only near accelerator targets, for example, would such reaction neutrons be of concern.

From a shielding viewpoint, one major exception to the insignificance of charged particle-induced reactions are those fusion reactions in which light elements fuse exothermally to yield a heavier nucleus and which are accompanied quite often by the release of energetic neutrons. The resulting fusion neutrons are usually the major source of radiation to be shielded against. Prompt gamma photons are not emitted in the fusion process, and the bremsstrahlung produced by charged-particle deflections are easily shielded by any shielding adequate for protection from the neutrons. On the other hand, activation and capture gamma photons may arise as a result of neutrons being absorbed in the surrounding material. Cross sections for the two neutron-producing fusion reactions of most interest in the development of thermonuclear fusion power are illustrated in  Fig. 5. In the D-D reaction and D-T reactions, 2.45 and 14.1 MeV neutrons, respectively, are released.

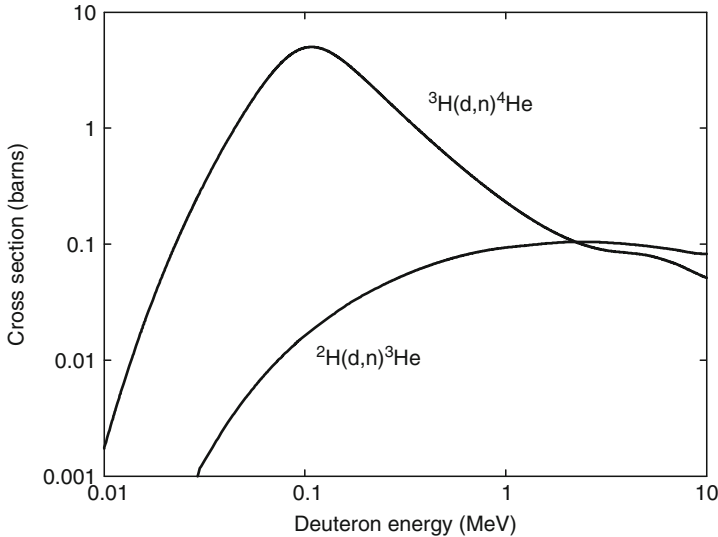


Figure 5

Cross sections for the two most easily induced thermonuclear reactions as a function of the incident deuteron energy. Tritium data are from ENDF/B-VI.8 and deuterium data from ENDF/B-VII.0

1.2.3 Gamma-Ray Sources

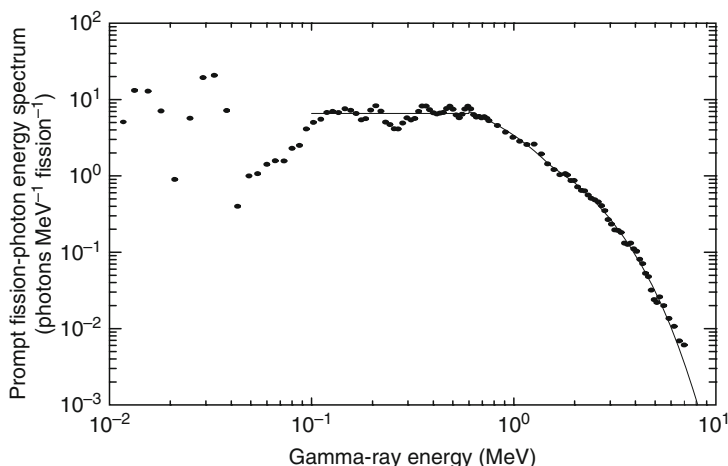
Radioactive Sources

There are many data sources for characterizing such sources. Printed documents include compilations by Kocher (1981), Weber et al. (1989), Eckerman et al. (1994), and Firestone et al. (1996). There are also many online data sources. One is the NuDAT (nuclear structure and decay data) and Chart of the Nuclides, www.nndc.bnl.gov, supported by the National Nuclear Data Center at Brookhaven National Laboratory. Another is the WWW table of radioisotopes (TORI) <http://nucleardata.nuclear.lu.se/nucleardata/toi> supported by the Lund/LBNL Nuclear Data Search. For detailed information on secondary X-rays and Auger electrons, the computer program of Dillman (1980) is invaluable.

Prompt Fission Gamma Photons

The fission process produces copious gamma photons. The *prompt fission-gamma photons* are released in the first 50 ns after the fission event. Those emitted later are the *fission product gamma photons*. Both are of extreme importance in the shielding and gamma-heating calculations for a reactor.

Investigations of prompt fission-gamma photons have centered on the thermal-neutron-induced fission of ^{235}U . For this nuclide, it has been found that the number of prompt fission photons is 8.13 ± 0.35 photons per fission over the energy range of 0.1 to 10.5 MeV, and the energy carried by this number of photons is 7.25 ± 0.26 MeV per fission (Peele and Maienschein 1970). In [Fig. 6](#), the measured prompt fission-photon spectrum per thermal fission is shown for thermal fission of ^{235}U . The large peaks observed at 15 and 30 keV are X-rays emitted by the light- and heavy-fission fragments, respectively. Although some structure is evident between



■ Figure 6

Energy spectrum of prompt fission photons emitted within the first 69 ns after the fission of ^{235}U by thermal neutrons. Data are from Peele and Maienschein (1970) and the line is the fission-spectrum approximation of (10)

0.1 and 0.6 MeV, the prompt fission-gamma spectrum is approximately constant at $6.6 \text{ photons MeV}^{-1} \text{ fission}^{-1}$. At higher energies, the spectrum falls off sharply with increasing energy. For shielding purposes, the measured energy distribution shown in Fig. 6 can be represented by the following empirical fit over the range of 0.1 to 10.5 MeV (Peele and Maienschein 1970):

$$N_{py}(E) = \begin{cases} 6.6 & 0.1 < E < 0.6 \text{ MeV} \\ 20.2e^{-1.78E} & 0.6 < E < 1.5 \text{ MeV} \\ 7.2e^{-1.09E} & 1.5 < E < 10.5 \text{ MeV,} \end{cases} \quad (10)$$

where E is in MeV and $N_{py}(E)$ is in units of $\text{photons MeV}^{-1} \text{ fission}^{-1}$. The low-energy prompt fission photons (i.e., those below 0.6 MeV) are not of concern for shielding considerations, although they may be important for gamma-heating problems. For this purpose, 3.74 photons with an average energy of 0.324 MeV may be considered as emitted below 0.6 MeV per fission. Relatively little work has been done to determine the characteristics of prompt fission photons from the fission of nuclides other than ^{235}U , but it is reasonable for shielding purposes to use ^{235}U spectra to approximate those for ^{233}U , ^{239}Pu , and ^{252}Cf .

Gamma Photons from Fission Products

One of the important concerns for the shielding analyst is the consideration of the very long lasting gamma activity produced by the decay of fission products. The total gamma-ray energy released by the fission product chains at times greater than 50 ns after the fission is comparable with that released as prompt fission gamma photons. About three-fourths of the delayed gamma-ray energy is released in the first thousand seconds after fission. In the calculations

involving spent fuel, the gamma activity at several months or even years after the removal of fuel from the reactor is of interest and only the long-lived fission products need be considered.

The gamma energy released from fission products is not very sensitive to the energy of the neutrons causing the fissions. However, the gamma-ray energy released and the photon energy spectrum depend significantly on the fissioning isotope, particularly in the first 10 s after fission. Generally, fissioning isotopes having a greater proportion of neutrons to protons produce fission-product chains of longer average length, with isotopes richer in neutrons and hence, with greater available decay energy. Also, the photon energy spectrum generally becomes "softer" (i.e., less energetic) as the time after the fission increases. Fission products from ^{235}U and ^{239}Pu release, on average, photon energy of 6.84 and 6.15 MeV/fission, respectively (Keepin 1965).

For very approximate calculations, the energy spectrum of delayed gamma photons from the fission of ^{235}U , at times up to about 500 s, may be approximated by the proportionality

$$N_{dy}(E) \sim e^{-1.1E}, \quad (11)$$

where $N_{dy}(E)$ is the delayed gamma yield (photons MeV^{-1} fission $^{-1}$) and E is the photon energy in MeV. The time dependence for the total gamma photon energy emission rate $F_T(t)$ (MeV s^{-1} fission $^{-1}$) is often described by the simple decay formula

$$F_T(t) = 1.4t^{-1.2}, \quad 10 \text{ s} < t < 10^8 \text{ s}, \quad (12)$$

where t is in seconds. More detailed, yet conservative expressions are available in the industrial standards [ANSI/ANS 2005]. ^{235}U and ^{239}Pu have roughly the same total gamma-ray-energy decay characteristics for up to 200 days after fission, at which time ^{235}U products begin to decay more rapidly until at 1 year after fission, the ^{239}Pu gamma activity is about 60% greater than that of ^{235}U .

Gamma-photon source data for the use in reactor design and analysis are readily available from software such as the ORIGEN code, which accounts for mixed oxide fuels and differing operating conditions, namely, BWR, PWR, or CANDU concentrations and temperatures. Activation products are also taken into account, as are spontaneous fission. Both gamma-photon and neutron spectra are available at user-selected times and energy group structures. As of this writing, the ORIGEN code is available as code package C00732 SCALE5.1/ORIGEN from the Radiation Safety Information Computational Center, Oak Ridge National Laboratory, Oak Ridge, Tennessee.

Sample ORIGEN results are given in [Table 6](#) for two extreme cases: time dependent (a) gamma-ray decay power from fission products created by a single fission event, and (b) gamma-ray decay power from fission products created during a 30,000-h period of operation at a constant rate of one fission per second. These particular results are for fission products only and are for fission of ^{235}U . The results do not account for bremsstrahlung or for neutron absorption, during operation, by previously produced fission products.

With these or similar results, the gamma-energy emission rate can be calculated for a wide variety of operation histories and decay times. Let $F_j(t)$ be the rate of energy emission via gamma photons in energy group j from fission products created by a single fission event t seconds earlier. Then, the photon energy emission rates can be calculated readily in terms of $F_j(t)$ for a sample of fissionable material which has experienced a prescribed power or fission history $P(t)$. Data fits are provided by George et al. (1980) and Labauve et al. (1982) for both ^{235}U and

Table 6

Fission-product gamma-photon energy release rates (MeV/s) for thermal fission of ^{235}U , computed using the ORIGEN code (RSIC 1991), Hermann and Westfall (1995)

Mean Energy (MeV)	Cooling time t (s)								
	10	100	1000	10^4	10^5	10^6	10^7	10^8	10^9
Single instantaneous fission event ^a									
0.010	1.69–04 ^a	1.70–05	2.14–06	1.34–07	6.98–09	3.78–10	2.79–11	1.16–12	1.61–13
0.030	1.78–04	2.05–05	2.42–06	1.65–07	1.40–08	1.25–09	3.78–11	1.54–12	2.02–13
0.055	2.33–04	2.28–05	2.41–06	1.65–07	1.01–08	4.65–10	3.19–11	1.45–12	1.84–13
0.085	2.27–04	2.28–05	2.73–06	1.72–07	8.59–09	1.35–09	2.83–11	1.43–12	1.58–13
0.120	2.72–04	2.85–05	2.55–06	1.83–07	1.51–08	9.77–10	4.17–11	2.56–12	1.51–13
0.170	4.42–04	5.96–05	8.72–06	5.70–07	2.13–08	2.07–09	1.21–10	1.78–12	2.09–13
0.300	1.39–03	2.17–04	3.43–05	1.35–06	1.60–07	8.07–09	7.31–11	3.56–12	3.81–13
0.650	3.91–03	5.86–04	1.06–04	1.40–05	8.01–07	4.29–08	4.81–09	3.20–11	1.29–11
1.130	2.10–03	6.95–04	1.19–04	6.09–06	2.27–07	5.45–09	3.08–11	1.41–12	7.47–14
1.580	1.14–03	2.40–04	5.51–05	6.95–06	1.09–07	3.84–08	1.39–10	8.17–13	1.33–14
2.000	4.93–04	1.25–04	3.46–05	3.02–06	2.48–08	5.86–10	2.10–11	1.68–12	1.01–15
2.400	4.26–04	1.23–04	2.74–05	4.01–06	9.80–09	2.74–09	9.87–12	5.54–14	7.08–19
2.800	5.03–04	1.37–04	9.74–06	1.03–06	2.91–10	4.42–11	2.26–13	9.04–15	2.67–23
3.250	2.89–04	1.11–04	6.89–06	4.87–07	7.50–11	2.29–11	9.13–14	1.46–15	5.32–24
3.750	2.53–04	5.77–05	3.84–06	2.65–07	1.51–11	7.15–18	5.19–18	7.43–19	2.71–27
4.250	2.89–04	1.15–04	2.89–06	3.40–09	2.64–12	1.64–30	1.69–30	1.99–30	2.27–30
4.750	2.57–04	2.44–05	4.84–07	9.77–09	2.19–11	9.20–31	9.45–31	1.12–30	1.27–30
5.500	2.87–04	1.72–05	3.43–07	7.27–11	1.62–13	7.91–31	8.11–31	9.61–31	1.09–30
Total	1.28–02	2.62–03	4.23–04	3.84–05	1.41–06	1.05–07	5.38–09	4.93–11	1.44–11
Long-term operation for 30,000 h at 1 fission per second									
0.010	2.00–02	1.32–02	8.78–03	4.68–03	2.26–03	1.22–03	4.81–04	6.34–05	1.55–05
0.030	2.63–02	1.90–02	1.36–02	8.78–03	5.51–03	2.24–03	6.31–04	8.27–05	1.97–05
0.055	2.56–02	1.64–02	1.08–02	6.15–03	3.03–03	1.44–03	5.90–04	7.69–05	1.76–05
0.085	2.75–02	1.85–02	1.27–02	7.31–03	4.55–03	2.04–03	5.70–04	7.21–05	1.50–05
0.120	3.18–02	2.05–02	1.44–02	9.23–03	5.74–03	2.03–03	1.03–03	1.09–04	1.45–05
0.170	7.27–02	5.32–02	3.68–02	1.80–02	1.05–02	5.16–03	1.05–03	9.23–05	1.99–05
0.300	2.62–01	1.92–01	1.31–01	6.50–02	3.59–02	1.02–02	1.45–03	1.80–04	3.62–05
0.650	1.16+00	9.80–01	7.82–01	4.81–01	2.80–01	1.42–01	4.61–02	3.24–03	1.33–03
1.130	6.86–01	5.51–01	3.43–01	1.24–01	2.95–02	6.41–03	6.98–04	9.42–05	8.78–06

Table 6 (continued)

Mean Energy (MeV)	Cooling time t (s)								
	10	100	1000	10^4	10^5	10^6	10^7	10^8	10^9
1.580	4.93-01	4.39-01	3.59-01	1.87-01	1.03-01	5.90-02	5.61-04	4.23-05	1.44-06
2.000	1.89-01	1.64-01	1.14-01	3.65-02	4.17-03	1.32-03	6.89-04	5.61-05	9.61-08
2.400	1.94-01	1.70-01	1.33-01	4.39-02	7.31-03	4.23-03	3.91-05	3.00-06	6.73-11
2.800	9.13-02	6.54-02	3.56-02	7.24-03	1.26-04	7.34-05	4.26-06	5.29-07	1.73-15
3.250	5.99-02	4.36-02	1.62-02	3.62-03	5.99-05	3.68-05	7.85-07	9.45-08	3.46-16
3.750	3.46-02	2.33-02	8.84-03	1.88-03	1.87-07	4.10-10	3.36-10	4.81-11	1.76-19
4.250	4.23-02	2.68-02	8.72-04	2.13-05	3.52-08	1.87-22	1.90-22	2.10-22	2.28-22
4.750	1.38-02	5.16-03	3.30-04	1.30-04	2.91-07	1.05-22	1.07-22	1.18-22	1.28-22
5.500	1.20-02	3.72-03	7.21-05	9.64-07	2.16-09	9.04-23	9.16-23	1.01-22	1.10-22
Total	3.43+00	2.81+00	2.02+00	1.00+00	4.90-01	2.37-01	5.38-02	4.10-03	1.47-03

^aRead as 1.69×10^{-4}

²³⁹Pu and for all fission products or gaseous products only. Shultis and Faw (2000) reproduce the data and address procedures in detail. Calculations mirroring the data of Table 6 are illustrated in Figs. 7 and 8.

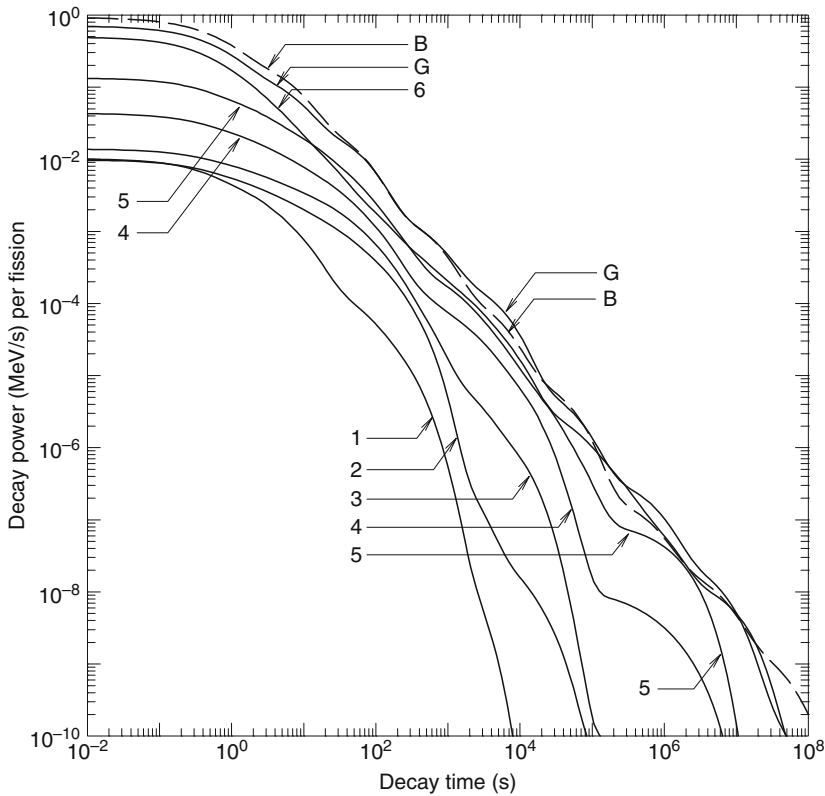
Capture Gamma Photons

The compound nucleus formed by neutron absorption is initially created in a highly excited state with excitation energy equal to the kinetic energy of the incident neutron plus the neutron-binding energy, which averages about 7 MeV. The decay of this nucleus, within 10^{-12} s and usually by way of intermediate states, typically produces several energetic photons. Such capture photons may be created intentionally by placing a material with a high thermal-neutron (n, γ) cross section in a thermal-neutron beam. The energy spectrum of the resulting capture gamma photons can then be used to identify trace elements in the sample. More often, however, capture gamma photons are an undesired secondary source of radiation encountered in neutron shielding. The estimation of the neutron absorption rate and the subsequent production of the capture photons is an important aspect of shielding analyses.

To calculate at some position in a shield the total source strength per unit volume of capture photons of energy E_γ , it is first necessary to know the energy-dependent fluence of neutrons, $\Phi(E)$, and the macroscopic absorption coefficient, $N^i \sigma_\gamma^i(E)$, where N^i and σ_γ^i are the atomic density and microscopic, radiative-capture cross section for the i th type of nuclide in the shield medium. If $F^i(E, E_\gamma) dE_\gamma$ represents the probability of obtaining a capture photon with energy in dE_γ about E_γ when a neutron of energy E is absorbed in the i th-type nuclide, the production, per unit volume, of capture photons with energy in unit energy about E_γ is

$$S_v(E_\gamma) = \sum_{i=1}^n \int_0^{E_{\max}} dE F^i(E, E_\gamma) N^i \sigma_\gamma^i(E) \Phi(E), \quad (13)$$

where E_{\max} is the maximum neutron energy and n is the number of nuclide species in the shield material. The evaluation of (13) can be accomplished only by using sophisticated computer codes for neutron transport calculations.

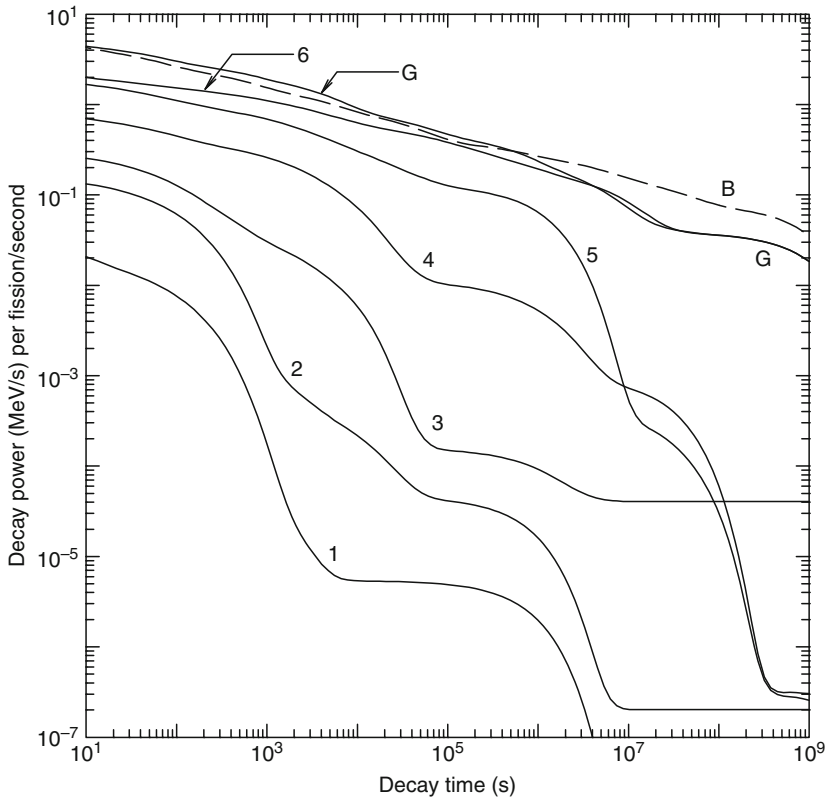


■ Figure 7

Total gamma-ray (G) and beta-particle (B) energy emission rates as a function of time after the thermal fission of ^{235}U . The curves identified by the numbers 1–6 are gamma emission rates for photons in the energy ranges 5–7.5, 4–5, 3–4, 2–3, 1–2, and 0–1 MeV, respectively

Fortunately, in most shielding situations, the evaluation of the capture photon source can be simplified considerably. The absorption cross sections are very small for energetic neutrons, typically no more than a few hundred millibarns for neutrons with energies between 10 keV and 10 MeV, and they are known with far less certainty than the scattering cross sections. The scattering cross-section for fast neutrons is always at least an order of magnitude greater than the absorption cross-section and, thus, in shielding analysis, the absorption of neutrons while they scatter and slow down is often ignored. Except in a few materials with isolated absorption resonances in the range of 1–100 eV, most of the neutron absorption occurs after the neutrons have completely slowed and assumed a speed distribution which is in equilibrium with the thermal motion of the atoms of the shielding medium. The thermal-neutron (n, γ) cross sections may be very large and in practice, the capture-gamma source calculation is usually based only on the absorption of thermal neutrons, with the epithermal and high-energy absorptions being neglected. Thus, (13) reduces to

$$S_v(E_\gamma) \simeq \sum_{i=1}^n F_{th}^i(E_\gamma) \bar{\sigma}_\gamma^i N^i \Phi_{th}, \quad (14)$$



■ Figure 8

Total gamma-ray (G) and beta-particle (B) energy-emission rates from a ^{235}U sample that has experienced a constant thermal-fission rate of one fission per second for effectively an infinite time so that the decay and production of fission products are equal. These data thus represent the worst-case situation for estimating radiation source strengths for fission products. The curves identified by the numbers 1–6 are gamma-emission rates for photons in the energy ranges 5–7.5, 4–5, 3–4, 2–3, 1–2, and 0–1 MeV, respectively

where F_{th}^i is the capture gamma spectrum arising from thermal neutron (n, γ) reactions and Φ_{th} is the neutron fluence integrated over all thermal energies. The thermal-averaged cross section $\bar{\sigma}_\gamma^i$ may be related to the 2200-m/s cross sections σ_γ^i given in ► Table 7 for selected elements, by $\bar{\sigma}_\gamma^i \approx \sqrt{\pi} \sigma_\gamma^i / 2$ (Lamarsh 1966). Capture cross sections and energy spectra of the capture photons, $F_{th}^i(E_\gamma)$ are given in ► Table 7 for selected elements.

Gamma Photons from Inelastic Neutron Scattering

The excited nucleus formed when a neutron is inelastically scattered decays to the ground state within about 10^{-14} s, with the excitation energy being released as one or more photons. Because of the constraints imposed by the conservation of energy and momentum in all scattering interactions, inelastic neutron scattering cannot occur unless the incident neutron energy is greater

Table 7

Radiative capture cross sections σ_y , and the number of capture gamma rays produced in common elements with natural isotopic abundances. The thermal capture cross sections are for 2200 m s^{-1} (0.0253 eV) neutrons in units of the barn (10^{-24} cm^2). Listed are the numbers of gamma rays produced, per neutron capture, in each of 11 energy groups

	σ_y (b)	Energy group (MeV)										
		0-1	1-2	2-3	3-4	4-5	5-6	6-7	7-8	8-9	9-10	10-11
H	3.32E-1	0.0000	0.0000	1.0000	0.0000	0.0000	0.0000	0.0000	0.0000	0.0000	0.0000	0.0000
Li	3.63E-2	0.1242	0.0491	0.8933	0.0000	0.0000	0.0000	0.0107	0.0402	0.0000	0.0000	0.0000
Be	9.20E-3	0.2641	0.0000	0.2356	0.4530	0.0000	0.0175	0.6375	0.0000	0.0000	0.0000	0.0000
B	1.03E-1	0.0000	0.0000	0.0000	0.0000	1.1014	0.0000	0.3950	0.4785	0.0000	0.0000	0.0000
Ti	6.10E+0	0.3213	0.9772	0.0832	0.1221	0.1187	0.0283	0.6089	0.0109	0.0043	0.0022	0.0003
V	5.04E+0	0.3837	0.2486	0.1335	0.0591	0.0877	0.3158	0.3947	0.1972	0.0000	0.0000	0.0000
Cr	3.10E+0	0.4051	0.1608	0.2067	0.0921	0.0421	0.1103	0.1189	0.2461	0.3766	0.1097	0.0000
Mn	1.33E+1	0.7128	0.1242	0.3838	0.2199	0.2049	0.2981	0.0949	0.3257	0.0000	0.0000	0.0000
Fe	2.55E+0	0.2781	0.2383	0.1018	0.1328	0.1137	0.1097	0.1045	0.5865	0.0087	0.0415	0.0011
Co	3.72E+1	0.9375	0.1737	0.0794	0.0920	0.1121	0.2991	0.2893	0.0980	0.0000	0.0000	0.0000
Ni	4.43E+0	0.2616	0.0658	0.0604	0.0364	0.0371	0.0746	0.1703	0.1404	0.5898	0.0000	0.0000
Cu	3.79E+0	0.8176	0.0602	0.0458	0.0588	0.0917	0.1018	0.1621	0.6488	0.0000	0.0000	0.0000
Zr	1.85E-1	0.8081	0.3048	0.2119	0.1361	0.0847	0.0820	0.1745	0.0042	0.0082	0.0000	0.0000
Mo	2.65E+0	0.8097	0.2000	0.0816	0.0416	0.0590	0.0542	0.0611	0.0074	0.0054	0.0000	0.0000
Ag	6.36E+1	0.6831	0.0166	0.0105	0.0102	0.0312	0.0877	0.0266	0.0112	0.0000	0.0000	0.0000
Cd	2.45E+3	1.0399	0.2239	0.1895	0.0736	0.0410	0.0957	0.0129	0.0073	0.0036	0.0025	0.0000
In	1.94E+2	0.3362	0.3534	0.1365	0.0311	0.0381	0.0328	0.0029	0.0000	0.0000	0.0000	0.0000

Source: Lone, Leavitt, and Harrison (1981)

than $(A+1)/A$ times the energy required to excite the scattering nucleus to its first excited state. Except for the heavy nuclides, neutron energies above about 0.5 MeV are typically required for inelastic scattering. The secondary photons produced by inelastic scattering of low-energy neutrons from heavy nuclides are generally not of interest in a shielding situation because of their low energies and the ease with which they are attenuated. Even the photons arising from inelastic scattering of high-energy neutrons (above 1 MeV) are rarely of importance in shielding analyses unless they represent the only source of photons.

The detailed calculation of secondary photon source strengths from inelastic neutron scattering requires knowledge of the fast-neutron fluence, the inelastic scattering cross sections, and spectra of resultant photons, all as functions of the incident neutron energy. Accounting accurately for inelastic scattering can be accomplished only with neutron transport codes using very detailed nuclear data. The cross sections and energy spectra of the secondary photons depend strongly on the incident neutron energy and the particular scattering nuclide. Such inelastic scattering data are known only for the more important nuclides and shielding materials, and even that known data require extensive data libraries such as that provided by

Roussin et al. (1980). Fortunately, in most analyses, these secondary photons are of little importance when compared with the eventual capture photons. Although inelastic neutron scattering is usually neglected with regard to its secondary-photon radiation, such scattering is a very important mechanism in the attenuation of the fast neutrons, better even than elastic scattering in some cases.

Activation Gamma Photons

For many materials, absorption of a neutron produces a radionuclide with a half-life ranging from a fraction of a second to many years. The radiation produced by the subsequent decay of these activation nuclei may be very significant for materials that have been exposed to large neutron fluences, especially structural components in a reactor core. Most radionuclides encountered in research laboratories, medical facilities, and industry are produced as activation nuclides from neutron absorption in some parent material. Such nuclides decay, usually by beta emission, leaving the daughter nucleus in an excited state which usually decays quickly (within 10^{-14} s) to its ground state with the emission of one or more gamma photons. Thus, the apparent half-life of the photon emitter is that of the parent (or activation nuclide), while the number and energy of the photons is characteristic of the nuclear structure of the daughter.

Although most activation products of concern in shielding problems arise from neutron absorption, there is one important exception in water-moderated reactors. The ^{16}O in the water can be transmuted to ^{16}N in the presence of fission neutrons by an (n, p) reaction with a threshold energy of 9.6 MeV. The activation cross section, averaged over the fission spectrum, is 0.019 mb (Jaeger 1968) and although reactions with such small cross sections are rarely important, ^{16}N decays with a 7.4-s half-life emitting gamma photons of 6.13 and 7.10 MeV (yields of 0.69 and 0.05 per decay). This activity may be very important in coolant channels of power reactors.

1.2.4 X-Ray Sources

As photons and charged particles interact with matter, secondary X-rays are inevitably produced. Because X-rays in most shielding applications usually have energies $\lesssim 100$ keV, they are easily attenuated by any shield adequate for the primary radiation. Consequently, the secondary X-rays are often completely neglected in analyses involving higher-energy photons. However, for those situations in which X-ray production is the only source of photons, it is important to estimate the intensity, energies, and the resulting exposure of the X-ray photons. There are two principal methods whereby secondary X-ray photons are generated: the rearrangement of atomic electron configurations leads to characteristic X-rays, and the deflection of charged particles in the nuclear electric field results in bremsstrahlung. Both mechanisms are briefly discussed as follows.

Characteristic X Rays

If the normal electron arrangement around a nucleus is altered through ionization of an inner electron or through excitation of electrons to higher energy levels, the electrons begin a complex series of transitions to vacancies in the lower shells (thereby acquiring higher binding energies) until the unexcited state of the atom is achieved. In each electronic transition, the difference in the binding energy between the final and initial states is either emitted as a photon, called a

characteristic X ray, or given up to an outer electron, which is ejected from the atom and is called an *Auger electron*. The discrete electron energy levels and the transition probabilities between levels vary with the Z number of the atom and, thus, the characteristic X rays provide a unique signature for each element.

The number of X rays with different energies is greatly increased by the multiplicity of electron energy levels available in each shell (1, 3, 5, 7,... distinct energy levels for the K, L, M, N, \dots shells, respectively). Fortunately, in shielding applications such detail is seldom needed, and often only the dominant K series of X rays is considered, with a single representative energy being used for all X rays.

There are several methods commonly encountered in shielding applications, whereby atoms may be excited and characteristic X rays produced. A photoelectric absorption leaves the absorbing atom in an ionized state. If the incident photon energy is sufficiently greater than the binding energy of the K -shell electron, which ranges from 14 eV for hydrogen to 115 keV for uranium, it is most likely (80–100%) that a vacancy is created in the K shell and, thus, that the K series of X rays dominates the subsequent secondary radiation. These X-ray photons produced from photoelectric absorption are often called *fluorescent radiation*.

Characteristic X rays can also arise following the decay of a radionuclide. In the decay process known as *electron capture*, an orbital electron, most likely from the K shell, is absorbed into the nucleus, thereby decreasing the nuclear charge by one unit. The resulting K -shell vacancy then gives rise to the K series of characteristic X rays. A second source of characteristic X rays, which occurs in many radionuclides, is a result of *internal conversion*. Most daughter nuclei formed as a result of any type of nuclear decay are left in excited states. This excitation energy may be either emitted as a gamma photon or transferred to an orbital electron which is ejected from the atom. Again it is most likely that a K -shell electron is involved in this internal conversion process.

Bremsstrahlung

A charged particle gives up its kinetic energy either by collisions with electrons along its path or by photon emission as it is deflected, and hence accelerated, by the electric fields of nuclei. The photons produced by the deflection of the charged particle are called *bremsstrahlung* (literally, “braking radiation”).

The kinetic energy lost by a charged particle of energy E , per unit path length of travel, to electron collisions (which excites and ionizes ambient atoms) and to bremsstrahlung is denoted by L_{coll} and L_{rad} , the collisional and radiative *stopping powers*, respectively. For a relativistic particle of rest mass M (i.e., $E \gg Mc^2$) slowing in a medium with atomic number Z , it can be shown that the ratio of radiative to ionization losses is approximately (Evans 1955)

$$\frac{L_{\text{rad}}}{L_{\text{coll}}} \simeq \frac{EZ}{700} \left(\frac{m_e}{M} \right)^2, \quad (15)$$

where E is in MeV. From this result, it is seen that bremsstrahlung is more important for high-energy particles of small mass incident on high- Z material. In shielding situations, only electrons ($m_e/M = 1$) are ever of importance for their associated bremsstrahlung. All other charged particles are far too massive to produce significant amounts of bremsstrahlung. Bremsstrahlung from electrons, however, is of particular radiological interest for devices that accelerate electrons, such as betatrons and X-ray tubes, or for situations involving radionuclides that emit only beta particles.

For monoenergetic electrons of energy E_o incident on a target thick when compared with the electron range, the number of bremsstrahlung photons of energy E , per unit energy and per incident electron, emitted as the electron is completely slowed down can be approximated by the distribution (Wyard 1952)

$$N_{br}(E_o, E) = 2kZ \left[\left(\frac{E_o}{E} - 1 \right) - \frac{3}{4} \ln \left(\frac{E_o}{E} \right) \right], \quad E \leq E_o, \quad (16)$$

where k is a normalization constant independent of E . The fraction of the incident electron's kinetic energy that is subsequently emitted as bremsstrahlung can then be calculated from this approximation as

$$Y(E_o) = \frac{1}{E_o} \int_0^{E_o} dE EN_{br}(E_o, E) = \frac{13}{16} kZE_o, \quad (17)$$


which is always a small fraction for realistic shielding situations. For example, only 4% of the energy of a 0.5-MeV electron, when stopped in lead, is converted into bremsstrahlung. Equation (17) can be used to express the normalization constant k in terms of the radiation yield $Y(E_o)$, namely $kZ = 16Y(E_o)/(13E_o)$, where $Y(E_o)$ can be found from tabulated values (ICRU 1984). With this choice for k , the approximation of (16) agrees quite well with the thick-target bremsstrahlung spectrum calculated by much more elaborate methods, such as the continuous slowing-down model.

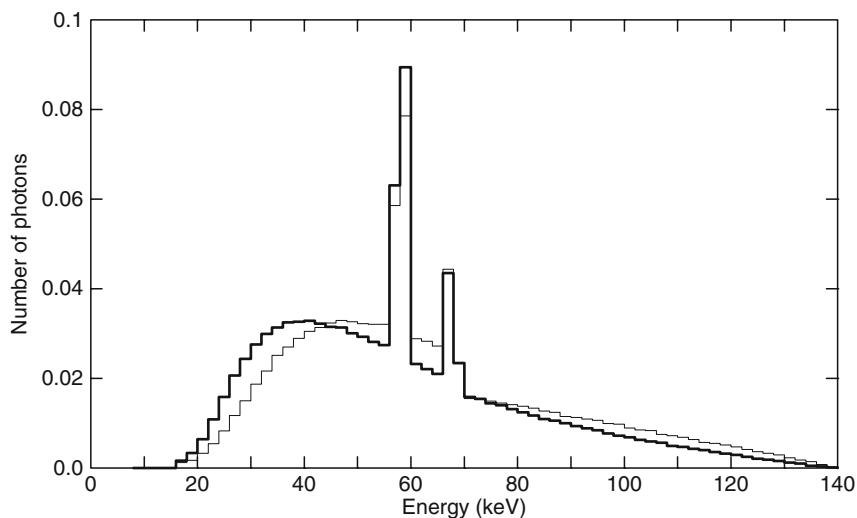
The electrons and positrons emitted by radionuclides undergoing beta decay produce bremsstrahlung as they slow down in the source material. However, these photons generally are of negligible importance in radiation shielding situations because the gamma and X-ray photons usually produced in radioactive decay are more numerous and penetrating than the bremsstrahlung. Only for the case of pure beta-particle emitters is beta-particle bremsstrahlung possibly of interest.

During the beta-decay process, the beta particle is accelerated, and consequently, a small amount of bremsstrahlung is emitted. These X rays, called "inner" bremsstrahlung, can be ignored in shielding analyses because only a small fraction of the beta-decay energy, on the average, is emitted as this type of radiation.

X-Ray Machines

The production of X-ray photons as bremsstrahlung and fluorescence occurs in any device that produces high-energy electrons. Devices that can produce significant amount of X rays are those in which a high voltage is used to accelerate electrons, which then strike an appropriate target material. Such is the basic principle of all X-ray tubes used in medical diagnosis and therapy, industrial applications, and research laboratories.

The energy spectrum of X-ray photons emitted from an X-ray tube has a continuous bremsstrahlung component up to the maximum electron energy (i.e., the maximum voltage applied to the tube). If the applied voltage is sufficiently high as to cause ionization in the target material, there will also be characteristic X-ray lines superimposed on the continuous bremsstrahlung spectrum. In  Fig. 9, two X-ray energy spectra are shown for the same operating voltage but for different amounts of beam filtration (i.e., different amounts of material attenuation in the X-ray beam). As the beam filtration increases the low-energy X rays are preferentially attenuated, and the X-ray spectrum hardens and becomes more penetrating. Also readily apparent in these spectra are the tungsten $K_{\alpha 1}$ and $K_{\beta 1}$ characteristic X rays.



■ Figure 9

Measured photon spectra from a Machlett Aeromax X-ray tube (tungsten anode) operated at a constant 140 kV potential. This tube has an inherent filter thickness of 2.50-mm aluminum equivalent and produces the spectrum shown by the thick line. The addition of an external 6-mm aluminum filter hardens the spectrum shown by the thin line. Both spectra are normalized to unit area. Data are from Fewell, Shuping, and Hawkins [1981]

Traditionally, the output from a particular X-ray machine is expressed by a parameter K_o ($\text{R mA}^{-1} \text{ min}^{-1}$), which is the exposure in the beam (expressed in roentgens) at a specified distance from the tube focal spot (usually 1 m) that would be produced by a 1-mA tube current of 1-min duration. This performance parameter is usually assumed to be known when making analyses for X-ray shielding around a particular machine because it depends greatly on the operating voltage and the degree of beam filtering.

2 Conversion of Fluence to Dose

The *dose conversion coefficient* (ICRP 1987) provides the link between the physical description of a radiation field, namely the fluence and some measure of radiation dose or radiation sensor response. There are two main classes of dose conversion coefficients. One class, the *local* conversion coefficient, converts the energy spectrum of the fluence at a point, $\Phi(\mathbf{r}, E)$ to the point value of the dose (kerma, exposure, absorbed dose, or effective dose). The other class of dose conversion coefficients, sometimes called *phantom related*, makes use of local fluences and dose coefficients within geometric or anthropomorphic phantoms to evaluate risk-related average or effective doses of various types. Geometric phantoms are used for evaluation of operational dose quantities such as the ambient dose, which is correlated with monitored occupational exposure. Effective doses associated with anthropomorphic phantoms are used prospectively for planning and optimization of protection, and retrospectively for demonstration of compliance with dose limits or for comparing with dose constraints or reference levels. These phantom related

coefficients account for the relative radiation sensitivities of the various organs and tissues and the relative biological effectiveness of different radiations.

In the extreme, a receiver with volume V might have a sensitivity that depends on the radiation's energy and direction and where in V the radiation interacts, so the dose or response is

$$R = \int_0^\infty dE \int_{4\pi} d\Omega \int_V dV \mathcal{R}(\mathbf{r}, E, \Omega) \Phi(\mathbf{r}, E, \Omega), \quad (18)$$

in which R is the response, $\Phi(\mathbf{r}, E, \Omega)$ is the fluence, and $\mathcal{R}(\mathbf{r}, E, \Omega)$ is the dose conversion coefficient or response function. For many cases, the receiver is a point and the response is isotropic, so that

$$R(\mathbf{r}) = \int_0^\infty dE \mathcal{R}(E) \Phi(\mathbf{r}, E). \quad (19)$$

Fluence-to-dose conversion is accomplished internally within calculations using point-kernel codes such as Isoshield, Microshield, and the QAD series of codes. The same is true for multi-group codes such as the DOORS and PARTISN series and, in general, it is necessary for the user to provide data tables for dose conversion coefficients. With Monte Carlo codes, such as MCNP, the absorbed dose or kerma may be computed directly or the energy-dependent fluence may be first computed and then dose conversion coefficients applied to the results.

2.1 Local Dosimetric Quantities

Dosimetric quantities are intended to provide, at a point or in a region of interest, a physical measure correlated with a radiation effect. The radiometric quantity called the fluence is not closely enough related to most radiation effects to be a useful determinant. Energy fluence appears to be more closely correlated with radiation effect than is fluence alone, because the energy carried by a particle must have some correlation with the damage it can do to material such as biological matter. This choice is not entirely adequate – not even for particles of a single type. One must examine more deeply the mechanism of the effect of radiation on matter in order to determine what properties of the radiation are best correlated with its effects, especially its biological hazards. One must account for energy transfer from the primary radiation, neutrons or photons in this context, to the absorbing medium at the microscopic level. One must then account for the creation of secondary charged particles and, as well, tertiary particles such as X-rays created as charged particles are stopped.

2.1.1 Energy Imparted and Absorbed Dose

For a given volume of matter of mass m , the energy ϵ imparted in some time interval is the sum of the energies (excluding rest-mass energies) of all charged and uncharged ionizing particles entering the volume minus the sum of the energies (excluding rest-mass energies) of all charged and uncharged ionizing particles leaving the volume, further corrected by subtracting the energy equivalent of any increase in rest-mass energy of the material in the volume. Thus, the energy imparted is that which is involved in the ionization and excitation of atoms and molecules within the volume and the associated chemical changes. This energy is eventually degraded almost entirely into thermal energy. The *specific energy* $z \equiv \epsilon/m$, the energy imparted per unit mass, leads to the absorbed dose quantity.

The *absorbed dose* is the quotient of the *mean* energy imparted $\bar{\epsilon}$ to matter of mass m , in the limit as the mass approaches zero (ICRU 1971). Or it may be written in differential form, namely,

$$D \equiv \lim_{m \rightarrow 0} \bar{z} = \frac{d\bar{\epsilon}}{dm}. \quad (20)$$

The standard unit of absorbed dose is the gray (Gy), 1 Gy being equal to an imparted energy of 1 joule per kilogram. A traditional unit for absorbed dose is the rad, defined as 100 ergs per gram. Thus, 1 rad = 0.01 Gy.

The concept of absorbed dose is very useful in radiation protection. Energy imparted per unit mass in tissue is closely, but not perfectly, correlated with radiation hazard.

2.1.2 Kerma

The absorbed dose is a measurable quantity, but in many circumstances it is difficult to calculate from the incident radiation fluence and material properties because such a calculation would require a detailed accounting of the energies of all secondary particles leaving the volume of interest. A closely related deterministic quantity, used only in connection with indirectly ionizing (uncharged) radiation, is the *kerma*, an acronym for *kinetic energy of radiation produced per unit mass in matter*. If E_{tr} is the sum of the initial kinetic energies of all the charged ionizing particles released by interaction of indirectly ionizing particles in matter of mass m , then

$$K \equiv \lim_{m \rightarrow 0} \frac{\bar{E}_{tr}}{m} = \frac{d\bar{E}_{tr}}{dm}, \quad (21)$$

where \bar{E}_{tr} is the mean or expected energy transferred to the secondary charged particles in the mass m . That some of the initial kinetic energy may be transferred ultimately to bremsstrahlung and lost from m , for example, is irrelevant. The kerma is relatively easy to calculate (requiring knowledge of only the initial interactions), but is hard to measure (because all the initial kinetic energy of the charged particles may not be deposited in m).

The use of the kerma requires the specification of the material present in the incremental volume, possibly hypothetical, used as an idealized receptor of radiation. Thus, one may speak conceptually of tissue kerma in a concrete shield or in a vacuum, even though the incremental volume of tissue may not be actually present.

Absorbed dose and kerma are frequently almost equal in magnitude. Under a condition known as *charged particle equilibrium*, they are equal. This equilibrium exists in an incremental volume about a point of interest if, for every charged particle leaving the volume, another of the same type and with the same kinetic energy enters the volume traveling in the same direction. In many practical situations, this charged particle equilibrium is closely achieved so that the kerma is a close approximation of the absorbed dose.

2.1.3 Exposure

The quantity called *exposure*, with abbreviation X , is used traditionally to specify the radiation field of gamma or X-ray photons. It is defined as the absolute value of the ion charge of one

sign produced anywhere in air by the complete stoppage of all negative and positive electrons, except those produced by bremsstrahlung, that are liberated in an incremental volume of air, per unit mass of air in that volume. The exposure is closely related to air kerma but differs in one important respect. The phenomenon measured by the interaction of the photons in the incremental volume of air is not the kinetic energy of the secondary electrons but the ionization caused by the further interaction of these secondary electrons with air. The SI unit of exposure is coulombs per kilogram. The traditional unit is the roentgen, abbreviated R, which is defined as precisely 2.58×10^{-4} coulomb of separated charge of one sign per kilogram of air in the incremental volume where the primary photon interactions occur.

Kerma in air and exposure are very closely related. A known proportion of the initial kinetic energy of secondary charged particles results in ionization of the air, namely, 33.85 ± 0.15 electron volts of kinetic energy per ion pair (ICRU 1979). The product of this factor and the air kerma, with appropriate unit conversions, is the exposure X . The product, however, must be reduced slightly to account for the fact that some of the original energy of the secondary electrons may result in bremsstrahlung, not in ionization or excitation.

2.1.4 Local Dose Equivalent Quantities

If the energy imparted by ionizing radiation per unit mass of tissue were by itself an adequate measure of biological hazard, absorbed dose would be the best dosimetric quantity to use for radiation protection purposes. However, there are also other factors to consider that are related to the spatial distribution of radiation-induced ionization and excitation. The charged particles responsible for the ionization may themselves constitute the primary radiation, or may arise secondarily from interactions of uncharged, indirectly ionizing, primary radiation.

Relative Biological Effectiveness

In dealing with the fundamental behavior of biological material or organisms subjected to radiation, one needs to take into account variations in the sensitivity of the biological material to different types or energies of radiation. For this purpose, radiobiologists define a *relative biological effectiveness* (RBE) for each type and energy of radiation, and, indeed, for each biological effect or *endpoint*. The RBE is the ratio of the absorbed dose of a reference type of radiation (typically, 250-kVp X-rays or ^{60}Co gamma rays) producing a certain kind and degree of biological effect to the absorbed dose of the radiation under consideration required to produce the same kind and degree of effect. RBE is normally determined experimentally and takes into account all factors affecting biological response to radiation in addition to absorbed dose.

Linear Energy Transfer

As a charged particle moves through matter it slows, giving up its kinetic energy through (a) Coulombic interactions with ambient atomic electrons causing ionization and excitation of the atoms and (b) radiative energy loss by the emission of bremsstrahlung (important only for electrons). The *stopping power* or unrestricted linear energy transfer, LET, L_∞ , often denoted as $-dE/dx$, is the expected energy loss per unit distance of travel by the charged particle.

The larger the LET of a radiation particle the more the ionization, and hence the biological damage, it causes per unit travel distance. Calculation of the LET is accomplished efficiently using one of the STAR Codes (Berger et al. 2005). Representative results are summarized by Shultis and Faw (2000).

Radiation Weighting Factor and Dose Equivalent

The RBE depends on many variables: the physical nature of the radiation field, the type of biological material, the particular biological response, the degree of response, the radiation dose, and the dose rate or dose fractionation. For this reason, it is too complicated a concept to be applied in the routine practice of radiation protection or in the establishment of broadly applied standards and regulations. Since 1964, a surrogate quantity called the *quality factor* Q (not to be confused with the Q value of a nuclear reaction) has been applied to the local value of the absorbed dose to yield a quantity called the *dose equivalent* H , recognized as an appropriate measure of radiation risk when applied to operational dosimetry. As is discussed below, the quality factor is also applied to evaluation of geometric-phantom related doses such as the ambient dose. Note that “the dose equivalent is based on the absorbed dose at a point in tissue which is weighted by a distribution of quality factors which are related to the LET distribution at that point” (NCRP 1993).

Because the spatial density of ionization and excitation along particle tracks is believed to be an important parameter in explaining the variations in biological effects of radiation of different types and energies, and because the density is clearly proportional to linear energy transfer (LET), the quality factor was defined in terms of LET. In particular, because tissue is largely water and has an average atomic number close to that of water, the quality factor was made a mathematical function of the unrestricted LET in water, L_∞ (ICRP 2007).

$$Q(L_\infty) = \begin{cases} 1 & L_\infty < 10 \text{ keV}/\mu\text{m} \\ 0.32L_\infty - 2.2 & 10 \leq L_\infty \leq 100 \text{ keV}/\mu\text{m} \\ 300/\sqrt{L_\infty} & L_\infty > 100 \text{ keV}/\mu\text{m}. \end{cases} \quad (22)$$

To ascribe a quality factor to some particular primary radiation, whether that primary radiation be directly or indirectly ionizing, more information is needed about the nature of the energy deposition. In principle, one must first determine how the absorbed dose is apportioned among particles losing energy at different LETs. One may then account for the variability of Q with L_∞ and determine an average quality factor \bar{Q} .

Quality factors can be ascribed to uncharged ionizing radiation through a knowledge of the properties of the secondary charged particles they release upon interaction with matter. Because secondary electrons released by gamma rays or X-rays are always assigned a quality factor of unity, the same factor applies universally to all ionizing photons. The situation for neutrons is not so simple, and average values must be determined as indicated in the following discussion.

Closely related to the quality factor is the *radiation weighting factor* w_R , introduced by the ICRP in 1991 and modified in 2007, for use with the dose equivalent in tissues of the anthropomorphic phantom and addressed in [2.3.3](#). The SI unit of the dose equivalent H is the sievert, abbreviated as Sv. [Table 8](#) compares quality factors specified by

■ Table 8

Mean quality factors Q or radiation weighting factors w_R adopted by the ICRP (2007) and by the US Nuclear Regulatory Commission (1991), based on NCRP (1971). They apply to the radiation incident on the body or, for internal sources, emitted from the source

Radiation	USNRC ^a	ICRP (2007) ^b
Gamma- and X-rays of all energies	1	1
Electrons and muons of all energies	1	1
Protons, other than recoil	10	2
Alpha particles, fission fragments, heavy nuclei	20	20
Neutrons		
MeV		
0.0001	2	2.5
0.001	2	2.5
0.01	2.5	3.0
0.1	7.5	10.0
0.5	11	19.3
1	11	20.7
2.5	9	16.0
5	8	12.0
7	7	10.3
10	6.5	8.8
14	7.5	7.7
20	8	6.8
40	7	5.7
60	5.5	5.4
100	4	4.9

^aNeutron data based on a 30-cm diameter cylinder tissue-equivalent phantom

^bThe neutron radiation weighting factor is computed from (23)

the US Nuclear Regulatory Commission (NCRP 1971, USNRC 1991) and radiation weighting factors specified by the ICRP (2007). The 2007 formulation computes neutron weighting factors as

$$w_R = \begin{cases} 2.5 + 18.2 \exp[-\ln^2(E)/6], & E < 1 \text{ MeV}, \\ 5.0 + 17 \exp[-\ln^2(2E)/6], & 1 \text{ MeV} \leq E \leq 50 \text{ MeV}, \\ 2.5 + 3.25 \exp[-\ln^2(0.04E)/6], & E > 50 \text{ MeV}. \end{cases} \quad (23)$$

2.2 Evaluation of Local Dose Conversion Coefficients

2.2.1 Photon Kerma, Absorbed Dose, and Exposure

If $\mu(E)$ is the total interaction coefficient (less coherent scattering), $f(E)$ is the fraction of the photon's energy E transferred to secondary charged particles and ρ is the material density, the kerma is given by

$$K = \left(\frac{f(E)\mu(E)}{\rho} \right) E\Phi(E). \quad (24)$$

The quantity $f(E)\mu(E)$ is called the linear *energy transfer* coefficient μ_{tr} . For energy E in units of MeV, Φ in units of cm^{-2} , the mass energy transfer coefficient $\mu_{tr}(E)/\rho$ in units of cm^2/g , and the conversion coefficient \mathcal{R}_K in units of Gy cm^2 ,

$$\mathcal{R}_K(E) = 1.602 \times 10^{-10} E \left(\frac{\mu_{tr}(E)}{\rho} \right), \quad (25)$$

in which $\mu_{tr}(E)$ is averaged on the basis of weight fractions of each element in the transport medium at the point of interest.

If the secondary charged particles produce substantial bremsstrahlung, a significant portion of the charged-particles' kinetic energy is reradiated away as bremsstrahlung from the region of interest. Even under charged-particle equilibrium, the kerma may overpredict the absorbed dose. The production of bremsstrahlung can be taken into account by the substitution in (25) of the mass energy absorption coefficient $\mu_{en}/\rho = [1 - G(E)]\mu_{tr}/\rho$, where $G(E)$ is the fraction of the secondary-charged particle's initial kinetic energy radiated away as bremsstrahlung. Then, under the assumptions of charged-particle equilibrium and no local energy transfer from bremsstrahlung,

$$\mathcal{R}_D(E) = 1.602 \times 10^{-10} E \left(\frac{\mu_{en}(E)}{\rho} \right). \quad (26)$$

Extensive table of μ_{en}/ρ values are available on line (Hubbell and Seltzer 2004).

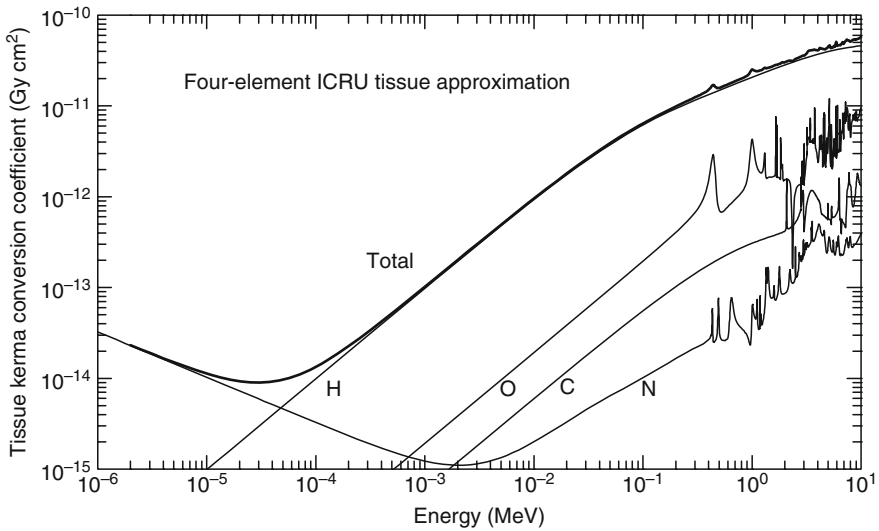
For exposure in units of roentgen, E in MeV, (μ_{en}/ρ) for air in cm^2/g , and Φ in cm^{-2} ,

$$X = 1.835 \times 10^{-8} E \left(\frac{\mu_{en}(E)}{\rho} \right)_{\text{air}} \Phi. \quad (27)$$

2.2.2 Neutron Kerma and Absorbed Dose

Charged particle equilibrium is, in most instances, closely approached in neutron transport, so that the kerma is an excellent approximation of the absorbed dose. The local dose conversion coefficient, in units of Gy cm^2 is given by

$$\mathcal{R}_K(E) = 1.602 \times 10^{-10} \sum_i \frac{N_i}{\rho} \sum_j \sigma_{ji}(E) \epsilon_{ji}(E), \quad (28)$$



■ Figure 10

Kerma dose conversion coefficient for neutron interactions in the ICRU four-element approximation for tissue, with mass fractions: 0.101 H, 0.111 C, 0.026 N, and 0.762 O. Computed using NJOY-processed ENDF/B-V data

in which ρ is the material density (g/cm^3), N_i (cm^{-3}) is the density of atomic species i , $\sigma_{ji}(E)$ is the cross-section (cm^2) for nuclear reaction j with atomic species i , and $\epsilon_{ji}(E)$ (MeV) is the energy transferred to the medium in that same reaction. ➤ Figure 10 illustrates the neutron-kerma dose conversion coefficient for a four-element tissue approximation.

2.3 Phantom-Related Dosimetric Quantities

2.3.1 Characterization of Ambient Radiation

A problem very often encountered in radiation shielding is as follows. At a given reference point representing a location accessible to the human body, the radiation field has been characterized in terms of the fluxes or fluences of radiations of various types computed in the *free field*, that is, in the absence of the body. Suppose for the moment that only a single type of radiation is involved, say either photons or neutrons, and the energy spectrum $\Phi(E)$ of the fluence is known at the reference point. What is needed is the ability to define and to calculate, at *that point* and for *that single type of radiation*, a dose quantity R for a phantom representation of the human subject, which can be calculated using an appropriate conversion coefficient, or response function \mathcal{R} , as

$$R = \int_0^{\infty} dE \mathcal{R}(E) \Phi(E), \quad (29)$$

analogous to (19). Here \mathcal{R} is a phantom-related conversion coefficient and Φ is the fluence energy spectrum, not perturbed by the presence of the phantom. Generation of the conversion coefficient, of course, requires determination of the absorbed dose and accounting for the radiation transport inside a phantom resulting from incident radiation with a carefully defined angular distribution (usually, a parallel beam).

Suppose one knows the angular and energy distributions of the fluence of ionizing radiation at a point in space, that is, the radiation field at the point. Both operational and limiting dose quantities are evaluated as radiation doses in phantoms irradiated by a *uniform* radiation field derived from the actual radiation field at the point. In the *expanded field*, the phantom is irradiated over its entire surface by radiation whose energy and angular distributions are the same as those in the actual field at the point of interest. In the *expanded and aligned field*, the phantom is irradiated by unidirectional radiation whose energy spectrum is the same as that in the actual field at the point.

2.3.2 Dose Conversion Factors for Geometric Phantoms

Of the geometrically simple mathematical phantoms, the more commonly used is the *ICRU sphere* of 30 cm diameter with density 1.0 g/cm^3 and of tissue-equivalent composition, by weight—76.2% oxygen, 11.1% carbon, 10.1% hydrogen, and 2.6% nitrogen. The dose quantity may be the maximum dose within the phantom or the dose at some appropriate depth.

Dose conversion coefficients for the phantoms are computed for a number of irradiation conditions, for example, a broad parallel beam of monoenergetic photons or neutrons. At selected points or regions within the phantom, absorbed-dose values, often approximated by kerma values, are determined. In this determination, contributions by all secondary-charged particles at that position are taken into account; and for each type of charged particle of a given energy, the L_∞ value in water and, therefore, Q are obtained. These are then applied to the absorbed-dose contribution from each charged particle to obtain the dose-equivalent contribution at the given location in the phantom. The resulting distributions of absorbed dose and dose equivalent throughout the phantom are then examined to obtain the maximum value, or the value otherwise considered to be in the most significant location, say at 10 mm depth. The prescribed dose conversion coefficient is then that value of either absorbed dose or dose equivalent divided by the fluence of the incident beam.

These conversion coefficients are intended for operational dose quantities and are designed to provide data for radiation protection purposes at doses well below limits for public exposure. The dose quantities may be treated as point functions, determined exclusively by the radiation field in the vicinity of a point in space. Application of the conversion coefficients for these dose quantities is explained in depth by the ICRU (1988).

Deep Dose Equivalent Index

For this dose quantity, $H_{1,d}$, the radiation field is assumed to have the same fluence and energy distribution as those at a reference point, but expanded to a broad parallel beam striking the phantom. The dose is the maximum dose equivalent within the 14-cm-radius central core of the ICRU sphere. There are difficulties in using this dose quantity when the incident radiation is polyenergetic or consists of both neutrons and gamma rays. The reason is that the depth at

which the dose is maximum varies from one type of radiation to another or from one energy to another. Thus, this quantity is nonadditive.

Shallow Dose Equivalent Index

This dose quantity, $H_{I,s}$, is very similar to the deep dose-equivalent index, except that the dose equivalent is the maximum value between depths 0.007 and 0.010 cm from the surface of the ICRU sphere (corresponding to the depths of radiosensitive cells of the skin).

Ambient Dose Equivalent

For this dose, $H^*(d)$, the radiation field is assumed to have the same fluence and energy distribution as those at a reference point but expanded to a broad parallel beam striking the phantom. The dose equivalent is evaluated at depth d , on a radius opposing the beam direction. This calculated dose quantity is associated with the measured *personal dose equivalent* $H_p(d)$, the dose equivalent in soft tissue below a specified point on the body, at depth d . For weakly penetrating radiation, depths of 0.07 mm for the skin and 3 mm for the lens of the eye are employed. For strongly penetrating radiation, a depth of 10 mm is employed.

Directional Dose Equivalent

For this dose quantity, $H'(d, \Omega)$, the angular and energy distributions of the fluence at a point of reference are assumed to apply over the entire phantom surface. The depths at which the dose equivalent is evaluated are the same as those for the ambient dose equivalent. The specification of the angular distribution, denoted symbolically by argument Ω , requires specification of a reference system of coordinates in which directions are expressed. In the particular case of a unidirectional field, $H'(d, \Omega)$ may be written as $H'(d)$ and is equivalent to $H^*(d)$.

Irradiation Geometries for Spherical Phantoms

Photon and neutron conversion coefficients for deep and shallow indices and for directional dose equivalents at depths of 0.07, 3, and 10 mm have been calculated for radiation protection purposes and have been tabulated by the ICRP (1987) for the following irradiation geometries: (a) PAR, a single-plane parallel beam, (b) OPP, two opposed plane parallel beams, (c) ROT, a rotating-plane parallel beam (i.e., a plane-parallel beam with the sphere rotating about an axis normal to the beam), and (d) ISO, an isotropic radiation field.

For a single plane parallel beam, the more conservative of the irradiation geometries, the conversion coefficients for $H_{I,d}$ and $H^*(d)$ at 10 mm are almost identical for photons. For neutrons, the two differ only at low energies, with the deep dose equivalent index being greater and thus more conservative.

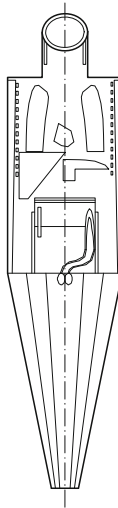
Slab and Cylinder Phantoms

Dose conversion coefficients are also available for plane parallel beams incident on slabs and on cylinders with axes normal to the beam. Slab-phantom deep-dose conversion coefficients are tabulated by the ICRP (1987) for high-energy photons and neutrons. Cylinder-phantom deep-dose coefficients reported by the NCRP (1971) are of special interest in that they are employed in US federal radiation protection regulations (USNRC 1991).

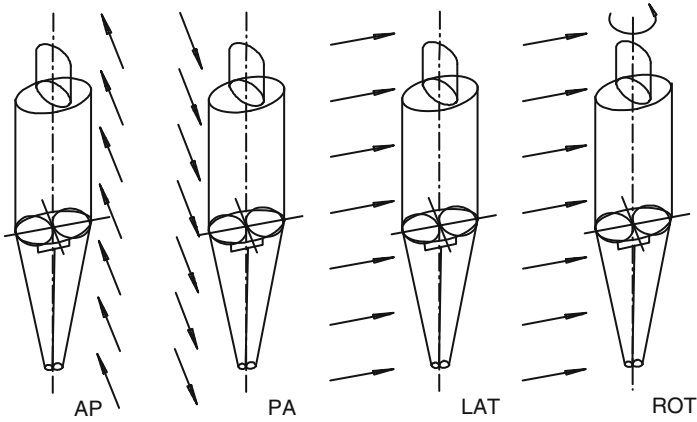
2.3.3 Dose Coefficients for Anthropomorphic Phantoms

The effective dose equivalent H_E and the effective dose \mathcal{E} are limiting doses based on an anthropomorphic phantom for which doses to individual organs and tissues may be determined. Averaging the individual doses with weight factors related to radiosensitivity leads to the effective dose or effective dose equivalent. In many calculations, a single phantom represents the adult male or female. In other calculations, separate male and female phantoms are used. These dose quantities have been developed for radiation-protection purposes in occupational and public health and, to some extent, in internal dosimetry as applied to nuclear-medicine procedures. The dose quantities apply, on average, to large and diverse populations, at doses well below annual limits. Their use in assessment of health effects for an individual subject requires a very careful judgment. One male phantom, Adam, is illustrated in ► Fig. 11. Adam has a companion female phantom, named Eva (Kramer et al. 1982). In yet other calculations (Cristy and Eckerman 1987), a suite of phantoms is available for representation of the human at various ages from the newborn to the adult. The many phantoms used for measurements or calculations are described in ICRU Report 48 (1992).

Anthropomorphic phantoms are mathematical descriptions of the organs and tissues of the human body, formulated in such a way as to permit calculation or numerical simulation of the transport of radiation throughout the body. In calculations leading to conversion coefficients, monoenergetic radiation is incident on the phantom in fixed geometry. One geometry leading to conservative values of conversion coefficients is *anteroposterior* (AP), irradiation from the front to the back with the beam at right angles to the long axis of the body. Other geometries, *posteroanterior* (PA), *lateral* (LAT), *rotational* (ROT), and *isotropic* (ISO) are illustrated in ► Fig. 12. The ROT case is thought to be an appropriate choice for the irradiation pattern experienced by a person moving unsystematically relative to the location of a radiation



■ Figure 11
Sectional view of the male anthropomorphic phantom used in calculation of the effective dose



■ Figure 12

Irradiation geometries for the anthropomorphic phantom. From ICRP (1987)

source. However, the AP case, being most conservative, is the choice in the absence of particular information on the irradiation circumstances.

Effective Dose Equivalent

In 1977, the ICRP introduced the effective dose equivalent H_E , defined as a weighted average of mean dose equivalents in the tissues and organs of the human body, namely,

$$H_E = \sum_T \omega_T D_T Q_T, \quad (30)$$

in which D_T is the mean absorbed dose in organ T and Q_T is the corresponding mean quality factor. If m_T is the mass of organ or tissue T , then

$$Q_T = \frac{1}{m_T} \int dm QD = \frac{1}{m_T} \int dm \int dL_\infty D(L_\infty) Q(L_\infty), \quad (31)$$

in which $D(L_\infty) dL_\infty$ is that portion of the absorbed dose attributable to charged particles with LETs in the range dL_∞ about L_∞ . Tissue weight factors to be used with the effective dose equivalent are listed in [Table 9](#). They are determined by the relative sensitivities for stochastic radiation effects such as cancer and first-generation hereditary illness. The 1977 values are still of importance because of their implicit use in federal radiation protection regulations [USNRC 1991] in the United States.

Effective Dose

In 1991, the ICRP recommended a replacement of the effective dose equivalent by the effective dose. This recommendation was endorsed in 1993 by the NCRP in the United States and modified by the ICRP in 2007. The effective dose \mathcal{E} is defined as follows. Suppose that the body is irradiated externally by a mixture of particles of different type and different energy, the different radiations being identified by the subscript R . The effective dose may then be determined as

$$\mathcal{E} = \sum_T \omega_T H_T = \sum_T \omega_T \sum_R \omega_R D_{T,R}, \quad (32)$$

■ **Table 9**

Tissue weight factors adopted by the ICRP (1991, 2007) and the NCRP (1993) for use in determination of the effective dose

Organ	ICRP (1977) USNRC (1991)	ICRP (1991) NCRP (1993)	ICRP (2007)
Gonads	0.25	0.20	0.08
Bone marrow (red)	0.12	0.12	0.12
Lung	0.12	0.12	0.12
Breast	0.15	0.05	0.12
Thyroid	0.03	0.05	0.04
Bone surfaces	0.03	0.01	0.01
Remainder	0.30 ^a	0.05 ^b	0.12 ^c
Colon ^d	–	0.12	0.12
Stomach	–	0.12	0.12
Bladder	–	0.05	0.04
Liver	–	0.05	0.04
Oesophagus	–	0.05	0.04
Skin	–	0.01	0.01
Salivary glands	–	–	0.01
Brain	–	–	0.01

^aA weight of 0.06 is applied to each of the five organs or tissues of the remainder receiving the highest dose equivalents, the components of the GI system being treated as separate organs

^bThe remainder is composed of the following additional organs and tissues: adrenals, brain, small intestine, large intestine, kidney, muscle, pancreas, spleen, thymus, uterus, and others selectively irradiated. With certain exceptions, the weight factor of 0.05 is applied to the average dose in the remainder tissues and organs

^cThe remainder tissues are adrenals, extrathoracic tissues, gall bladder, heart wall, kidneys, lymphatic nodes, muscle, oral mucosa, pancreas, prostate, small intestine, spleen, thymus, and uterus/cervix. The weight factor for the remainder is applied to the average of the male and female remainder doses, each being the unweighted average dose to the 13 organs or tissues appropriate to the male or female

^dIn both the 1991 and 2007 formulations, the dose to the colon is the mass-weighted mean of upper and lower intestine doses

in which H_T is the *equivalent dose* in organ or tissue T , $D_{T,R}$ is the mean absorbed dose in organ or tissue T from radiation R , ω_R is a radiation weighting factor for radiation R as determined from ► [Table 8](#), and ω_T is a tissue weight factor given in ► [Table 9](#). Note that in this formulation, ω_R is independent of the organ or tissue and ω_T is independent of the radiation.

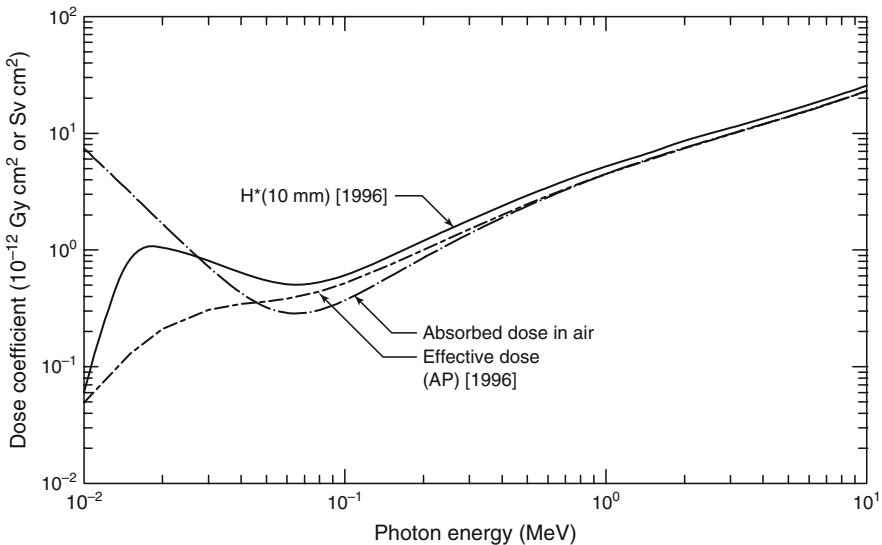
In computing the dose conversion coefficient for the effective dose, one assumes that the phantom is irradiated by unit fluence of monoenergetic particles of energy E . Neither local values nor tissue-average dose equivalents but only tissue-average absorbed doses are calculated. The tissue-average absorbed doses are multiplied by quality factors determined not by the LET distributions in the tissues and organs but by quality factors characteristic of the incident

radiation. This is a fundamental departure from the methodology used in determination of the conversion coefficients for the effective dose equivalent.

2.3.4 Comparison of Dose Conversion Coefficients

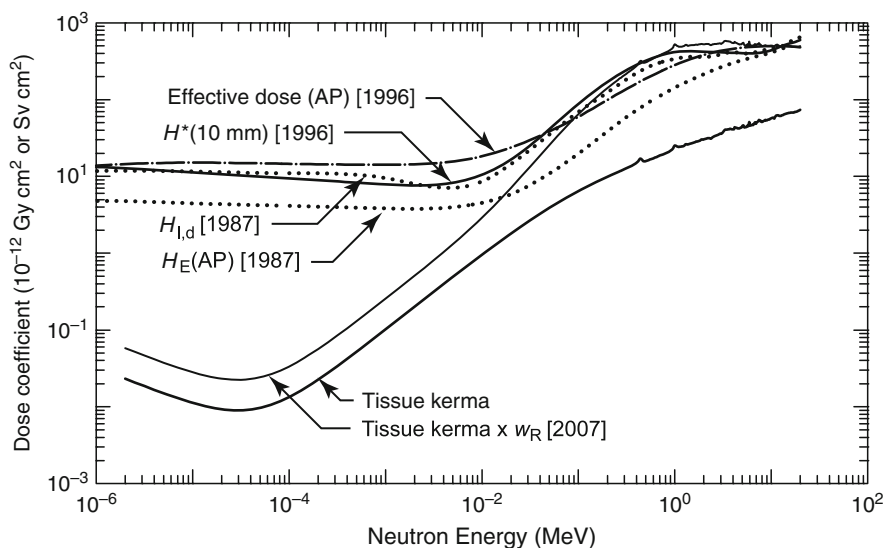
► *Figures 13* and ► *14* compare the dose conversion coefficients for photons and neutrons, respectively. At energies above about 0.1 MeV, the various photon coefficients are very nearly equal. This is a fortunate situation for radiation dosimetry and surveillance purposes. Instruments such as ion chambers respond essentially in proportion to absorbed dose in air. Personnel dosimeters are usually calibrated to give responses proportional to the ambient dose. Both the ambient dose and the absorbed dose in air closely approximate the effective dose equivalent. However, below 100 keV the three conversion coefficients are quite different. At the scale of the graph, the 1996 ambient dose coefficients are indistinguishable from the 1987 deep dose index.

The comparison of conversion coefficients for neutrons is not so straightforward. The tissue kerma always has the smallest value, largely because no quality factor is applied to the kinetic energy of a secondary charged particle. Fortunately, the ambient dose and the deep dose equivalent index have conversion coefficients that are very similar at energies above about 5 keV. Therefore, historic dosimetry records based on personnel dosimeters calibrated in terms of the deep dose equivalent index do not diverge significantly from those that would have been recorded using more modern dose standards. Furthermore, the ambient dose coefficient exceeds that for the effective dose equivalent index above about 0.01 MeV. Thus, calibration of personnel dosimeters in terms of ambient dose is a conservative practice. It should be noted that neutron dose conversion factors in the U.S. N.R.C. regulations (10CFR Part 20) are based on very early calculations (NCRP 1971).



■ Figure 13

Comparison of photon dose conversion coefficients. Data are from ICRP (1996)



■ Figure 14

Comparison of neutron dose conversion coefficients. Data are from ICRP (1987, 1996, 2007). The 1987 deep dose index and effective dose equivalent are based on quality factors defined prior to ICRP Report 45 (1985)

3 Basic Methods in Radiation Attenuation Calculations

In this section, simplified methods for estimating the dose under specialized source and geometric conditions are reviewed. The methods apply in circumstances in which there is a direct path from source to receiver and a significant portion of the dose is from uncollided radiation. A spatially distributed source is divided conceptually into a set of contiguous small sources, each of which can be treated as a point source. With an *uncollided point kernel*, the uncollided dose can be calculated for each point source. Summation or integration over the source volume then yields the total uncollided dose. In general, a correction factor may be applied to the uncollided point kernel to yield the point kernel for combined uncollided and collided radiation. For monoenergetic gamma rays, the correction factor is referred to as the *buildup factor*. For polyenergetic X-rays, an *attenuation factor* jointly accounts for both collided and uncollided radiation. Similarly, for polyenergetic neutron sources in hydrogenous media, the dose from collided and uncollided fast neutrons is estimated with a total-dose point kernel.

3.1 The Point-Kernel Concept

The fluence or dose at some point of interest is in many situations determined primarily by the uncollided radiation that has streamed directly from the source without any interaction in the surrounding medium. For example, if only air separates a gamma-ray or neutron source from a detector, interactions in the intervening air or in nearby solid objects, such as the ground or

building walls, are often negligible, and the radiation field at the detector is due almost entirely to uncollided radiation coming directly from the source. Scattered and other secondary radiation in such situations is of minor importance. In this section, some basic properties of the uncollided radiation field are presented, and methods for estimating the dose from this radiation are derived.

3.1.1 Exponential Attenuation

The *linear interaction coefficient* for indirectly ionizing radiations such as gamma rays or neutrons, $\mu(E)$, also called the *macroscopic cross section* $\Sigma(E)$, in the limit of small distances, is the probability per unit distance of travel that a particle of energy E experiences an interaction such as scattering or absorption. From this definition, it is easily shown that the probability of a particle traveling a distance x without interaction is given by


$$P(x) = e^{-\mu x}. \quad (33)$$

From this result, the *half-value thickness* x_2 that is required to reduce the uncollided radiation to one-half of its initial value can readily be found, namely, $x_2 = \ln 2/\mu$. Similarly, the *tenth-value thickness* x_{10} , which is the distance the uncollided radiation must travel to be reduced to 10% of its initial value, is found to be $x_{10} = \ln 10/\mu$. The concepts of half-value and tenth-value thicknesses, although stated here for uncollided radiation, are also often used to describe the attenuation of the total radiation dose. The average distance λ that a particle streams from the point of its birth to the point at which it makes its first interaction is called the *mean-free-path length*. It is easily shown that $\lambda = 1/\mu$.

3.1.2 Uncollided Dose from a Monoenergetic Point Source

In the following subsections, basic expressions are derived for the dose from uncollided radiation produced by isotropic point sources.

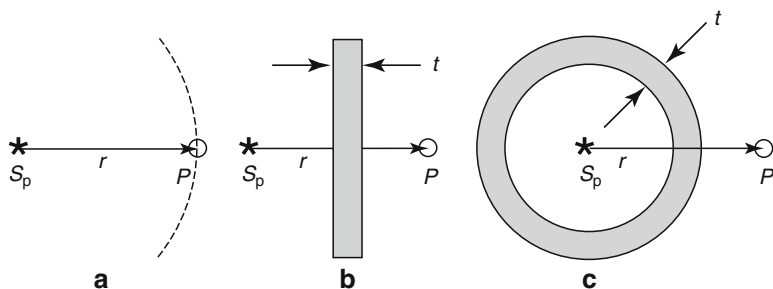
Point Source in a Vacuum

Consider a point-isotropic source that emits S_p particles into an infinite vacuum as in  [Fig. 15a](#). All particles move radially outward without interaction, and because of the source isotropy, each unit area on an imaginary spherical shell of radius r has the same number of particles crossing it, namely, $S_p/(4\pi r^2)$. It then follows from the definition of the fluence that the fluence Φ^o of uncollided particles at a distance r from the source is

$$\Phi^o(r) = \frac{S_p}{4\pi r^2}. \quad (34)$$

If all the source particles have the same energy E , the response of a point detector at a distance r from the source is obtained by multiplying the uncollided fluence by the appropriate dose-conversion coefficient \mathcal{R} , which usually depends on the particle energy E , namely,

$$D^o(r) = \frac{S_p \mathcal{R}(E)}{4\pi r^2}. \quad (35)$$



■ Figure 15

Point isotropic source (a) in a vacuum, (b) with a slab shield, and (c) with a spherical-shell shield. Point P is the location of the receiver or point detector

Notice that the dose and fluence decrease as $1/r^2$ as the distance from the source is increased. This decreasing dose with increasing distance is sometimes referred to as *geometric attenuation*.

Point Source in a Homogenous Attenuating Medium

Now consider the same point monoenergetic isotropic source embedded in an infinite homogenous medium characterized by a total interaction coefficient μ . As the source particles stream radially outward, some interact before they reach the imaginary sphere of radius r and do not contribute to the uncollided fluence. The number of source particles that travel at least a distance r without interaction is $S_p e^{-\mu r}$, so that the uncollided dose is

$$D^o(r) = \frac{S_p \mathcal{R}(E)}{4\pi r^2} e^{-\mu(E)r}. \quad (36)$$

The term $e^{-\mu r}$ is referred to as the *material attenuation* term to distinguish it from the $1/r^2$ geometric attenuation term.

Point Source with a Shield

Now suppose that the only attenuating material separating the source and the detector is a slab of material with attenuation coefficient μ and thickness t as shown in ► Fig. 15b. In this case, the probability that a source particle reaches the detector without interaction is $e^{-\mu t}$, so that the uncollided dose is

$$D^o(r) = \frac{S_p \mathcal{R}(E)}{4\pi r^2} e^{-\mu(E)t}. \quad (37)$$

This same result holds if the attenuating medium has any shape (e.g., a spherical shell of thickness t as shown in ► Fig. 15c) provided that a ray drawn from the source to the detector passes through a thickness t of the attenuating material.

If the interposing shield is composed of a series of different materials such that an uncollided particle must penetrate a series of thicknesses t_i of materials with attenuation coefficients μ_i before reaching the detector, the uncollided dose is

$$D^o(r) = \frac{S_p \mathcal{R}(E)}{4\pi r^2} \exp(-\sum_i \mu_i(E) t_i). \quad (38)$$

Here $\sum_i \mu_i t_i$ is the total number of mean-free-path lengths of attenuating material that an uncollided particle must traverse without interaction, and $\exp(-\sum_i \mu_i t_i)$ is the probability that a source particle traverses this number of mean-free-path lengths without interaction.

3.2 Uncollided Doses for Distributed Sources

3.2.1 The Superposition Procedure


The results for the uncollided dose from a point source can be used to derive expressions for the uncollided dose arising from a wide variety of distributed sources such as line sources, area sources, and volumetric sources. One widely used approach is to divide the distributed source conceptually into a set of equivalent point sources and then to sum (integrate) the dose contribution from each point source.


The examples presented later for a line source are selected because of their simplicity or utility. In all these examples, it is assumed that the source is monoenergetic and isotropic and the detector is a point isotropic one. For polyenergetic sources, the monoenergetic result can be summed (or integrated) over all source energies.

The superposition technique of decomposing a source into a set of simpler sources is very powerful and has been applied to line, surface, and volumetric sources of complex shapes. Many important practical cases have been examined and generalized results have been published. Among the special cases are cylindrical and spherical surface and volume sources, with and without external shields, and with interior as well as exterior receptor locations. The examples below are but a few of the known results. For other source and shield configurations, the reader is referred to the publications of Rockwell (1956), Blizard and Abbott (1962), Hungerford (1966), Blizard et al. (1968), Schaeffer (1973), Courtney (1975), Chilton et al. (1984), and Shultis and Faw (2000).

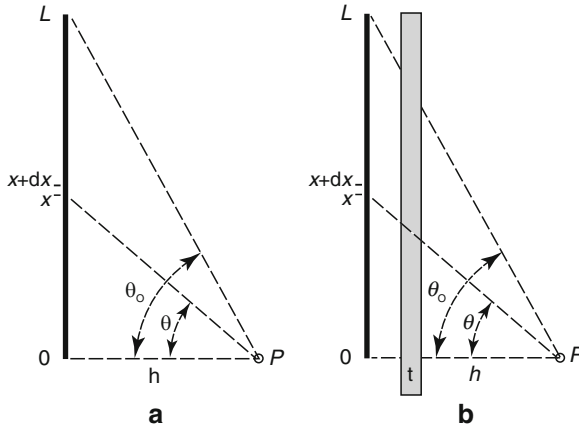
3.2.2 Example Calculations for Distributed Sources

The Line Source

A straight-line source of length L emitting isotropically S_1 particles per unit length at energy E is depicted in  Fig. 16. A detector is positioned at point P , a distance h from the source along a perpendicular to one end of the line. Consider a segment of the line source between distance x and $x + dx$ measured from the bottom of the source. The source within this segment may be treated as an effective point isotropic source emitting $S_1 dx$ particles which produces an uncollided dose at P of dD^o . To obtain the total dose at P from all segments of the line source, one then must sum, or rather integrate, dD^o over all line segments. Several cases are discussed as follows.

Line Source in a Nonattenuating Medium. In the absence of material interaction () Fig. 16a), the differential uncollided dose produced by particles emitted in dx about x is, from (36),

$$dD^o(P) = \frac{1}{4\pi} \frac{S_1 \mathcal{R} dx}{x^2 + h^2} \quad (39)$$



■ **Figure 16**
Isotropic line source (a) in a homogenous medium and (b) with a slab shield

and thus,

$$D^o(P) = \frac{S_l \mathcal{R}}{4\pi} \int_0^L \frac{dx}{x^2 + h^2} = \frac{S_l \mathcal{R} \theta_0}{4\pi h}. \quad (40)$$

The angle $\theta_0 = \tan^{-1} L/h$ in this result must be expressed in radians.

Line Source in a Homogenous Attenuating Medium. Now suppose that the source and receptor are present in a homogenous medium with a total interaction coefficient μ . Attenuation along the ray from x to P reduces the uncollided dose at P to

$$dD^o(P) = \frac{1}{4\pi} \frac{S_l \mathcal{R} dx}{x^2 + h^2} \exp[-\mu \sqrt{x^2 + h^2}], \quad (41)$$

where \mathcal{R} and μ generally depend on the particle energy E . The total uncollided dose now is described by the integral

$$D^o(P) = \frac{S_l \mathcal{R}}{4\pi h} \int_0^{\theta_0} d\theta e^{-\mu h \sec \theta}. \quad (42)$$

This integral cannot be evaluated analytically. However, it can be expressed in terms of the *Sievert integral* or the *secant integral*, defined as

$$F(\theta, b) \equiv \int_0^\theta dx e^{-b \sec x}. \quad (43)$$

This integral is widely available in the previously cited text and reference works. With it, the dose from a line source may be expressed as

$$D^o(P) = \frac{S_l \mathcal{R}}{4\pi h} F(\theta_0, \mu h). \quad (44)$$

Line Source Behind a Slab Shield. Now suppose that the only material separating the line source and the receptor is a parallel slab or concentric cylindrical-shell shield of thickness t and total attenuation coefficient μ_s , as shown in \blacktriangleright Fig. 16b. For this case, the analysis above using only attenuation in the slab yields

$$D^o(P) = \frac{S_L \mathcal{R}}{4\pi h} F(\theta_o, \mu_s t). \quad (45)$$

If the shield is made up of layers of thicknesses t_i and attenuation coefficients μ_{si} , then $\mu_s t$ must be replaced by $\sum_i \mu_{si} t_i$, the total mean-free-path thickness of the shield.

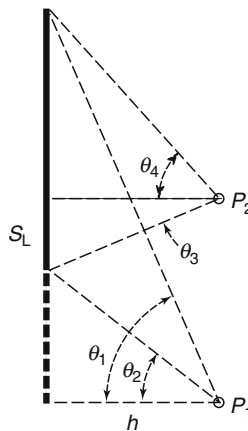
A Superposition Procedure for Line Sources. The restriction in the foregoing examples that the detector be perpendicularly opposite one end of the line source is easily relaxed by use of the principle of *superposition of sources*. \blacktriangleright Figure 17 illustrates two receptor points in relation to a line source in a homogenous attenuating medium. Determination of the uncollided dose at either point may be obtained by conceptually decomposing the line source into two adjacent line sources each of which has an end perpendicular to the detector. Point P_1 , for example, is on a normal from the end of a projection of the line source. Were the line source truly of the extended length, then the dose would be given by (44) with angle argument θ_1 . However, that result would be too high by just the amount contributed by a line source of the same strength subtending angle θ_2 . Thus, at point P_1 ,

$$D^o(P_1) = \frac{S_L \mathcal{R}}{4\pi h} [F(\theta_1, \mu h) - F(\theta_2, \mu h)]. \quad (46)$$

By similar reasoning, at point P_2 ,

$$D^o(P_2) = \frac{S_L \mathcal{R}}{4\pi h} [F(\theta_3, \mu h) + F(\theta_4, \mu h)]. \quad (47)$$

As illustrated by these line source examples, the superposition of multiple distributed sources, for each of which the dose is readily calculated, to create a more complex source configuration is an extremely useful procedure that can be used effectively for all types of sources.



\blacksquare Figure 17

Application of the superposition principle to an isotropic line source

Indeed, part of the art of shield analysis is to devise how to reduce a complex source problem to a set of simpler problems, and the source superposition principle is a valuable tool in this reduction.

4 Photon Attenuation Calculations

This section describes the engineering methodology that has evolved for the design and analysis of shielding for gamma and X-rays with energies from about 1 keV to about 20 MeV. To support this methodology, very precise radiation transport calculations have been applied to a wide range of carefully prescribed situations. The results are in the form of buildup factors, attenuation factors, albedos or reflection factors, and line-beam response functions.

Buildup factors relate the total dose to the dose from uncollided photons alone and are most applicable to point monoenergetic-radiation sources with shielding well distributed between the source point and points of interest. Attenuation factors apply equally well to monoenergetic sources and to polyenergetic sources such as X-ray machines and are most applicable when a shield wall separates the source and points of interest, the wall being sufficiently far from the source that radiation strikes it as a nearly parallel beam. There are many common features of buildup and attenuation factors and it is possible to represent one factor in terms of the other. Albedos, which describes how radiation is reflected from a surface, and line-beam response functions, which are used in skyshine analyses, are taken up in other sections of this chapter.

Discussed first in this section are buildup factors for point isotropic and monoenergetic sources in infinite media. Incorporation of these buildup factors into the uncollided point kernel is treated next. Then addressed are three topics associated with the use of buildup factors. The first is the use of empirical buildup-factor approximations designed to simplify engineering design and analysis. The second is the use of buildup factors with point kernels to treat spatially distributed radiation sources. The third is the application of approximate methods to permit the use of buildup factors in media with variations in composition.

4.1 The Photon Buildup-Factor Concept

Whatever the photon source and the attenuating medium, the energy spectrum of the total photon fluence $\Phi(\mathbf{r}, E)$ at some point of interest \mathbf{r} may be divided into two components. The *unscattered* component $\Phi^o(\mathbf{r}, E)$ consists of just those photons that have reached \mathbf{r} from the source without having experienced any interactions in the attenuating medium. The *scattered* component $\Phi^s(\mathbf{r}, E)$ consists of source photons scattered one or more times, as well as secondary photons such as X-rays and annihilation gamma rays. Accordingly, the dose or detector response $D(\mathbf{r})$ at point of interest \mathbf{r} may be divided into unscattered (primary) and scattered (secondary) components $D^o(\mathbf{r})$ and $D^s(\mathbf{r})$. The buildup factor $B(\mathbf{r})$ is defined as the ratio of the total dose to the unscattered dose, i.e.,

$$B(\mathbf{r}) \equiv \frac{D(\mathbf{r})}{D^o(\mathbf{r})} = 1 + \frac{D^s(\mathbf{r})}{D^o(\mathbf{r})}. \quad (48)$$

The doses may be evaluated using response functions described in [Sect. 2](#), so that

$$B(\mathbf{r}) = 1 + \frac{\int dE \mathcal{R}(E) \Phi^s(\mathbf{r}, E)}{\int dE \mathcal{R}(E) \Phi^o(\mathbf{r}, E)}, \quad (49)$$

in which the integrations are over all possible E .

It is very important to recognize that in (49), the fluence terms depend only on the source and medium, and not on the type of dose or response. The conversion factors or response function $\mathcal{R}(E)$ depends only on the type of dose, and not on the attenuating medium. For these reasons, it is imperative to associate with buildup factors the nature of the source, the nature of the attenuating medium, and the nature of the response.

When the source is monoenergetic, with energy E_o , then $\Phi^o(\mathbf{r}, E) = \Phi^o(\mathbf{r})\delta(E - E_o)$, so that

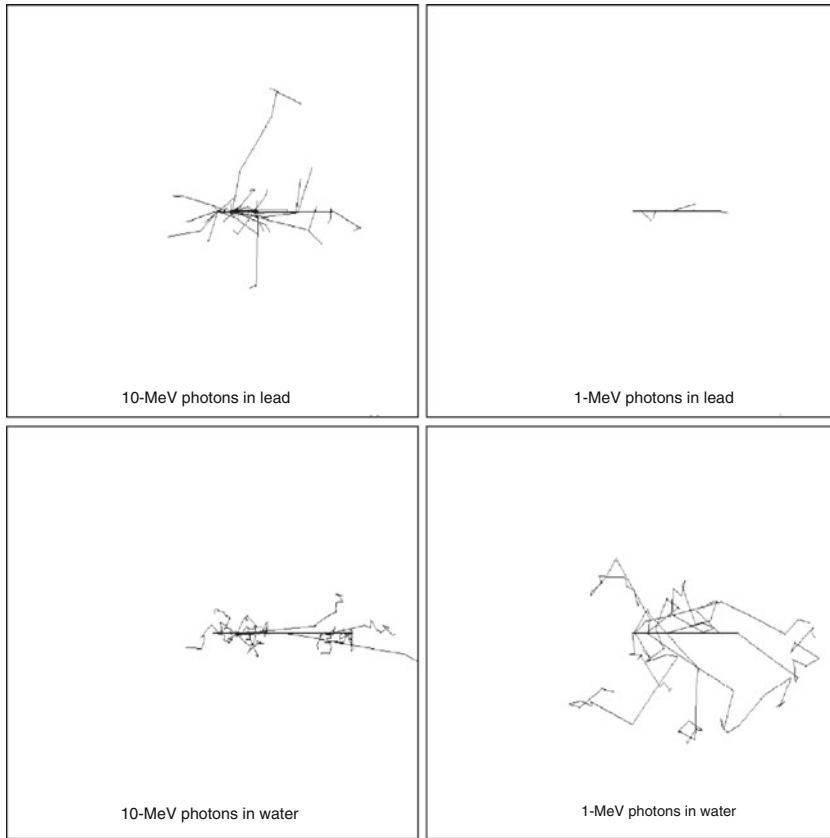
$$B(\mathbf{r}) = 1 + \frac{1}{\Phi^o(\mathbf{r})} \int_0^{E_o} dE \frac{\mathcal{R}(E)}{\mathcal{R}(E_o)} \Phi_s(\mathbf{r}, E). \quad (50)$$

In this case, the response nature is fully accounted for in the ratio $\mathcal{R}(E)/\mathcal{R}(E_o)$.

4.2 Isotropic, Monoenergetic Sources in Infinite Media

By far, the largest body of buildup-factor data is for point, isotropic, and monoenergetic sources of photons in infinite homogenous media. The earliest data (Fano et al. 1959; Goldstein 1959; Goldstein and Wilkins 1954) were based on moments-method calculations (Shultis and Faw 2000) and accounted only for buildup of Compton-scattered photons. Subsequent moments-method calculations (Eisenhauer and Simmons 1975; Chilton et al. 1980) accounted for buildup of annihilation photons as well. Buildup-factor calculations using the discrete-ordinates ASFIT code (Subbaiah et al. 1982) and the integral-transport PALLAS code (Takeuchi, Tanaka, and Kinno 1981) account for not only Compton-scattered and annihilation photons, but also for fluorescence and bremsstrahlung. These calculations, which supplement later moments-method calculations, are the basis for the data prescribed in the American National Standard for buildup factors (ANSI/ANS 1991). Calculation of buildup factors for high-energy photons requires consideration of the paths traveled by positrons from their creation until their annihilation. Such calculations have been performed by Hirayama (1987) and by Faw and Shultis (1993a) for photon energies as great as 100 MeV. Most point-source buildup-factor compilations exclude coherently scattered photons and treat Compton scattering in the free-electron approximation. This is also true for the buildup factors in the standard. Thus, in computing the dose or response from unscattered photons, coherent scattering should be excluded and the total Klein–Nishina cross section should be used. Correction for coherent scattering, significant for only low-energy photons at deep penetration, is discussed in ANSI/ANS (1991).

Figure 18 gives a qualitative impression of the buildup of secondary photons during the attenuation of primary photons. For 10-MeV photons in lead, there is considerable buildup of annihilation photons, which are emitted isotropically, and bremsstrahlung, which deviates little in direction from the path of the decelerating electron or positron. For 1-MeV photons in lead, there is very little buildup of secondary photons, owing to the strong photoelectric absorption of the primary photons. In water, both 1- and 10-MeV photons experience Compton scattering principally. However, for the higher-energy primary photons, the scattering leads to relatively small change in direction. Figure 19 illustrates the energy spectrum of the energy fluence

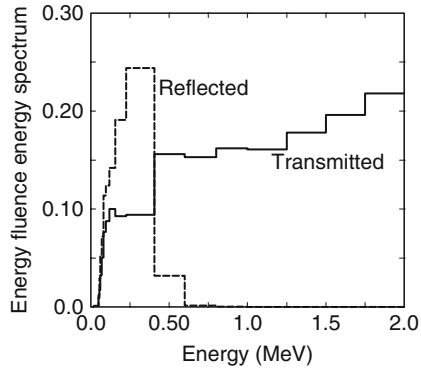


■ Figure 18

Comparison of photon transport in lead and water. Each box has 10 mean-free paths on a side. Each depicts the projection in a plane of primary and secondary photon tracks arising from 10 primary photons originating at the box center, moving to the right in the plane of the paper. Tracks computed using the EGS4 code, courtesy of Robert Stewart, Kansas State University

$E\Phi(E)$ of reflected and transmitted photons produced by 2-MeV primary photons, normally incident on a concrete slab two mean free paths in thickness. These fluences are normalized to unit incident flow and, thus, are dimensionless. Note that transmitted photons have energies up to the energy of the primary photons. However, the reflected photons, mostly single scattered, are much more restricted in energy.

Tables of buildup factors are available in standards (ANSI/ANS 1991), the technical literature (Eisenhauer and Simmons 1975; Takeuchi and Tanaka 1984; Goldstein and Wilkins 1954) and many textbooks. Buildup-factor data are generally more broadly applicable than might be thought at first glance. As indicated in (50), it is the ratio $\mathcal{R}(E)/\mathcal{R}(E_o)$ that defines the dependence of the buildup factor on the type of dose or response. For responses such as kerma or absorbed dose in air or water, exposure, or dose equivalent, the ratio is not very sensitive to the type of response. Thus, buildup factors for air kerma may be used with little error for exposure or dose equivalent.



■ Figure 19

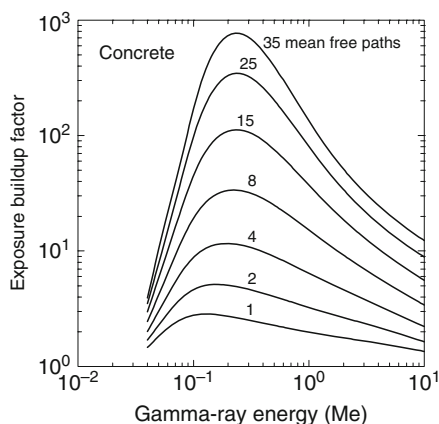
Transmitted and reflected energy fluences for 2-MeV photons normally incident on a concrete slab of two mean free path thickness

It can be shown that, for a point isotropic source of monoenergetic photons in an infinite homogenous medium, the buildup factor depends spatially only on the number of mean free paths μr separating the source and the point of interest. Here, μ is the total interaction coefficient (excluding coherent scattering) in the attenuating medium at the source energy, namely $\mu(E_0)$. Thus, we write the buildup factor as $B(\mu r)$, but it must be recognized that there is an implicit dependence on the source energy, the nature of the attenuating medium, and the nature of the response.

► Figure 20 illustrates the buildup factor for concrete, plotted with the photon energy as the independent variable and the number of mean free paths as a parameter. That there are maxima in the curves is due to the relative importance of the photoelectric effect, as compared to Compton scattering, in the attenuation of lower-energy photons and to the very low fluorescence yields exhibited by the low- Z constituents of concrete. ► Figure 21 illustrates the buildup factor for lead, plotted with the number of mean free paths as the independent variable and the photon energy as a parameter. For high-energy photons, pair production is the dominant attenuation mechanism in lead, the cross section exceeding that for Compton scattering at energies above about 5 MeV. The buildup is relatively large because of the production of 0.511-MeV annihilation gamma rays. As may also be seen from the figure, the attenuation factor increases greatly at photon energies just above the 0.088-MeV K -edge for photoelectric absorption, each absorption resulting in a cascade of X-rays. For these reasons, buildup factors may be extraordinarily large, as evidenced by the line for 0.089-MeV photons in ► Fig. 21. At energies below the K -edge, the buildup factors are very small. The importance of fluorescence in the buildup of low-energy photons is addressed by Tanaka and Takeuchi (1986) and by Subbaiah and Natarajan (1987).

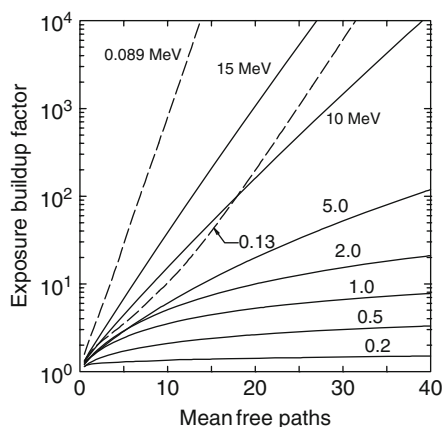
4.3 Buildup Factors for Point and Plane Sources

Many so-called “point-kernel codes” finding wide use in radiation shielding design and analysis make exclusive use of buildup factors for point isotropic sources in infinite media. This is true even when the source and shield configuration is quite different from that of an infinite



■ Figure 20

Air-kerma buildup factors for gamma-ray attenuation in concrete, excluding bremsstrahlung, fluorescence, and coherent scattering. Data from Eisenhauer and Simmons (1975)



■ Figure 21

Exposure buildup factors for gamma-ray attenuation in lead, calculated using the PALLAS code, excluding coherent scattering. Data from ANSI/ANS (1991)

medium. A good example is that of a point source and point receptor, each at some distance in air from an intervening shielding wall. Is the use of infinite-medium buildup factors a conservative approximation? That question is addressed in ► [Table 10](#), prepared for shielding of 1-MeV gamma rays by iron. This table lists exposure buildup factors, in some cases for infinite media and in other cases for vacuum-bounded finite media. The first column in the table is the number of mean free paths from source to receptor location. Six columns of buildup factors follow, three for point isotropic (PTI) sources and three for plane monodirectional (PLM) sources.

The PTI source in an infinite medium is the reference case. Data for the PTI source in a finite medium refer to the exposure rate at the surface of a sphere whose radius corresponds to

■ **Table 10**
Exposure buildup factors for 1-MeV gamma rays in iron

Thickness (mfp)	Source type and attenuating medium					
	PTI			PLM		
	Infinite ^a	Finite ^b	Slab ^c	Infinite ^d	Semi-infinite ^e	Finite ^f
0.5	1.41	1.36	1.35		1.49	
1	1.85	1.77	1.73	1.92	1.88	1.72
2	2.85	2.68	2.63	2.74	2.68	2.45
3	4.00	3.75	3.65		3.54	
4	5.30	4.95	4.43	4.57	4.46	3.97
5	6.74	6.26	6.47		5.44	
6	8.31	7.70	6.67		6.51	5.77
7	10.0	9.41	8.98	8.81	7.63	
8	11.8	11.1			8.82	7.91
10	15.8	14.5		11.6	11.3	9.77
15	27.5	26.1		18.9	18.5	

^aStandard ANSI/ANS-6.4.3-1991;

^bEGS4 calculations, courtesy Sherrill Shue, Kansas State University;

^cDunn et al. (1992);

^dGoldstein (1959);

^eTakeuchi and Tanaka (1984);

^fChen and Faw (1994)

the mean free path thickness. Data for the PTI source and slab shield are for a point source on one side of a slab of given thickness and a receptor point directly on the opposite side of the slab. Data for the PLM source in an infinite medium are for the buildup factor as a function of distance from a hypothetical plane source emitting a parallel beam of photons perpendicular to the plane. Data for the PLM source in a semi-infinite medium are for the buildup factor as a function of depth in a half-space illuminated by a normally incident parallel beam of photons. Data in the last column, for the PLM source in a finite medium, refer to the exposure on one side of a slab shield of given thickness which is illuminated by a parallel beam of photons normally incident on the opposite side of the slab.

It is apparent from [Table 10](#) that for the cases examined, use of buildup factors for point sources in an infinite medium, with few exceptions, is a conservative approximation in shield design, that is, predicted doses are slightly higher than the actual doses. However, the PLM examples are all for beams *normally* incident on slab shields. When beams are obliquely incident on slab shields, point kernel codes routinely determine the number of mean free paths along the oblique path through the slab shield and apply infinite-medium buildup factors for the corresponding thickness. This practice can underestimate shielding requirements because buildup factors for slant penetration of beams can greatly exceed those for point sources computed at the same optical thicknesses (mean free paths) as is addressed later in this section.

Buildup factors are available for plane isotropic (PLI) and plane monodirectional (PLM) gamma-ray sources in infinite media. Indeed, Fano et al. (1959), Goldstein (1959), and Spencer

(1962), in their moments-method calculations, obtained buildup factors for plane sources first and, from these, buildup factors for point sources. Buildup factors at depth in a half-space shield are also available for the PLM source, that is, normally incident photons (Takeuchi et al. 1981; Takeuchi and Tanaka 1984; Hirayama 1987).

Special methods have been developed for treating buildup when source and receptor are separated by many shielding slabs, such as walls and floors of a structure, at various orientations. For example, Dunn et al. (1992) address shipboard radiation shielding problems and provide buildup factors for common shielding materials.

4.3.1 Empirical Approximations for Buildup Factors

A great deal of effort has been directed toward the approximation of point-source buildup factors by mathematical functions which can be used directly in calculations. These efforts have dealt almost exclusively with buildup factors for point-isotropic and monoenergetic sources in infinite media. Two forms of approximation have been in use for many years. One is the *Taylor form* (Chilton 1977; Foderaro and Hall 1981; Shure and Wallace 1988). The other is the *Berger form* (Chilton 1979; Chilton et al. 1980). While both forms still see a wide application in computer codes used in engineering practice, a more modern, more accurate, but much more complicated approximation is the *geometric progression* (GP) form, and without question it is the preferred approximation to use if possible.

The Geometric Progression Approximation

An extraordinarily precise formulation, called the *geometric progression approximation* of the buildup factor, was developed in recent years (Harima 1986; Harima et al. 1986, 1991). The approximation is in the form

$$B(E_o, \mu r) \simeq \begin{cases} 1 + (b - 1)(K^{\mu r} - 1)/(K - 1), & K \neq 1 \\ 1 + (b - 1)\mu r, & K = 1, \end{cases} \quad (51)$$

where

$$K(\mu r) = c(\mu r)^a + d \frac{\tanh(\mu r/\xi - 2) - \tanh(-2)}{1 - \tanh(-2)}, \quad (52)$$

in which a , b , c , d , and ξ are parameters dependent on the gamma-ray energy, the attenuating medium, and the nature of the response. Example values of the parameters for kerma in air as the response, and for attenuation in air, water, concrete, iron, and lead are listed in [► Tables 11 and 12](#). The parameters are based on PALLAS code calculations (Takeuchi et al. 1981).

4.3.2 Point-Kernel Applications of Buildup Factors

For a distributed source of monoenergetic photons $S_\nu(\mathbf{r}_s)$ of energy E_o , the dose from uncollided photons at some position \mathbf{r} is

$$D^o(\mathbf{r}) = \int_{V_s} dV_s \frac{S_\nu(\mathbf{r}_s) \mathcal{R}(E_o)}{4\pi|\mathbf{r}_s - \mathbf{r}|^2} e^{-\ell}, \quad (53)$$

■ Table 11

Coefficients for the geometric progression form of the gamma-ray buildup factor

Photon energy (MeV)	Air kerma / air medium					Air kerma / concrete medium				
	<i>b</i>	<i>c</i>	<i>a</i>	ξ	<i>d</i>	<i>b</i>	<i>c</i>	<i>a</i>	ξ	<i>d</i>
0.015	1.170	0.459	0.175	13.73	-0.0862	1.029	0.364	0.240	14.12	-0.1704
0.020	1.407	0.512	0.161	14.40	-0.0819	1.067	0.389	0.214	12.68	-0.1126
0.030	2.292	0.693	0.102	13.34	-0.0484	1.212	0.421	0.201	14.12	-0.1079
0.040	3.390	1.052	-0.004	19.76	-0.0068	1.455	0.493	0.171	14.53	-0.0925
0.050	4.322	1.383	-0.071	13.51	0.0270	1.737	0.628	0.115	15.82	-0.0600
0.060	4.837	1.653	-0.115	13.66	0.0511	2.125	0.664	0.118	11.90	-0.0615
0.080	4.929	1.983	-0.159	13.74	0.0730	2.557	0.895	0.042	14.37	-0.0413
0.100	4.580	2.146	-0.178	12.83	0.0759	2.766	1.069	0.001	12.64	-0.0251
0.150	3.894	2.148	-0.173	14.46	0.0698	2.824	1.315	-0.049	8.66	-0.0048
0.200	3.345	2.147	-0.176	14.08	0.0719	2.716	1.430	-0.070	18.52	0.0108
0.300	2.887	1.990	-0.160	14.13	0.0633	2.522	1.492	-0.082	16.59	0.0161
0.400	2.635	1.860	-0.146	14.24	0.0583	2.372	1.494	-0.085	15.96	0.0194
0.500	2.496	1.736	-0.130	14.32	0.0505	2.271	1.466	-0.082	16.25	0.0195
0.600	2.371	1.656	-0.120	14.27	0.0472	2.192	1.434	-0.078	17.02	0.0199
0.800	2.207	1.532	-0.103	14.12	0.0425	2.066	1.386	-0.073	15.07	0.0202
1.000	2.102	1.428	-0.086	14.35	0.0344	1.982	1.332	-0.065	15.38	0.0193
1.500	1.939	1.265	-0.057	14.24	0.0232	1.848	1.227	-0.047	16.41	0.0160
2.000	1.835	1.173	-0.039	14.07	0.0161	1.775	1.154	-0.033	14.35	0.0100
3.000	1.712	1.051	-0.011	13.67	0.0024	1.671	1.054	-0.010	10.47	-0.0008
4.000	1.627	0.983	0.006	13.51	-0.0051	1.597	0.988	0.008	12.53	-0.0115
5.000	1.558	0.943	0.017	13.82	-0.0117	1.527	0.951	0.020	9.99	-0.0184
6.000	1.505	0.915	0.025	16.37	-0.0231	1.478	0.940	0.021	13.11	-0.0163
8.000	1.418	0.891	0.032	12.06	-0.0167	1.395	0.917	0.028	13.45	-0.0213
10.00	1.358	0.875	0.037	14.01	-0.0226	1.334	0.901	0.035	12.56	-0.0267
15.00	1.267	0.844	0.048	14.55	-0.0344	1.260	0.823	0.065	14.28	-0.0581

Source: Extracted from American National Standard ANSI/ANS-6.4.3-1991, *Gamma-Ray Attenuation Coefficients and Buildup Factors for Engineering Materials*, published by the American Nuclear Society. Data are also available from Data Library DLC-129/ANS643, issued by the Radiation Shielding Information Center, Oak Ridge National Laboratory, Oak Ridge, TN

■ Table 12

Coefficients for the geometric progression form of the gamma-ray buildup factor

Photon energy (MeV)	Air kerma / iron medium					Air kerma / lead medium				
	<i>b</i>	<i>c</i>	<i>a</i>	ξ	<i>d</i>	<i>b</i>	<i>c</i>	<i>a</i>	ξ	<i>d</i>
0.015	1.004	1.561	-0.554	5.60	0.3524					
0.020	1.012	0.130	0.620	11.39	-0.6162					
0.030	1.028	0.374	0.190	29.34	-0.3170	1.007	0.322	0.246	13.67	-0.1030
0.040	1.058	0.336	0.248	11.65	-0.1188	1.014	0.317	0.245	14.95	-0.0867
0.050	1.099	0.366	0.232	14.01	-0.1354	1.023	0.312	0.252	14.17	-0.1005
0.060	1.148	0.405	0.208	14.17	-0.1142	1.033	0.320	0.260	13.89	-0.1223
0.080	1.267	0.470	0.180	14.48	-0.0974	1.058	0.362	0.233	13.91	-0.1127
0.088						1.067	0.382	0.220	14.14	-0.1048
0.089						2.368	1.580	0.075	12.44	-0.0635
0.090						2.187	1.693	0.050	18.21	-0.0415
0.100	1.389	0.557	0.144	14.11	-0.0791	1.930	1.499	0.061	29.65	-0.1162
0.110						1.821	1.196	0.102	16.64	-0.0756
0.120						1.644	0.970	0.136	16.10	-0.1135
0.130						1.540	0.718	0.194	15.69	-0.1685
0.140						1.472	0.479	0.273	16.50	-0.2153
0.150	1.660	0.743	0.079	14.12	-0.0476	1.402	0.352	0.269	17.09	-0.0247
0.160						1.334	0.329	0.145	11.38	-0.0643
0.200	1.839	0.911	0.034	13.23	-0.0334	1.201	0.158	0.426	14.12	-0.1873
0.300	1.973	1.095	-0.009	11.86	-0.0183	1.148	0.422	0.203	13.49	-0.1013
0.400	1.992	1.187	-0.027	10.72	-0.0140	1.187	0.562	0.137	14.19	-0.0706
0.500	1.967	1.240	-0.039	8.34	-0.0074	1.233	0.634	0.109	14.20	-0.0556
0.600	1.947	1.247	-0.040	8.20	-0.0096	1.269	0.685	0.089	13.78	-0.0440
0.800	1.906	1.233	-0.038	7.93	-0.0110	1.329	0.759	0.065	13.69	-0.0317
1.000	1.841	1.250	-0.048	19.49	0.0140	1.367	0.811	0.051	13.67	-0.0283
1.500	1.750	1.197	-0.040	15.90	0.0110	1.369	0.942	0.020	14.65	-0.0207
2.000	1.712	1.123	-0.021	7.97	-0.0057	1.384	0.980	0.014	13.51	-0.0216
3.000	1.627	1.059	-0.005	11.99	-0.0132	1.367	1.006	0.017	13.33	-0.0377
4.000	1.553	1.026	0.005	12.93	-0.0191	1.337	1.009	0.024	14.15	-0.0455
5.000	1.483	1.009	0.012	13.12	-0.0258	1.360	0.957	0.049	14.04	-0.0683

Table 12 (continued)

Photon energy (MeV)	Air kerma / iron medium					Air kerma / lead medium				
	<i>b</i>	<i>c</i>	<i>a</i>	ξ	<i>d</i>	<i>b</i>	<i>c</i>	<i>a</i>	ξ	<i>d</i>
6.000	1.442	0.980	0.023	13.37	-0.0355	1.363	0.965	0.054	14.21	-0.0715
8.000	1.354	0.974	0.029	13.65	-0.0424	1.441	0.994	0.061	14.18	-0.0800
10.000	1.297	0.949	0.042	13.97	-0.0561	1.464	1.148	0.032	14.08	-0.0554
15.000	1.199	0.957	0.049	14.37	-0.0594	1.573	1.337	0.016	13.54	-0.0463

Source: Extracted from American National Standard ANSI/ANS-6.4.3-1991, *Gamma-Ray Attenuation Coefficients and Buildup Factors for Engineering Materials*, published by the American Nuclear Society. Data are also available from Data Library DLC-129/ANS643, issued by the Radiation Shielding Information Center, Oak Ridge National Laboratory, Oak Ridge, TN

where the integration is over all source locations and ℓ is the optical thickness between \mathbf{r}_s and \mathbf{r} , namely,

$$\ell = \int_0^{|\mathbf{r}_s - \mathbf{r}|} ds \mu(s), \quad (54)$$

with s measured along a straight line from \mathbf{r}_s to \mathbf{r} . To correct for the buildup of secondary radiation, an appropriate buildup factor is included in the integrand of (53). If an infinite-medium, point-source buildup factor is used and the medium is of uniform composition but possibly of variable density, the total dose at \mathbf{r} is

$$D(\mathbf{r}) = \int_{V_s} dV_s \frac{S_v(\mathbf{r}_s) \mathcal{R}(E_o)}{4\pi|\mathbf{r}_s - \mathbf{r}|^2} B(E_o, \ell) e^{-\ell} \equiv \int_{V_s} dV_s S_v(\mathbf{r}_s) \mathcal{G}(\mathbf{r}_s, \mathbf{r}). \quad (55)$$

Here,

$$\mathcal{G}(\mathbf{r}_s, \mathbf{r}) \equiv \frac{\mathcal{R}(E_o)}{4\pi|\mathbf{r}_s - \mathbf{r}|^2} B(E_o, \ell) e^{-\ell} \quad (56)$$

is the dose Green's function or point kernel that gives the dose at \mathbf{r} due to a photon emitted isotropically at \mathbf{r}_s .

From this approximate result, it is seen that the total dose at \mathbf{r} from radiation emitted isotropically from \mathbf{r}_s depends only on the material properties along a line between \mathbf{r}_s and \mathbf{r} and on the distance $|\mathbf{r}_s - \mathbf{r}|$ between these two points. This approximation, based on the infinite-medium, point-source buildup factor, is sometimes called *ray theory*, indicative that the total dose is determined simply by the material and distance along the ray joining the source and detector points. In many situations, it is an excellent approximation and is widely used in photon shielding calculations. To illustrate the use of ray theory, two examples are given as follows.

Line Source in an Infinite Attenuating Medium

With reference to Fig. 16 and (41), one sees that the total dose at detector point P due to photons arising from the differential source length dx is

$$dD(P) = \frac{\mathcal{R}(E_o) S_1 dx}{4\pi(x^2 + h^2)} e^{-\mu\sqrt{x^2 + h^2}} B(E_o, \mu\sqrt{x^2 + h^2}). \quad (57)$$

In analogy to (41), the response due to the entire line source is given by the integral

$$D(P) = \mathcal{R}(E_o) \frac{S_l}{4\pi h} \int_0^{\theta_o} d\theta e^{-\mu h \sec \theta} B(E_o, \mu h \sec \theta). \quad (58)$$

In general, the integral must be evaluated numerically. However, if the Taylor form of buildup-factor approximation is employed, the integral yields a sum of Sievert integrals (Shultis and Faw 2000).

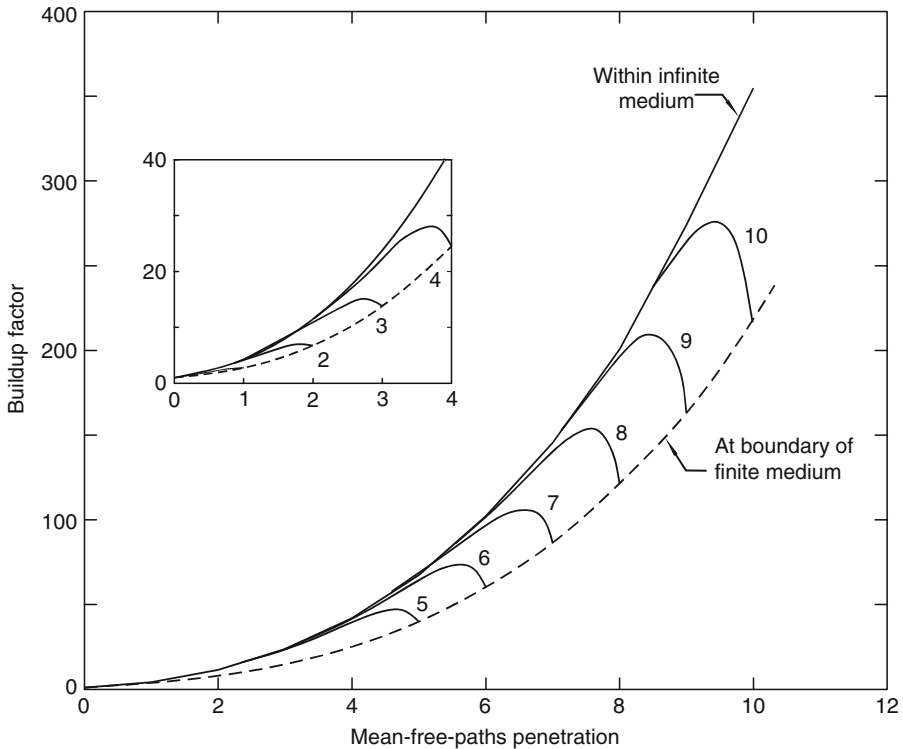
4.4 Buildup Factors for Heterogenous Media

4.4.1 Boundary Effects in Finite Media

Consider a point isotropic source at the center of a finite sphere of shielding material and a dose point at the surface. The sphere is surrounded by air, which may be approximated as a vacuum. The use of an infinite-medium buildup factor in calculating the dose at the boundary leads to an overestimate because, in fact, no photons are reflected back to the sphere from the space beyond the spherical surface. Because the error is on the side of overestimation of the dose, corrections are very often ignored.

► *Figure 22* illustrates the magnitude of the effect of a vacuum interface for a tissue medium. The lower bounding dashed lines are buildup factors for the dose at the surface of a sphere of given radius. The upper bounding solid lines are for the dose at the same radius in an infinite medium. The intervening lines are for points interior to the finite sphere. It is apparent that the effect of the boundary is insignificant for points more than about one mean free path from the surface. Buildup factors at vacuum boundaries of finite media are conveniently presented as the ratio $(B_x - 1)/(B_\infty - 1)$, in which B_x is the finite-medium buildup factor and B_∞ is the infinite-medium buildup factor. This ratio, which is illustrated in ► *Fig. 23*, can be used in many applications, because it has been found to be insensitive to whether the source is a point isotropic, plane isotropic, or plane perpendicular, and to the distance x from the source to the boundary.

Consider the same point isotropic source at the center of a finite sphere of shielding material and a dose point at the surface. The sphere is bounded not by a vacuum but by a tissue medium. This model is appropriate for determination of the phantom dose outside a shielding structure. For use in such calculations, Gopinath et al. (1987) determined adjustment factors to be applied to infinite-medium buildup factors. The adjustment factors, which are listed in ► *Table 13*, were adopted in the ANSI/ANS Standard (1991) for buildup factors. They were computed for parallel beam sources normally incident on shielding slabs, but may be used for point sources as well. The adjustment factor is to be used as follows. For the given shield material, first compute the absorbed dose in tissue at the location of the interface but within an infinite medium of the shielding material. Then multiply the result by the adjustment factor to yield the maximum absorbed dose in the tissue medium surrounding the shielding medium. The adjustment factor is insensitive to the thickness of the shielding medium.



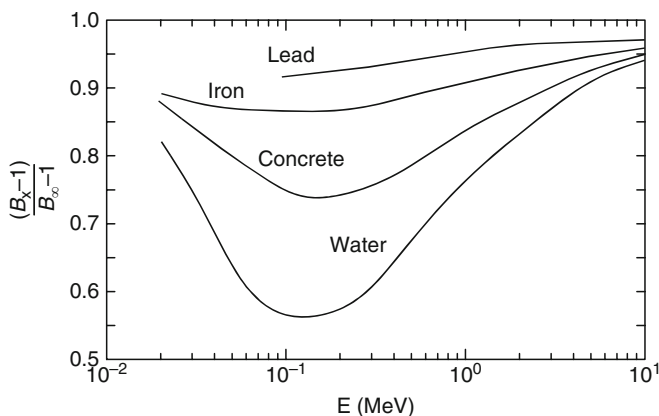
■ Figure 22

Finite-medium versus infinite-medium buildup factors for a 0.1-MeV point isotropic gamma-ray source in tissue. Calculations performed using the EGS4 code, courtesy of Sherrill Shue (1994), Kansas State University

4.4.2 Treatment of Stratified Media

The use of the buildup-factor concept for heterogenous media is of dubious merit, for the most part. Nevertheless, implementation of point-kernel codes for shielding design and analysis demands some way of treating buildup when the path from source point to dose point is through more than one shielding material. Certain regularities do exist, however, which permit at least an approximate use of homogenous-medium buildup factors for stratified shields. In general, though, the user of a point-kernel code must make the choice of a single material to characterize buildup. That choice is usually either the material with the greatest number of mean free paths between the source and the receiver or the material nearest the receiver.

For hand calculations, greater flexibility may often be used. For example, consider two-layer shields of optical thicknesses (mean free paths) ℓ_1 and ℓ_2 and effective atomic numbers Z_1 and Z_2 , numbered in the direction from source to detector. A commonly applied rule is that if $Z_1 < Z_2$, then the overall buildup factor is approximately equal to the buildup factor B_2 for material 2 evaluated at the total optical thickness $\ell_1 + \ell_2$. However, if $Z_1 > Z_2$, then the overall



■ Figure 23

Adjustment factor for the buildup factor at the boundary of a finite medium in terms of the infinite-medium buildup factor for the same depth of penetration. Exposure buildup calculations were performed for point isotropic sources in finite spheres and infinite media, using the EGS4 code, courtesy of Sherrill Shue, Nuclear Engineering Department, Kansas State University

■ Table 13

Adjustment factors to be applied to infinite-medium buildup factors when the maximum dose equivalent is to be evaluated in a thick-tissue medium bounding the shielding medium

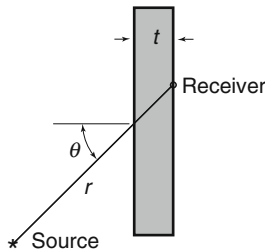
E (MeV)	Shielding medium			
	Water	Concrete	Iron	Lead
0.05	0.95	1.29	1.60	1.65
0.06	0.95	1.29	1.66	1.72
0.08	0.96	1.24	1.60	1.72
0.10	0.97	1.20	1.48	1.46
0.15	0.98	1.14	1.31	1.37
0.20	0.98	1.11	1.22	1.36
0.30	0.99	1.08	1.15	1.29
0.40	0.99	1.06	1.11	1.22
0.50	0.99	1.05	1.09	1.18
0.60	0.99	1.05	1.08	1.15
0.80	0.99	1.04	1.06	1.12
1.00	0.99	1.03	1.06	1.10
1.50	1.00	1.02	1.03	1.07
2.00	1.00	1.02	1.02	1.04
3.00	1.00	1.01	1.01	1.02

Source: ANSI/ANS (1991)

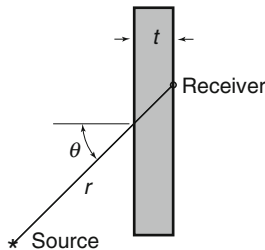
buildup factor is the product $B_1(\ell_1) \times B_2(\ell_2)$. More precise methods have been suggested by Kalos (Goldstein 1959), Broder et al. (1962), Kitazume (1965), Bünemann and Richter (1968), Harima (1983), Su and Jiang (1989), Harima and Hirayama (1993), and Shin and Hirayama (1994, 1995).

4.5 Broad-Beam Attenuation of Photons

4.5.1 Attenuation Factors for Photon Beams

It is often the case in dealing with the shielding requirements for a radionuclide or X-ray source that the source is located some distance in air from a wall or shielding slab, and the concern is with the radiation dose on the exterior (cold) side of the wall. Often too, the source is sufficiently far from the wall that the radiation reaches the wall in nearly parallel rays, and the attenuation in the air is quite negligible in comparison to that provided by the shielding wall. Shielding design and analysis in the circumstances just described, and illustrated in  Fig. 24, are addressed by the National Council on Radiation Protection and Measurements (NCRP 1976) in their widely used Report 49. Attenuation of photons from both monoenergetic and polyenergetic sources can be established in terms of the formula

$$D(P) = D^{\circ}(P)A_f, \quad (59)$$

in which $D(P)$ is the dose or response at point P (the receiver in  Fig. 24), $D^{\circ}(P)$ is the response in the absence of the shield wall, accounting only for the inverse-square attenuation, and A_f is an *attenuation factor* which depends on the nature and thickness of the shielding material, the source energy characteristics, and the angle of incidence θ . The attenuation factor incorporates the response function and combines buildup and exponential attenuation into a single factor A_f .

4.5.2 Attenuation of Oblique Beams of Photons

When monoenergetic beams of gamma rays are obliquely incident on shielding slabs, attenuation-factor and conventional ray-theory methods are not successful. The reason is that

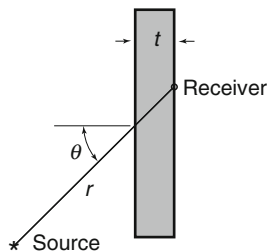


 Figure 24

Attenuation of gamma and X-rays from a point source in air by a shielding wall

the uncollided component of penetrating radiation is likely very small when compared with the collided component, and that the collided component is likely only very weakly dependent on the uncollided component. Obliquely incident beams, however, may be treated using a modified buildup factor that is a function of the angle of incidence. With respect to [Fig. 24](#), the beam attenuation factor in [\(59\)](#) may be written as

$$A_f = B(E_o, \cos \theta, \mu t) e^{-\mu t / \cos \theta}. \quad (60)$$

Values of the special buildup factor $B(E_o, \cos \theta, \mu t)$ are available in Shultis and Faw (2000) for concrete, iron, and lead shields for thicknesses as great as 10 mean free paths for wide ranges of photon energy and angle of incidence. Attenuation factors for concrete are listed in [Table 14](#). Attenuation factors for other materials may be found in the standard ANSI/ANS-6.4 (2006).

4.5.3 Attenuation Factors for X-Ray Beams

The appropriate measure of source strength for X-ray sources is the electron-beam current, and the appropriate characterization of photon energies, in principle, involves the peak accelerating voltage (kVp), the wave form, and the degree of filtration (e.g., mm Al) through which the X rays pass. Although the degree of filtration of the X rays would affect their energy spectra, there is only a limited range of filtrations practical for any one voltage, and within that limited range, the degree of filtration has little effect on the attenuation factor (NCRP 1976). Most diagnostic radiographic procedures for adult patients are conducted with an X-ray-beam quality of 2–3 mm Al half-value-layer (HVL) (Keriakes and Rosenstein 1980), which is consistent with 2.5–3.5 mm Al filtration of the X-ray source. The National Council on Radiation Protection and Measurements (NCRP 1989) requires at least 3.1 mm HVL and 3.1 mm Al filtration for three-phase generators with voltages 90 kVp or greater. Similar requirements are stated for lower voltages and for single-phase generators. Data on energy spectra from a wide variety of X-ray tubes and filtrations are available (Fewell and Shuping 1978; Fewell et al. 1981). For a given voltage, the greatest penetration would occur for a constant potential generator, but it has been found that X rays from modern three-phase generators are very nearly as penetrating (Simpkin 1989; Archer et al. 1994). Less penetrating are X rays from single-phase generators. Conservatism in design, allowing for upgrade in generators, dictates use of attenuation data for multiphase or constant-potential generators. If i is the beam current (mA) and r is the source–detector distance (m), then [\(59\)](#), with dose rate ($cGy \text{ min}^{-1} \simeq R \text{ min}^{-1}$) as the response, takes the form

$$\dot{D}(P) = \frac{i}{r^2} K_o A_f, \quad (61)$$

in which K_o is the *radiation output factor* with units of dose rate in vacuum (or air), per unit beam current at a distance of 1 m from the source in the absence of any shield. The dose unit was recently changed from exposure to air kerma (NCRP 1989). For the same voltage, the radiation output factor for a single-phase generator is less than that for a three-phase generator by a factor of $\sqrt{3}$ (NCRP 1989).

Attenuation factors for X rays normally incident on various shielding materials have been fit by Simpkin (1989, 1995) and by Archer et al. (1994) to the following expression, which was

■ Table 14

Attenuation factors for monoenergetic beams of gamma rays obliquely incident on slabs of ordinary concrete, expressed as the ratio of transmitted to incident air kerma

Photon energy (MeV)	Slab thickness (mfp)	$\cos \theta$						
		1.0	0.875	0.75	0.625	0.5	0.375	0.25
0.2	1	7.28E-01	6.53E-01	5.67E-01	4.57E-01	3.33E-01	2.15E-01	1.05E-01
	2	4.13E-01	3.28E-01	2.58E-01	1.77E-01	1.11E-01	6.09E-02	2.92E-02
	4	9.89E-02	6.77E-02	4.15E-02	2.61E-02	1.37E-02	7.87E-03	3.71E-03
	8	4.02E-03	2.15E-03	1.15E-03	6.08E-04	3.21E-04	1.65E-04	7.61E-05
0.661	1	6.78E-01	6.08E-01	5.25E-01	4.26E-01	3.11E-01	1.91E-01	8.49E-02
	2	3.69E-01	2.98E-01	2.24E-01	1.54E-01	9.23E-02	4.65E-02	1.96E-02
	4	8.86E-02	5.92E-02	3.62E-02	2.00E-02	9.95E-03	4.68E-03	2.01E-03
	8	3.51E-03	1.73E-03	7.86E-04	3.46E-04	1.50E-04	6.32E-05	2.47E-05
1.25	1	6.37E-01	5.73E-01	4.95E-01	4.01E-01	2.92E-01	1.76E-01	7.37E-02
	2	3.36E-01	2.69E-01	2.01E-01	1.35E-01	7.78E-02	3.60E-02	1.33E-02
	4	7.59E-02	4.92E-02	2.86E-02	1.45E-02	6.39E-03	2.54E-03	9.25E-04
	8	2.72E-03	1.21E-03	4.72E-04	1.67E-04	5.59E-05	1.85E-05	5.73E-06
2.5	1	5.94E-01	5.34E-01	4.62E-01	3.74E-01	2.71E-01	1.60E-01	6.29E-02
	2	2.99E-01	2.39E-01	1.77E-01	1.16E-01	6.41E-02	2.67E-02	8.02E-03
	4	6.30E-02	3.98E-02	2.20E-02	1.02E-02	3.76E-03	1.13E-03	3.08E-04
	8	2.04E-03	8.11E-04	2.88E-04	6.93E-05	1.64E-05	3.61E-06	7.23E-07
6.13	1	5.31E-01	4.76E-01	4.09E-01	3.30E-01	2.37E-01	1.36E-01	4.85E-02
	2	2.49E-01	1.97E-01	1.43E-01	9.21E-02	4.79E-02	1.74E-02	3.68E-03
	4	4.75E-02	2.91E-02	1.53E-02	6.37E-03	1.92E-03	3.78E-04	5.90E-05
	8	1.37E-03	5.03E-04	1.42E-04	2.67E-05	3.58E-06	4.17E-07	3.85E-08
10	1	4.98E-01	4.43E-01	3.82E-01	3.04E-01	2.11E-01	1.23E-01	3.96E-02
	2	2.23E-01	1.76E-01	1.27E-01	8.05E-02	3.99E-02	1.39E-02	2.51E-03
	4	4.08E-02	2.47E-02	1.24E-02	5.12E-03	1.46E-03	2.35E-04	2.41E-05
	8	1.14E-03	4.02E-04	1.08E-04	1.88E-05	2.16E-06	1.83E-07	1.20E-08

Source: MCNP calculations extending the work of Fournie and Chilton (1981) and Chen and Faw (1994)

originally recommended by Archer, Thornby, and Bushong (1983):

$$A_f = \left[\left(1 + \frac{\beta}{\alpha} \right) e^{\alpha y x} - \frac{\beta}{\alpha} \right]^{-1/\gamma}, \quad (62)$$

in which x is the material thickness, in units of millimeters. The coefficients for lead and concrete attenuation factors are listed in **Table 15** based on measurements and calculations of Archer et al. (1994), Simpkin (1987a), and Légaré et al. (1977). Conservative values of the output factor K_o given in the table conform to those given by Keriakes and Rosenstein (1980) and in NCRP Report 102 (1989).

In the design and analysis of shield walls for X-ray installations, it is necessary to account for a number of factors: (1) the *maximum permissible dose* for an individual situated beyond the shield wall during some prescribed time interval, such as 1 week, (2) the *workload*, which is the cumulative sum during the prescribed time interval of the product of the beam current and the duration of machine operation, (3) the *use factor*, which is the fraction of machine operation time that the X-ray beam is directed toward the shield wall, and (4) the *occupancy factor*, which is the fraction of the time during which the X-ray machine is in use and the beam is directed toward the shield wall behind which the individual at risk is actually present. All these factors are taken into account in the methodology of NCRP Reports 49 and 147. In addition, that methodology also treats leakage radiation from the X-ray machine and radiation scattered from patients or other objects present in the X-ray beam. The methodology is discussed at length by Simpkin (1987a,b, 1989, 1990) and by Chilton et al. (1984). A computer code for routine X-ray-shielding design and analysis [Simpkin 1987a] is available as code packages CCC-515/KUX and CCC-594/CALKUX from the Radiation Safety Information Computational Center, Oak Ridge National Laboratory, Oak Ridge, Tennessee.

Table 15

Fitting parameters for constant-potential X-ray attenuation factors computed for typical energy spectra from modern three-phase generators. The data for 30 and 35 kV are for low-voltage units with molybdenum anodes and beryllium windows. Otherwise, data are for tungsten anodes

kVcp	K_o^a	α (mm ⁻¹)	β (mm ⁻¹)	γ	α (mm ⁻¹)	β (mm ⁻¹)	γ
		Lead, $\rho = 11.35$ g/cm ³			Concrete, $\rho = 2.35$ g/cm ³		
30	2.61	38.80	178.0	0.3473	0.3173	1.698	0.3593
35	4.04	29.55	164.7	0.3948	0.2528	1.807	0.4648
50	0.87	8.801	27.28	0.2957	0.09032	0.1712	0.2324
70	2.19	5.369	23.49	0.5881	0.05087	0.1696	0.3847
100	4.69	2.500	15.28	0.7557	0.03925	0.08567	0.4273
120	7.62	2.246	8.950	0.5873	0.03566	0.07109	0.6073
140	8.74	2.009	5.916	0.4018	0.03345	0.07476	1.0470

^aRadiation output in units (mGy mA⁻¹ min⁻¹ at 1 m).

Source: Parameters α , β , γ , and K_o are from NCRP (2004); those for K_o are based on data of Archer et al. (1994)

4.5.4 The Half-Value Thickness

The half-value thickness, or half-value layer (HVL), is defined in terms of the attenuation of a parallel beam gamma or X rays, namely,

$$\text{HVL}(x) = \frac{-\ln 2}{d \ln A_f(x)/dx}. \quad (63)$$

For the special case of uncollided monoenergetic photons, $A_f(x) = e^{-\mu x}$, and

$$\text{HVL} = \frac{-\ln 2}{d \ln A_f/dx} = \frac{\ln 2}{\mu}. \quad (64)$$

However, when dealing with X rays or accounting for scattered gamma rays, the half-value thickness is a function of the depth of penetration, namely,

$$\text{HVL}(x) = \frac{-\ln 2}{d \ln A_f(x)/dx}. \quad (65)$$

At shallow penetrations, lower-energy photons are selectively removed and the HVL is relatively small. As the beam spectrum “hardens” with increasing penetration, the HVL increases. As may be shown from (62), the following relationships apply to X-ray data fit by that equation:

$$\lim_{x \rightarrow 0} \text{HVL} = \frac{\ln 2}{\alpha + \beta} \quad (66)$$

and


$$\lim_{x \rightarrow \infty} \text{HVL} = \frac{\ln 2}{\alpha}. \quad (67)$$

One other important application of the HVL. Values of the HVL at shallow penetration, usually for aluminum or copper, are widely used to characterize the penetration ability of X rays and as a parameter in the assessment of radiation doses from medical X rays. HVL data for a wide variety of materials and a wide variety of gamma- and X-ray source energies may be found in NCRP Reports 49 and 147 (1976, 2005).

4.6 Shield Heterogeneities

Occasionally, an analyst encounters a shield that includes regions of composition different from the bulk shield material. These regions may be large with a well-defined geometry, such as embedded pipes or instrumentation channels transverse to the direction of radiation penetration. By contrast, there may be incorporated into the shield material small irregularly shaped and randomly distributed voids or lumps of other material, such as pieces of scrap iron used to increase the effectiveness of a concrete shield against gamma radiation. For a large, well-defined heterogeneity in the shield (most often a single void or region of low-interaction coefficient), ray theory can often be used effectively. For simple geometry (e.g., a spherical or cylindrical void in a slab shield), (53) can be evaluated analytically. Otherwise, numerical integration techniques are used. Examples are given by Rockwell (1956), Burrus (1968b), and Chilton et al. (1984).

Rigorous calculation of the effect of such heterogenous regions in a shield usually requires Monte Carlo techniques. In this section, some simplified techniques, based on ray theory, illustrate the effect of shield heterogeneities.

Consider two rays through a shield (see  Fig. 25) containing randomly distributed small voids in a continuous phase which has an effective linear attenuation coefficient μ . Ray 1 travels a distance t with transmission probability $T_1 = e^{-\mu t}$. Ray 2 travels a distance $t - \delta$ with transmission probability $T_2 = e^{-\mu(t-\delta)}$. The average path length for these two rays is $\bar{t} = t - \delta/2$, and the average transmission probability is


$$\bar{T} = \frac{1}{2}(T_1 + T_2) = e^{-\mu \bar{t}} \cosh(\mu \delta/2) > e^{-\mu \bar{t}}. \quad (68)$$

Thus, it is seen that the use of the average path length of a ray through the shield material underpredicts the average transmission probability. If the voids are replaced by a material with an attenuation coefficient different from that of the shield material, a similar analysis shows that use of the average path length (in mean free paths) also underestimates the average transmission probability. This effect is known as *channeling* and its neglect leads to an overestimation of the effectiveness of a shield. Channeling is seen in shields with randomly included heterogeneities as well as in shields with well-defined placement of voids and heterogenous regions.

4.6.1 Limiting Case for Small Discontinuities

Suppose in (68) that $\delta \ll \mu^{-1}$, that is, the lumps or voids are much smaller in size than the radiation mean free path length in the continuous phase. In this case, the channeling effect is negligible, and shield transmission factors may be estimated using an average mass attenuation coefficient μ/ρ . Suppose that μ , ρ , and w are the effective linear attenuation coefficient, density,

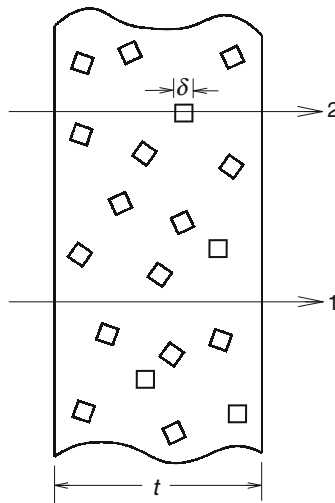


 **Figure 25**
Shield containing randomly distributed voids

and weight fraction of the continuous phase, and μ' , ρ' , and w' are the same quantities for the discontinuous phase. If v is the volume fraction of the voids or lumps in the shield and $\bar{\rho}$ is the average shield density, the average mass attenuation coefficient is

$$\overline{\mu/\rho} = \omega \left(\frac{\mu}{\rho} \right) + \omega' \left(\frac{\mu'}{\rho'} \right) = \frac{\rho(1-v)}{\bar{\rho}} \left(\frac{\mu}{\rho} \right) + \frac{\rho'v}{\bar{\rho}} \left(\frac{\mu'}{\rho'} \right), \quad (69)$$

and the transmission probability is thus

$$T(t) = e^{-(\overline{\mu/\rho})\bar{\rho}t} = e^{-(1-v)\mu + v\mu'}t} = e^{-\mu t} e^{-(\mu' - \mu)v t}. \quad (70)$$

This transmission probability is the same as if the shield materials (continuous and discontinuous components) were conceptually homogenized and the average attenuation coefficient for the homogenous mixture was used.

4.6.2 Small Randomly Distributed Discontinuities

Channeling effects have been treated by a statistical technique attributed to Coveyou (Burrus 1968a). Consider an infinite slab shield of thickness t , uniformly and normally illuminated on one side by radiation. The shield contains randomly distributed lumps with a different linear attenuation coefficient (μ') from that of the shield material (μ). Suppose that the mean chord length through a lump is δ . Then it can be shown that

$$T(t) = e^{-\mu t} e^{-(\mu' - \mu)v t / c_o}. \quad (71)$$

Here, c_o is the *cross-section effectiveness ratio*, namely,

$$c_o = \frac{-(\mu' - \mu)v\delta}{\ln[(1-v) + v e^{-(\mu' - \mu)\delta}]}. \quad (72)$$

For an arbitrary convex lump, the mean chord length is just four times the volume/surface area ratio. For concave and irregularly shaped lumps, the value of δ must be determined by specific calculation or by measurement of slices of the shield material.

5 Neutron Shielding

Neutron shielding analysis is often quite complex, involving not only attenuation of primary or source neutrons but also production and attenuation of secondary particles. These associated problems include the production of photons from neutron inelastic scattering, slowing down and thermalization of neutrons, capture of thermal neutrons leading to capture gamma photons, and even production of secondary neutrons as a result of fission or ($n, 2n$) reactions. Moreover, none of these associated problems is accurately solved using elementary techniques. To obtain accurate results with errors of only a few percentage, it is necessary to use sophisticated numerical techniques based on the exact descriptions of photon and neutron transport in the shield.

In this section, several of the simplified techniques developed for neutron shielding over the past 50 years are reviewed. Although these techniques are seldom used directly in modern shield analysis, the ideas behind them provide an insight into important mechanisms that determine the effectiveness of a neutron shield. Such insight allows the analyst to interpret and assess more critically results obtained with large computer codes.

5.1 Neutron Versus Photon Calculations

The development of simplified techniques for neutron shielding analysis is considerably more difficult than for photon shielding. The use of buildup factors, while theoretically applicable to any type of indirectly ionizing radiation, is much more difficult to apply to the neutron problem. The buildup of scattered neutrons depends strongly on the isotopic composition of the medium, on the neutron energy spectrum, and above all, on the problem geometry. Near a free surface, neutron densities generally decrease much more dramatically than in the photon case. Consequently, the use of infinite-medium buildup factors, which work so well for photon analyses, may introduce serious errors for neutron analyses.

Another serious difference between photon and neutron calculations arises from the evolution of thinking about fluence-to-dose conversion coefficients. Many different response-function sets have been issued by various national and international institutions over the past 50 years. Because the photon quality factor is independent of the photon energy, the ratio of different conversion coefficients, except at very low energies, is nearly constant, as is seen in [▶ Fig. 13](#). Thus, measured or calculated photon doses based on one conversion coefficient can be converted easily to another type of dose by an appropriate multiplicative constant. By contrast, the many neutron response functions that have been used at one time or another are not simply related to each other by a multiplicative constant (see, for example, [▶ Fig. 14](#)). Thus, much neutron shielding data (e.g., point kernels, albedos, transmission factors, etc.) reported in obsolete units cannot be rigorously used in modern shielding analysis. At best, only approximate conversions can be made; and if accurate results are needed, then there is no recourse but to repeat the original calculations or measurements using modern dose units.

5.2 Fission Neutron Attenuation by Hydrogen

There is one widely encountered situation for which the attenuation of a fast-neutron beam can be expected to be somewhat insensitive to the buildup of scattered neutrons. Elastic scattering from light elements results in a significant portion of the neutron's kinetic energy being lost, on the average, in a single scatter. In particular, for scattering from hydrogen the average energy loss is one-half of the initial neutron energy and, consequently, the scattering of a fast neutron on hydrogen acts essentially as an effective absorption or removal interaction because the neutron is, on the average, removed from the fast-neutron energy region by a single scatter. Thus, for the deep penetration of fast neutrons, the fast-neutron fluence might be expected to be very nearly equal to that of uncollided fast neutrons deep in an hydrogenous medium. In addition, the cross section for hydrogen in the MeV-energy region increases as the neutron energy decreases; hence, a low-energy neutron is much more likely to scatter from hydrogen than is a high-energy neutron. In effect, this characteristic of the hydrogen cross section implies

that, once a fast neutron interacts in an hydrogenous medium, the subsequent scattering or slowing-down interactions occur relatively near the point of the first scattering interaction.

From these arguments, it is then possible to derive a point kernel for the uncollided fast-neutron fluence in an infinite hydrogenous medium (Albert and Welton 1950). Consider a point-fission source which emits S_p fission neutrons with an energy spectrum given by $\chi(E)$ in an infinite hydrogenous medium with a hydrogen atom density of $N_H \text{ cm}^{-3}$. The uncollided fluence $\Phi_H^o(r, E)$ at distance r from the source, if one neglects any nonhydrogen collisions, is

$$\Phi_H^o(r, E) = \frac{S_p \chi(E)}{4\pi r^2} \exp[-N_H \sigma_H(E)r]. \quad (73)$$

Because the total fast-neutron fluence is of interest, (73) must be integrated over all fission energies. To perform such an integration, the functional form of $\chi(E)$ and $\sigma_H(E)$ must be used, and because the fast fluence is dominated by those neutrons with energies greater than 4 MeV, a simpler form from that of (9) may be used, namely,

$$\chi(E) \simeq A e^{-aE}, \quad (74)$$

where the parameters A and a depend on the fissile isotope and the energy range of the fit. For the energy range 2–12 MeV, the hydrogen total cross section (which is essentially the scattering cross section) may be approximated by (Blizard 1962)

$$\sigma_H(E) \simeq B E^{-b}, \quad (75)$$

where $B = 5.13 \times 10^{-24}$, $b = 0.725$, and σ_H is in units of cm^2 when E is in units of MeV.

As is shown by Chilton, Shultis, and Faw (1984), integration of (73) over all energy yields

$$\Phi_H^o(r) = \frac{S_p A \beta}{4\pi r^2} r^{\gamma/2} \exp(-\alpha r^\gamma), \quad (76)$$

where

$$\gamma \equiv 1/(1+b), \quad (77)$$

$$\beta \equiv \left[\frac{2\pi\gamma(N_H B b)^\gamma}{a^{1+\gamma}} \right]^{1/2}, \quad (78)$$

and

$$\alpha \equiv \frac{1}{\gamma} \left(\frac{a}{b} \right)^{b\gamma} (N_H B)^\gamma. \quad (79)$$

The presence of heavier components in the attenuating medium (e.g., the oxygen in a water shield) also degrades the fast neutrons in energy, although not nearly as well as the hydrogen. Many experiments have been performed to measure the attenuation of fast fission neutrons in hydrogenous media. Experimentally, it is found that the fast-neutron fluence falls off slightly faster with increasing distance from the source than (76) would indicate. In particular, experimental data for attenuation in water reveal that the spatial distribution of the total fast-neutron fluence can be related to that in hydrogen by

$$\Phi^o(r) = \Phi_H^o(r) \exp(-\mu_{r,O} r); \quad (80)$$

that is, the nonhydrogen component (oxygen) contributes an exponential attenuation factor. The constant $\mu_{r,O}$, although given the symbol of an attenuation coefficient, is an empirically derived constant to account for the nonhydrogen attenuation. Because of the similarity of this constant to the coefficient in the usual exponential attenuation of uncollided radiation, it is called the *removal coefficient*, although numerically it is usually significantly less than the actual total attenuation coefficient. More is said in the next section about the physical basis of the removal coefficient. Thus, by correcting for the attenuation of the oxygen, the fast-neutron fluence in water for a point fission source may be written as

$$\Phi^o(r) = \frac{A\beta S_p}{4\pi r^2} r^{\gamma/2} \exp(-\alpha r^\gamma - \mu_{r,O}r). \quad (81)$$

It should be emphasized at this point that the fast-neutron fluence kernel obtained from (81), with $S_p = 1$, is not adequate for detector-response evaluation because no account is taken of the buildup of small-angle-scattered neutrons which have lost very little energy. The usefulness of the kernel, however, is to suggest how the uncollided fluence (and hence, dose) can be expected to vary with distance from the source. Consequently, by fitting the functional form of the kernel to experimental data, one could expect to obtain a reasonably accurate semiempirical result. Such a fitting technique could be expected to lead to better agreement with experiment because the buildup of fast neutrons could be incorporated empirically. One widely used result is due to Casper (1960), who obtained the following fast-neutron tissue-absorbed-dose kernel for a point ^{235}U fission source in water:

$$\mathcal{G}(r) = \frac{5.39 \times 10^{-11}}{4\pi r^2} r^{0.349} \exp(-0.422r^{0.698} - 0.0308r), \quad (82)$$

where r has units of centimeters and \mathcal{G} has units of Gy for a source strength of one fission neutron.

Other functional forms have been fit to experimental dose data or to values calculated by the more elaborate neutron transport techniques. One particularly simple form for a ^{235}U fission source, which can be readily incorporated into analytical kernel calculations, expresses the fast-neutron tissue-absorbed dose kernel for water in terms of exponential functions (Grotenhuis 1962; Glasstone and Sesonske 1963), in the same units as used above, as

$$\mathcal{G}(r) = \frac{10^{-12}}{4\pi r^2} (23.9e^{-0.129r} + 2.89e^{-0.091r}). \quad (83)$$

Another empirical result, with the same units, which fits the experimental water kernel for absorbed dose in tissue more accurately than do the previous two results and which is valid over a much wider range of r ($0 \leq r \leq 300$ cm), is given by Brynjolfsson [1975] as

$$\mathcal{G}(r) = \frac{2.6 \times 10^{-11}}{4\pi r^2} e^{-br}, \quad (84)$$

where

$$b = \left[0.126 - 0.0001773 \left(r - \frac{r^2}{600} \right) \right] \left[1 - \left(2 + \frac{r^4}{5000} \right)^{-1} \right]. \quad (85)$$

A comparison of the foregoing three empirical tissue-absorbed dose-point-kernels in water with accurately calculated values is presented in [Table 16](#).

■ Table 16

Absorbed dose kernels in tissue from a point ^{235}U fission source in water (\mathcal{G}_o) obtained by the moments method (Goldstein 1959)

Distance from source (cm)	$4\pi r^2 \mathcal{G}_o(r)$ moments methods (Gy cm ²)	Ratio to \mathcal{G}_o^a		
		$\mathcal{G}_1/\mathcal{G}_o$	$\mathcal{G}_2/\mathcal{G}_o$	$\mathcal{G}_3/\mathcal{G}_o$
0	2.63×10^{-11}	0	1.02	0.98
10	1.05×10^{-11}	1.03	0.74	0.97
20	2.30×10^{-12}	1.19	0.99	1.04
30	7.08×10^{-13}	1.06	0.97	0.99
60	2.43×10^{-14}	0.94	0.94	0.99
90	9.89×10^{-16}	0.95	1.03	1.05
120	5.53×10^{-17}	0.85	1.03	0.98

^a \mathcal{G}_1 calculated from (82); \mathcal{G}_2 calculated from (83); and \mathcal{G}_3 calculated from (84)

5.3 Removal Cross Sections

In many realistic situations, fission neutrons are attenuated not only by an hydrogenous medium but also by an interposed nonhydrogenous shield such as the wall of a steel pressure vessel. Many experimental data have been obtained for such situations; and under special circumstances, the effect of the nonhydrogen component can be very simply accounted for by an exponential attenuation factor, much as was done for the oxygen correction examined in the preceding section.

An idealized fast-neutron attenuation experiment is shown in ► Fig. 26. A point isotropic fission source in an infinite homogenous hydrogenous medium is surrounded by a spherical shell of thickness t composed of a nonhydrogenous material. Experimental results reveal that under certain circumstances, the tissue-absorbed dose D' with the shell in position (i.e., at a distance $r_1 + r_2$ of hydrogenous medium plus a thickness t of the nonhydrogenous component) is related to the dose D at a distance $r = r_1 + r_2$ from the source, without the shell, by

$$D' = D \left(\frac{r}{r+t} \right)^2 e^{-\mu_r t}, \quad (86)$$

where μ_r is called the *removal coefficient* and is a constant characteristic of the nonhydrogenous component for a given fission-neutron energy spectrum.

Two important restrictions on the experimental arrangement are required for the validity of (86). First, it is important that there be at least 6 g cm^{-2} of hydrogen, equivalent to 50 cm of water, between the nonhydrogenous component and the observation position. Second, the thickness t must be such that $\mu_r t$ is less than about 5.

Although the factor $\exp(-\mu_r t)$ in (86) appears to indicate that absorption of neutrons is taking place in the nonhydrogenous component, the principal interactions are scattering interactions in which the fission neutrons are degraded in energy only slightly. However, the

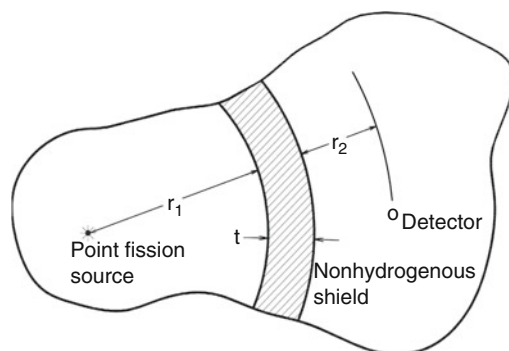


Figure 26

Idealized experimental geometry for the measurement of the removal cross-section in which a nonhydrogenous shield of thickness t is placed between the point-fission source and the detector in an infinite hydrogenous medium

hydrogen in the material following the nonhydrogenous component (one of the two experimental restrictions) moderates or removes the slightly slowed-down neutrons more quickly than those neutrons which traverse the nonhydrogenous component without any energy loss. If, following the nonhydrogenous component, there is sufficient hydrogen to effect the removal of the neutrons which are slightly moderated, the spatial variation of the fast-neutron tissue-absorbed dose D can be obtained from one of the kernels of (82) to (84), for the case that the hydrogenous medium is water.

If a series of different materials is inserted into the hydrogenous medium, the removal term $\exp(-\mu_r t)$ of (86) becomes simply $\exp(-\sum_i \mu_{r,i} t_i)$, where $\mu_{r,i}$ is the removal coefficient for the i th slab of thickness t_i . Similarly, if a slab of a mixture of elements is inserted, the removal coefficient μ_r for the slab is given by $\sum_i N_i \sigma_{r,i}$, where N_i is the atom density of the i th element with microscopic removal cross section $\sigma_{r,i}$. This additive nature of the relaxation lengths for the nonhydrogen components, which is a direct consequence of (86), has generally been supported by experiment, although some deviations have been noted.

The (n, γ) absorption cross-section for most materials in the MeV-energy region is negligible and plays no significant role in the removal of fast neutrons. Conceptually, the removal cross-section is that fraction of the total fast-neutron cross section, averaged over energies of fission neutrons, representing inelastic and elastic scattering through a large scattering angle (i.e., scattering in which there is significant energy loss). Thus, the removal cross section can be expected to be somewhat less than the total cross section. As an approximation, $\mu_r \approx \frac{2}{3} \bar{\mu}_t$, where $\bar{\mu}_t$ is the average total attenuation coefficient in the energy range 6–8 MeV (Goldstein and Aronson 1954).

There is no firm theoretical reason for the removal cross section to be a material constant, and indeed, it might be expected to vary with the fission neutron energy spectrum, the thickness of the nonhydrogenous shield, amount of hydrogenous material on either side of the slab, and the geometry of the experiment. However, experimental results have shown that for most situations (provided that the slab is less than five removal relaxation lengths thick), μ_r can often be taken as a constant for a given incident fission spectrum. In Table 17, the measured values of removal cross sections for several materials are presented. To obtain removal cross sections

■ Table 17

Measured microscopic removal cross sections of various elements and compounds for ^{235}U fission neutrons

Material	σ_r (b/atom)	Material	σ_r (b/atom)
Aluminum	1.31 ± 0.05	Oxygen	0.99 ± 0.10
Beryllium	1.07 ± 0.06	Tungsten	3.36
Bismuth	3.49 ± 0.35	Zirconium	2.36 ± 0.12
Boron	0.97 ± 0.10	Uranium	3.6 ± 0.4
Carbon	0.81 ± 0.05	Boric oxide, B_2O_3	4.30 ± 0.41^a
Chlorine	1.2 ± 0.8	Boron carbide, B_4C	4.7 ± 0.3^a
Copper	2.04 ± 0.11	Fluorothene, $\text{C}_2\text{F}_3\text{Cl}$	6.66 ± 0.8
Fluorine	1.29 ± 0.06	Heavy water, D_2O	2.76 ± 0.11^a
Iron	1.98 ± 0.08	Heavimet ^b	3.22 ± 0.18
Lead	3.53 ± 0.30	Lithium fluoride, LiF	2.43 ± 0.34^a
Lithium	1.01 ± 0.05	Oil, CH_2 group	2.84 ± 0.11^a
Nickel	1.89 ± 0.10	Paraffin, $\text{C}_{30}\text{H}_{62}$	80.5 ± 5.2

^aRemoval cross-section is in barns per molecule or per group.

^b90 wt% W, 6 wt% Ni, 4 wt% Cu; cross-section is weighted average.

Source: Blizard (1962); Chapman and Storrs (1955)

for other elements, the following empirical formulas (in units of cm^2/g) have been obtained to permit interpolation between these measured values (Zoller 1964):

$$\frac{\mu_r}{\rho} = \begin{cases} 0.190Z^{-0.743} & Z \leq 8 \\ 0.125Z^{-0.565} & Z > 8 \end{cases} \quad (87)$$

or

$$\frac{\mu_r}{\rho} = 0.206A^{-1/3}Z^{-0.294}, \quad (88)$$

where A and Z are the atomic mass and atomic number, respectively, for the element of concern.

5.4 Extensions of the Removal Cross Section Model

5.4.1 Effect of Hydrogen Following a Nonhydrogen Shield

In the preceding section, it was emphasized that the applicability of the removal cross section model of (86) was dependent on whether there is sufficient hydrogen following the nonhydrogenous component to complete the removal of neutrons which have been degraded slightly in energy by the nonhydrogen component. If there is insufficient hydrogen following the

nonhydrogenous component, not all the neutrons are removed, and the removal cross-section appears to have a smaller value. In such a situation, the removal cross-section is no longer simply a material property, but it is also a function of the hydrogen thickness following the nonhydrogen component (Shure et al. 1969).

Values of removal cross sections are insensitive to the lower cutoff energy used to define the lower limit of the fast-neutron fluence. However, for hydrogen-deficient shields, the lower cutoff energy yields slightly smaller values for the removal cross section, as would be expected, because the limited hydrogen available is unable to remove all the degraded neutrons and consequently, leaves relatively more fast neutrons to penetrate the shield.

5.4.2 Homogenous Shields

For homogenous systems in which the nonhydrogen material is uniformly dispersed in a hydrogenous medium such as concrete, the removal cross section concept can also be applied if the hydrogen concentration is sufficiently high. For such situations, the fast-neutron tissue-absorbed dose $D(r)$ from a point fission source of strength S_p can be related to the dose $D_H(r)$ in a pure hydrogen medium of equivalent hydrogen density by the equation

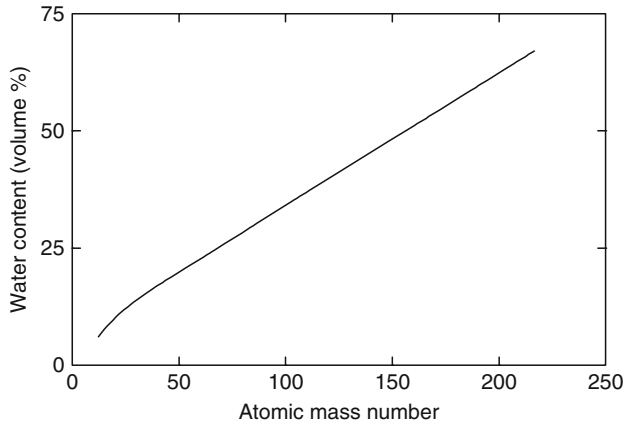
$$D(r) = D_H(r) \exp\left(-\sum_{i=1}^N N_i \sigma_{r,i}^{\text{homo}} r\right), \quad (89)$$

where $\sigma_{r,i}^{\text{homo}}$ is the microscopic removal cross section of the i th nonhydrogen component for a fission neutron source, and N_i is the atom density of the i th nonhydrogen species. The pure hydrogen dose $D_H(r)$ in this result can be calculated in terms of a point-source dose kernel $\mathcal{G}_H(r)$ as $D_H(r) = S_p \mathcal{G}_H(r)$, where $\mathcal{G}_H(r)$ can be inferred from the water kernels of (82) to (85) by eliminating the oxygen contribution and correcting for the different hydrogen atomic density. For example, using Casper's semiempirical kernel of (82), with the oxygen removal term eliminated, $\mathcal{G}_H(r)$ can be expressed as

$$\mathcal{G}_H(r) = \frac{5.39 \times 10^{-11}}{4\pi r^2} \left\{ (Yr)^{0.349} \exp[-0.422(Yr)^{0.698}] \right\}, \quad (90)$$

where Y is the ratio of the hydrogen atom density in the mixture to that in pure water. For most elements, the homogenous removal cross sections in (89) can be taken equal to the heterogenous removal cross section (see [Table 17](#)); although for lighter elements, the homogenous removal cross sections appear to be 5–10% smaller than those for heterogenous media (Tsy-pin and Kukhtevich 1968).

For (89) to be valid, it is imperative that there be sufficient hydrogen present to remove neutrons degraded in energy by collisions with the heavy component. In [Fig. 27](#), the lowest concentration of water required for the validity of (89) is presented as a function of the atomic mass of the nonwater component. Note that the heavier the nonhydrogen component, the more the water is required. It should also be noted that the concrete, which is a very important neutron-shielding material, is just barely able to pass this criterion. One should be cautious therefore in the application of (89) to a very dry concrete.



■ Figure 27

Lowest volume concentration of water in a homogenous mixture containing heavy components with an average atomic mass A for (89) to be valid. From Tsypin and Kukhovich (1968)

5.4.3 Energy-Dependent Removal Cross Sections

In many situations, the neutron spectrum incident on an hydrogenous shield is not that of a fission source, but may have a completely different energy dependence, $\chi(E)$, as a result of penetration through other materials or from a difference in the physical source of the fast neutrons (e.g., a fusion reaction). In such situations, the removal concept can again be used by employing energy-dependent removal cross sections. As with the fission-spectrum case, it is important that sufficient hydrogen be present to remove those neutrons which have been slightly degraded by collisions with the nonhydrogenous components in the shield. For any point isotropic source of strength S_p and energy spectrum $\chi(E)$, the tissue-absorbed dose in a distance r away from the source in an infinite homogenous medium can, by analogy with our previous results, be written as

$$D = \int_0^{\infty} dE S_p \chi(E) \mathcal{G}_H(r, E) \exp\left[-\sum_{i=1}^N N_i \sigma_{r,i}(E) r\right], \quad (91)$$

where $\mathcal{G}_H(r, E)$ is the neutron dose kernel at a distance r from a unit-strength isotropic source emitting neutrons of energy E in a pure hydrogen medium of density equivalent to that in the shield material; $\sigma_{r,i}(E)$ is the microscopic removal cross section of the i th nonhydrogen shield component for neutron energy E ; and N_i is the atom density of the i th shield component.

The use of (91) to calculate the dose depends on two crucial pieces of information: the hydrogen dose kernel $\mathcal{G}_H(r, E)$ and the energy-dependent removal coefficient $\mu_{r,i}$. As a rough approximation for the energy-dependent hydrogen dose kernel, one may use the following result [Tsypin and Kukhovich 1968]:

$$\mathcal{G}_H(r, E) = \frac{1}{4\pi r^2} \exp[-\mu_H(E)r][1 + \mu_H(E)r]\mathcal{R}_D(E), \quad (92)$$

which is simply the uncollided dose kernel times an approximate buildup-factor correction, $[1 + \mu_H(E)r]$, times the tissue-absorbed dose-response function $\mathcal{R}_D(E)$. Here $\mu_H(E)$ is

the total hydrogen attenuation coefficient at energy E . An alternative is to use the following empirical result for the tissue-absorbed dose kernel (Shultis and Faw 2000) as

$$\mathcal{G}_H(r, E) = \frac{A_0(E)}{4\pi r^2} \exp[-A_1(E)Yr - A_2(E)(Yr)^2 + \mu_{r,O}(E)Yr], \quad (93)$$

in which Y is the ratio of the hydrogen atom density to that in water, and $\mu_{r,O}(E)$ is the energy-dependent removal coefficient for oxygen in water. The parameters $A_0(E)$, $A_1(E)$, and $A_3(E)$ are given in ► [Table 18](#).

A more severe limitation of the energy-dependent removal-cross-section theory is the availability of values for removal cross sections. Only sparse experimental data are available, and those have rather large associated uncertainties (Gronroos 1968; Tsypin and Kukhtevich 1968). In many cases, it is necessary to use theoretical values of removal cross sections. Generally, the lack of information about energy-dependent removal cross sections as well as a lack of an accurate hydrogen-attenuation dose kernel limit the use of removal-cross-section theory for dose calculations. Of particular concern in shield calculations are those energy regions for which these removal cross-sections have minima, that is, those energies for which neutrons can stream through the shield material with a little chance of being removed. To obtain accurate results for nonfission spectra, more elaborate transport-theory based methods are called for. However, for an approximate calculation, (91) may be useful.

5.5 Fast-Neutron Attenuation without Hydrogen

In nonhydrogenous material, accurate calculation of the attenuation of fast neutrons requires numerical procedures based on transport theory or removal-diffusion theory. For rough estimates of fast-neutron penetration, however, a few empirical results have been obtained and are summarized in this section.

■ **Table 18**

Constants for the empirical fit of the tissue-absorbed dose kernel for a point-monoenergetic neutron source in water as given by (93).^a

Source energy (MeV)	A_0 (Gy cm ²)	A_1 (cm ⁻¹)	A_2 (cm ⁻²)	Range of fit (cm)
2	7.31×10^{-11}	0.1716	6.274×10^{-4}	10 to 80
4	9.55×10^{-11}	0.1115	3.792×10^{-4}	10 to 110
6	8.63×10^{-11}	0.07953	1.913×10^{-4}	10 to 140
8	7.04×10^{-11}	0.06362	1.634×10^{-4}	10 to 140
10	6.09×10^{-11}	0.05723	1.414×10^{-4}	10 to 140
14	5.42×10^{-11}	0.04925	1.318×10^{-4}	10 to 140

^aThese values were obtained by a least-squares fit to the results of moments calculations (Brynjolfsson 1975; Goldstein 1959). Agreement is within $\pm 10\%$ over the indicated range of each fit

Important nonhydrogenous materials frequently encountered in shield design include iron, lead, and aluminum used as structural material or for photon shielding. Fast neutrons are attenuated very poorly by these materials. For Po–Be neutrons, relaxation lengths are found to be 16 cm for iron, 24 cm for lead, and 30 cm for aluminum (Dunn 1957). Hence, fast-neutron attenuation through only a few centimeters of these materials can be neglected for practical purposes.

However, for thick nonhydrogenous shields, fast neutrons may be appreciably attenuated. Beyond a few mean-free-path lengths from a fast-neutron source in an infinite nonhydrogenous medium, the fast-neutron fluence has been observed to decrease exponentially. However, the relaxation length is a characteristic not only of the material but also of the source energy and the low-energy limit used to define the fast-neutron region (i.e., the “fast group” of neutrons). Specifically, the total fast-neutron fluence $\Phi_\alpha(r)$ above some threshold energy E_α at a distance r greater than three mean-free-path lengths from a point monoenergetic source of strength S_p and energy E_o in an infinite homogenous medium, can be calculated by (Broder and Tsypin 1968)

$$\Phi_\alpha(r) \simeq \int_{E_\alpha}^{E_o} \Phi(r, E) dE = \frac{S_p B_o}{4\pi r^2} \exp(-r/\lambda_r). \quad (94)$$

The factor B_o corrects for the initial buildup of scattered fast neutrons and, after a few mean-free-path lengths, becomes a constant. Both the initial buildup factor and the relaxation length λ_r are empirical constants and depend on the attenuating material, the source energy, and the threshold energy E_α . In **Table 19**, values of B_o and λ_r are presented for a few materials.

If the fast-neutron source is distributed in energy, the technique above can still be applied by dividing the source energy region into several contiguous narrow energy ranges and then treating the neutrons in each range as monoenergetic neutrons, governed by (94). Thus,

$$\Phi_\alpha = \frac{S_p}{4\pi r^2} \sum_i f_i B_o^i \exp(-r/\lambda_r^i), \quad (95)$$

where f_i is the fraction of neutrons emitted in the i th energy range and B_o^i and λ_r^i are the initial buildup factor and relaxation length, respectively, for neutrons at the mean energy of the i th

Table 19
Initial Buildup Factors and Relaxation Lengths in Different Media for Monoenergetic Neutron Sources. The energy range for the fast-neutron flux density is 1.5 MeV to E_o

Medium	Density (g cm ⁻³)	$E_o = 4$ MeV		$E_o = 14.9$ MeV	
		B_o	λ_r (cm)	B_o	λ_r (cm)
B ₄ C	1.67	2	12.0	2	17.2
C	1.67	2	11.4	2	19.2
Al	2.70	2.5	14.1	2.5	15.8
Fe	7.83	2.5	7.6	2.7	8.2
Pb	11.3	4	15	2.9	15.3

Source: Broder and Tsypin (1968)

energy range. At large distances into the shield, only a few terms in the summation of (95) are significant, those corresponding to neutrons whose energies are at minima in the total effective nuclear cross section.

The exponential attenuation of the fluence given empirically by the equations above can also be applied to media composed of a mixture of elements by using a weighted average of the relaxation lengths for the individual components, that is,

$$\lambda_r = \left(\sum_i \frac{\rho'_i}{\rho_i} \frac{1}{\lambda_r^i} \right)^{-1}, \quad (96)$$

where λ_r^i is the relaxation distance of the i th material at density ρ_i , and ρ'_i is the actual density of the i th material in the mixture, which may be different from ρ_i .

One of the major difficulties in applying the above technique is the lack of empirical data for initial buildup or, more important, for values of the relaxation lengths. Often, values for λ_r are chosen as the reciprocal of the removal coefficient μ_r for neutrons above 3 MeV. In reality, one can expect the relaxation length to be somewhat larger because hydrogen is not present to remove the slightly degraded neutrons. Typically, the removal coefficient should as a rule of thumb be reduced by a factor of about 2 to compute λ_r . However, the use of such inferred values for the relaxation lengths introduces a great deal of uncertainty in the fast-neutron fluences calculated, and consequently, such estimates must be used cautiously.

The procedures described here for estimating the fast-neutron fluence are, at best, only approximate. For design work, it is necessary to employ more elaborate methods based on the neutron-transport equation.

5.6 Intermediate and Thermal Fluences

The attenuation of fast neutrons in a shield necessarily leads to neutrons with intermediate and, eventually, thermal energies. The resulting intermediate-energy neutrons can contribute appreciably to the transmitted neutron dose in a shield, and the thermal neutrons, which are readily absorbed in the shield material, lead to the production of high-energy capture gamma photons. In many instances, the capture gamma-ray dose at the shield surface is the dominant consideration in the shield design. Thus, an important aspect of neutron shield analyses is the calculation of thermal and intermediate neutron fluences.

The thermal and intermediate neutrons in a shield arise from the thermalization of fast neutrons as well as from thermal and intermediate-energy neutrons incident on the shield's surface. Many elaborate techniques have been developed to compute accurately the thermal and intermediate neutron fluences; however, two simplified methods, based on diffusion and Fermi age theory, are first presented.

5.6.1 Diffusion Theory for Thermal Neutron Calculations

For hydrogenous shields, the fast neutrons are rapidly thermalized once they are removed from the fast group, as a result of the higher hydrogen cross section experienced by the neutrons removed. Consequently, as a rough approximation, the neutrons can be assumed to become

thermalized at the point at which they are removed from the fast group. In effect, the migration of intermediate-energy neutrons is neglected. The diffusion of the thermal neutrons then establishes the thermal-neutron fluence inside the shield. The thermal neutron flux density Φ_{th} can be calculated by use of the steady-state, one-speed, diffusion model for neutron transport (Lamarsh 1966),

$$D\nabla^2\Phi_{th}(\mathbf{r}) - \mu_a\Phi_{th}(\mathbf{r}) + S_{th}(\mathbf{r}) = 0, \quad (97)$$

where D and μ_a are the diffusion coefficient and linear absorption coefficient (macroscopic absorption cross section), respectively, for thermal neutrons.

Neutrons appear in the thermal group as they are lost from the fast group. Thus, the thermal neutron source term in (97) can be determined from the spatial rate of change of the fast neutrons traveling in direction Ω , namely,

$$S_{th}(\mathbf{r}) = -\nabla \cdot \int_{4\pi} d\Omega \Omega \Phi_f(\mathbf{r}, \Omega). \quad (98)$$

To a good approximation, the fast neutrons can be considered to be moving directly away from their source because there is little change in direction from the time the neutron leaves the source until it is removed from the fast region. Also, far from the fast neutron sources, the fast neutrons are all traveling in approximately the same direction \mathbf{n} directly away from their source, so that $\int_{4\pi} d\Omega \Omega \Phi_f(\mathbf{r}, \Omega) \simeq \mathbf{n}\Phi_f(\mathbf{r})$. Thus, the source of the thermal neutrons can be estimated from the fast-neutron fluence as

$$S_{th}(\mathbf{r}) \simeq -\nabla \cdot \mathbf{n}\Phi_f(\mathbf{r}). \quad (99)$$

The vector \mathbf{n} is a unit vector directed away from the fast-neutron source in the direction of fast-neutron travel or, equivalently, the direction in which the fast fluence decreases the most rapidly (i.e., opposite to the direction of the gradient of Φ_f).

For example, consider a plane shield ($0 < x < T$) in which the fast-neutron fluence is represented by an exponential function, or more generally, by a sum of N exponentials; that is,

$$\Phi_f(x) = \sum_{i=1}^N \Phi_f^i(0) \exp[-k_f^i x], \quad (100)$$

where $\Phi_f^i(0)$ and k_f^i are adjusted to give the best fit to the given fast-neutron fluence. For this case, the diffusion equation becomes

$$\frac{d^2\Phi_{th}(x)}{dx^2} - \frac{\mu_a}{D}\Phi_{th}(x) = -\frac{1}{D} \sum_{i=1}^N k_f^i \Phi_f^i(0) \exp[-k_f^i x], \quad (101)$$

whose general solution is

$$\Phi_{th}(x) = Ae^{-x/L} + Ce^{x/L} - \sum_{i=1}^N \frac{k_f^i \Phi_f^i(0)}{(k_f^i)^2 D - \mu_a} \exp[-k_f^i x], \quad (102)$$

where $L \equiv \sqrt{D/\mu_a}$. The constants A and C are then evaluated from the presumably known thermal neutron fluence incident at $x = 0$, and by setting Φ_{th} to zero at the outer surface of the shield, or, for thick shields, setting C equal to zero.

Instead of representing the fast-neutron fluence by a sum of exponentials as in (8.39), the shield could be divided into contiguous regions, with the fluence in each region represented by a single exponential, that is,

$$\Phi_f(x) = \Phi_f(x_j) \exp[-k_f^i(x - x_j)], \quad x_j < x < x_{j+1}. \quad (103)$$

Such a fit is easily performed by a series of straight-line fits to a plot of $\ln \Phi_f(x)$ versus x , and the relaxation constant k_f^j is obtained from

$$k_f^j = \frac{1}{x_j - x_{j+1}} \ln \left[\frac{\Phi_f(x_{j+1})}{\Phi_f(x_j)} \right]. \quad (104)$$

Once the exponential fit of the fast-neutron fluence is obtained for each region, the thermal neutron diffusion equation is solved in each region. The constants of integration are evaluated by requiring the solution and its first derivative to be continuous at the interfaces x_j or equal to specified values of the thermal neutron fluence at the shield surfaces. For preliminary analyses, it is often sufficient to fit the fast-neutron fluence by a single exponential over the whole shield volume. In **Table 20**, values for D and μ_a are presented for a few important shield materials, together with values of k_f for attenuation of fast neutrons.

5.6.2 Fermi Age Treatment for Thermal and Intermediate-Energy Neutrons

A refinement of the diffusion-theory procedure is to use Fermi age theory to correct for the migration of neutrons as they slow down to thermal energies (Blizard 1962). Age theory describes the slowing down of neutrons by a continuous energy-loss process which results in the same average energy loss as in the actual discrete energy losses from each scattering interaction. With this theory, neutrons are found to be distributed spatially in a Gaussian manner about the point at which they begin to slow down.

Table 20

Neutron properties of hydrogenous shield materials

Material	Density (g cm ⁻³)	k_f (cm ⁻¹) ^a	D (cm)	μ_a (cm)
Water	1.0	0.14	0.17	0.022
Ordinary concrete	2.35	0.085	0.65	0.0094
Barytes	3.50	0.125	0.44	0.019
Iron concrete	4.30	0.16	0.29	0.081

^aApproximate value for fast-neutron attenuations for a single exponential fit by (100). Actual fit values should be used whenever available.

Source: Glasstone and Sesonske (1963)

The number of fast neutrons reaching thermal energies per unit time at some point x inside the shield, $S_{th}(x)$, can be shown to be (Shultis and Faw 2000)

$$S_{th}(x) \simeq k_f \Phi_f(0) \exp[-k_f(x - k_f \tau_{th})], \quad (105)$$

where τ_{th} is the age to thermal energy. This result is valid for a shield whose thickness $T \gg \sqrt{\tau_{th}}$.

If the thermal neutrons are absorbed near the point at which they reach thermal energies, then under steady conditions the number absorbed, $\mu_a \Phi_{th}(x)$, must equal the number thermalized, $S_{th}(x)$. Thus, from (105),

$$\Phi_{th}(x) \simeq \frac{k_f}{\mu_a} \Phi_f(0) \exp[-k_f(x - k_f \tau_{th})] = \frac{k_f}{\mu_a} \Phi_f(x - k_f \tau_{th}). \quad (106)$$

This result implies that inside the shield the thermal neutron fluence is proportional to the fast-neutron fluence displaced toward the source by a *displacement distance* $k_f \tau_{th}$. The thermal neutron fluence inside a shield can thus be expected to parallel the fast-neutron fluence – a result usually observed.

5.6.3 Removal-Diffusion Techniques

Although diffusion theory can be used for initial estimates, more accurate techniques are often needed without the effort and expense of a full-scale multigroup transport calculation. Multigroup diffusion theory, which is considerably less expensive and complex to use than the transport theory, is remarkably successful at describing the slowing down and thermalization of neutrons in a reactor core. However, for describing neutrons deep within a shield, it has met with only limited success (Taylor 1951), although better accuracy has been obtained by introducing extraneous renormalization techniques to describe the penetration of the fast neutrons (Anderson and Shure 1960; Haffner 1968). That strict diffusion models should be of limited use to describe fast-neutron penetration, and subsequent thermalization is not surprising since diffusion theory requires both the differential scattering cross sections, and the angular fluence to be well described by first-order Legendre expansions. Such conditions usually hold in a reactor core where the neutron fluence is approximately isotropic; however, the fluence deep within a shield is determined by those very energetic neutrons which are highly penetrating and whose angular distribution is therefore highly anisotropic.

The penetrating fast neutrons are described very successfully by removal theory. The migration of the neutrons, once they are removed from the anisotropic fast group and begin to thermalize, is small compared to the distance traveled by the unremoved neutrons. Further, during thermalization, the fluence becomes more isotropic as more scatters occur. Consequently, one would expect multigroup diffusion theory to be applicable for the description of the slowing-down process and the subsequent diffusion at thermal energies. One approach to compute the buildup of low-energy neutrons inside a shield is to combine removal theory (to describe the penetration of fast neutrons) with multigroup diffusion theory (to describe the subsequent thermalization and thermal diffusion). This combination of removal and diffusion theory, in many formulations, has proved very successful.

Original Spinney Method

The first wedding of removal theory to diffusion theory was introduced by Spinney in 1958 (Avery et al. 1960). In the original formulation, the fast-source region, 0–18 MeV, is divided into 18 equal-width energy bands. The source neutrons in each band penetrate the shield in accordance with the removal theory. The density of removal collisions from all bands is then used as the source of neutrons in the first diffusion group. Explicitly, this diffusion source density at \mathbf{r} is given by

$$S_d(\mathbf{r}) = \sum_{i=1}^{18} \int_V \frac{S_v(\mathbf{r}') \chi_i \mu_{r,i} \exp(-\mu_{r,i} |\mathbf{r} - \mathbf{r}'|)}{4\pi |\mathbf{r}' - \mathbf{r}|^2} dV(\mathbf{r}'), \quad (107)$$

where $S_v(\mathbf{r}')$ is the production of source neutrons per unit volume at \mathbf{r}' in the source region, χ_i is the fraction of source neutrons in the i th removal band, and $\mu_{r,i}(\mathbf{r})$ is the removal coefficient for the i th band at position \mathbf{r} . The term $\mu_{r,i} |\mathbf{r} - \mathbf{r}'|$ is the total number of removal relaxation lengths between \mathbf{r} and \mathbf{r}' for a fast neutron in the i th band.

These removal neutrons are inserted as source neutrons into the top energy group of five energy groups, with the fifth group representing the thermal neutrons. The transfer of neutrons from one diffusion group to another diffusion group is determined by Fermi age theory (Lamarsh 1966), a continuous slowing-down model, and consequently neutrons can be transferred only to the energy group directly below. Thus, the diffusion group equations are written as

$$\nabla^2 \Phi_i(\mathbf{r}) - \frac{\mu_{a,i}}{D_i} \Phi_i(\mathbf{r}) - \frac{1}{\tau_i} \Phi_i(\mathbf{r}) = -\frac{S_i(\mathbf{r})}{D_i}, \quad (108)$$

where Φ_i is the fluence for group i , $\mu_{a,i}$ is the linear absorption coefficient for group i , D_i is the i th group diffusion coefficient, and τ_i is the square of the slowing-down length from group i to the next lower group $i + 1$, or equivalently, the Fermi age of neutrons starting from group i and slowing down to group $i + 1$ (for the thermal group, $\tau_i^{-1} = 0$).

The source term for the i th diffusion group is then given by

$$S_i(x) = \begin{cases} S_d(\mathbf{r}) & \text{from (107), } i = 1, \\ D_{i-1} \tau_{i-1}^{-1} \Phi_{i-1}(\mathbf{r}), & i > 1. \end{cases} \quad (109)$$

Improved Removal-Diffusion Methods

The original Spinney method, just described, was quite successful in predicting the low-energy neutron fluences in the concrete shields around early graphite reactors. However, to obtain better accuracy for a wider range of shield configurations, several obvious improvements could be made. First, more diffusion groups could be used to better describe the continuous slowing-down model implied by Fermi age theory. Second, neutrons should be allowed to transfer past intermediate diffusion groups in a single step to account for the possibility of large energy losses in inelastic scattering or elastic scattering from light nuclei. Third, more detail should be given for the removal of fast neutrons from the removal bands to the diffusion groups. Fast-neutron diffusion cannot be neglected altogether; and hence, the upper diffusion groups should overlap the same energy region spanned by the lower-energy removal bands. Further, when neutrons suffer a removal interaction, they should be allowed to enter any one of several diffusion groups, depending on the severity of the removal interaction. This improved description of the removed neutrons would give more information about the fast-neutron fluence, an important consideration for radiation damage studies.

Shortly after the introduction of the Spinney method, several variations of it were introduced which implement some or all of the improvements described above. Three such codes are RASH-E (Bendall 1962), MAC (Peterson 1962), and NRN (Hjärne 1964).

For thick shields with attenuation factors as low as 10^{-12} , this removal-diffusion method gives very accurate results even for layered shields, provided that penetration takes place mainly at the source energies (Peterson 1962). It is least accurate when significant attenuation occurs after diffusion (e.g., water followed by a thick iron shield). The greatest disadvantage of this method is the need to calculate many energy-group and removal-band constants (although considerably fewer than are needed for multigroup transport calculations). The removal-diffusion technique is a very powerful tool for the reactor designer, offering accuracies for many shield configurations comparable to those of the much more computationally expensive neutron transport methods.

With the advent of computing power undreamed of only decades ago, the use of removal-diffusion theory has waned and transport theory codes are now almost universally used in place of removal-diffusion codes. However, we include this section, not only for historical completeness, but for the insight it affords the analyst on how fast neutrons migrate through a shield.

5.7 Capture-Gamma-Photon Attenuation

Often, a significant contribution to the total dose at the surface of a shield is made by capture gamma photons produced deep within the shield as a result of neutron absorption. Another source of secondary photons arises from the inelastic scattering of fast neutrons. The resulting photons generally have much lower energies than the capture gamma photons (see [Table 7](#)) and are frequently ignored in the analysis of thick shields.

Most neutrons are not absorbed until they are thermalized, and consequently, one needs to consider only the absorption of thermal neutrons in most shield analyses. For this reason, it is important to calculate accurately the thermal neutron fluence $\Phi_{th}(\mathbf{r})$ in the shield. The volumetric source strength of capture photons per unit energy about E is, thus, given by (13), namely

$$S_y(\mathbf{r}, E) = \Phi_{th}(\mathbf{r})\mu_y(\mathbf{r})f(\mathbf{r}, E), \quad (110)$$

where $\mu_y(\mathbf{r})$ is the absorption coefficient at \mathbf{r} for thermal neutrons and $f(\mathbf{r}, E)$ is the number of photons produced in unit energy about E per thermal neutron absorption at \mathbf{r} . Although the capture-photon-energy distribution for any material is composed of a set of monoenergetic photons, a great many different energies can generally be expected as a result of multiple nuclear transitions following neutron capture and the usual presence of many different nuclear species in the shield material. Consequently, the capture-gamma-photon yield is usually “binned” into energy groups. Thus, the source strength for the i th energy group of width ΔE_i is

$$S_{yi}(\mathbf{r}) \equiv \int_{\Delta E_i} S(\mathbf{r}, E) dE = \Phi_{th}(\mathbf{r})\mu_y(\mathbf{r})f_i(\mathbf{r}), \quad (111)$$

where f_i is the number of photons produced in group i per thermal neutron absorbed at \mathbf{r} , averaged over all isotopes at \mathbf{r} , namely,

$$f_i(\mathbf{r}) = \frac{1}{\mu_y(\mathbf{r})} \sum_m \mu_y^m(\mathbf{r})f_i^m, \quad (112)$$

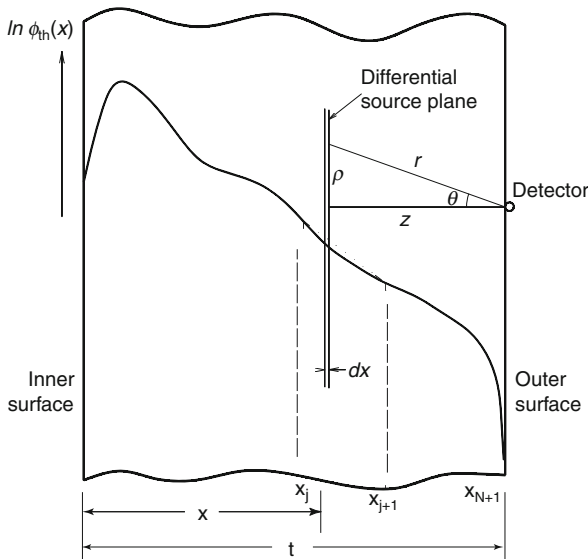
where the superscript m refers to the m th nuclide and summation is over all nuclear species. The quantity f_i^m is the number of capture photons emitted in group i arising from the absorption of a thermal neutron by the m th nuclide (see [Table 7](#)).

The calculation of the dose from capture gamma photons is based on the distributed source of (111). The calculational procedure is illustrated for an infinite slab shield in which the thermal-neutron fluence has been previously obtained (see [Fig. 28](#)). The slab is generally composed of laminates, that is, a series of adjacent homogenous regions. If the thermal-neutron fluence depends only on the distance into the slab (plane geometry), then with the technique involving the point kernel and point-source buildup factors, the dose or detector response $D(t)$ at the shield surface from capture-gamma photons in all G groups is

$$D(t) = \sum_{i=1}^G \mathcal{R}_i \int_0^t dx S_{\gamma i}(x) \int_0^\infty d\rho 2\pi\rho B_i(r) \frac{\exp[-\mu_i r]}{4\pi r^2}, \quad (113)$$

where \mathcal{R}_i is a fluence-to-dose conversion factor for photons in energy group i , B_i is a composite buildup factor for photons in group i traveling from the source to the detector through the various interposed laminates, and $\mu_i r$ is the total number of mean free paths for photons in group i between the source and the detector.

[Equation \(113\)](#) could be evaluated numerically for a given B_i and $S_{\gamma i}$; however, considerable simplification is possible if we assume functional forms for these two quantities that allow analytical evaluation of the integrals. In particular, the shield is subdivided into N contiguous regions such that each region is composed of a single material and over which the thermal-neutron fluence could be fit reasonably well by a single exponential (see [Fig. 28](#)). Thus, for



■ **Figure 28**

Profile of the thermal neutron fluence in a multilaminar shield showing the coordinate system used for calculation of the capture-gamma-photon dose at the shield surface

the j th region bounded by x_j and x_{j+1} , the thermal-neutron fluence is represented by

$$\Phi_{th}^j(x) \simeq \Phi^j \exp[-k^j x], \quad x_j < x < x_{j+1}, \quad (114)$$

where Φ^j and k^j are constants. Thus, the capture-gamma-source strength for the i th energy group is

$$S_{\gamma i}^j(x) = C_i^j \exp[-k^j x], \quad (115)$$

with $C_i^j \equiv \Phi^j \mu_{\gamma i}^j f_i^j$, where the superscript j refers to material properties in the j th region and the subscript i refers to the energy group of the photons. Equation (113) can then be evaluated analytically for the uncollided dose ($B = 1$), and for the collided dose, if the Berger-buildup factor approximation is used (Stevens and Trubey 1968).

5.8 Neutron Shielding with Concrete

Of all shielding materials, concrete is probably the most widely used because of its relatively low cost and the ease with which it can be cast into large and variously shaped shields. Concrete is prepared from a mixture, by weight, of about 13% cement, 7% water (including water in the aggregate), and 80% aggregate. Many different types of concrete can be prepared by varying the nature of the aggregate. For example, to improve photon-attenuation properties, scrap iron or iron ore may be incorporated into the sand-and-gravel aggregate.

The amount of hydrogen in concrete strongly influences its effectiveness for shielding against neutrons. Generally, the more water content, the less concrete is needed to thermalize and absorb incident-fast neutrons. Virtually, all the hydrogen in concrete is in the form of water, which is present not only as *fixed water* (i.e., water of hydration in the cement and aggregate) but also as *free water* in the pores of the concrete. At elevated temperatures, both may be lost, thereby greatly reducing the ability of the concrete to attenuate fast neutrons. Even at ambient temperatures, free water may be lost slowly over time by diffusion and evaporation. Typically, the free water is initially about 3% by weight of the concrete, and this water is lost by evaporation during curing of the concrete. Over a 20- to 30-year period at ambient temperatures, half the fixed water may be lost.

Neutron attenuation calculations for concrete, especially by the simplified methods presented in this chapter, are usually problematic, partly as a result of the variation in elemental compositions of different concretes, and partly because the hydrogen content of many concretes is only marginal for the application of removal theory. Neutron transport methods generally must be used if accurate results are desired.

5.8.1 Concrete Slab Shields

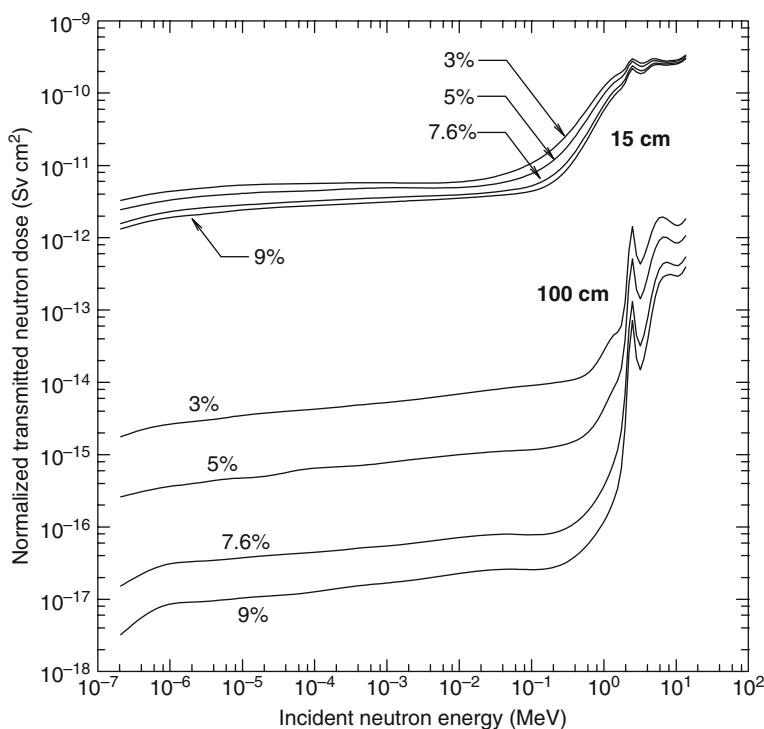
A particularly important shielding geometry is that of a plane slab of ordinary concrete on which a monoenergetic, broad, parallel beam of neutrons is normally incident. This problem has been studied in some detail (Alsmiller et al. 1969; Chilton 1971; Roussin and Schmidt 1971; Roussin et al. 1973; Wyckoff and Chilton 1973; Wang and Faw 1995). Extensive tables of dose transmission factors $\tau_i(t, E, \cos \theta)$ are available for neutrons ($i = n$) and the secondary photon

dose ($i = p$), for plane parallel beams of neutrons of energy E incident at the concrete slab (NBS Type 04), at an angle θ with respect to the slab normal (ANSI/ANS-2006). The transmitted dose rates for a neutron flux of Φ is then simply calculated as

$$D_i(t) = \Phi \cos \theta \tau_i(t, E, \cos \theta), \quad i = n, p. \quad (116)$$

Effect of Water Content

If the proportion of water is changed in concrete, the concrete's attenuation ability also changes, especially for thicker shields. An example of the effect of water content in ordinary concrete (NBS Type 04 of [Table 24](#)) is shown in [Fig. 29](#). Detailed data must be obtained from the literature (Chilton 1971); but as an example, it can be shown that a reduction from 5.5% water to 4.5% water requires that the prescribed dose-equivalent values be multiplied by a factor of about 1.6 for incident neutrons in the energy range 1–15 MeV and for a shield thickness of about 400 g cm^{-2} . A reduction to 3.5% requires a multiplicative factor of about 2.6 under these circumstances; and a reduction to 2.5% implies a factor of about 4.1 (NCRP 1977).



■ Figure 29

Transmitted dose equivalent per unit incident fluence for neutrons, normally incident on slabs of ordinary concrete (NBS Type 04), with two thicknesses and four water contents (by weight). Response functions used are for the deep dose index (PAR) as specified by the ICRP (1987). Data courtesy of X. Wang, Kansas State University

Effect of Slant Incidence

Data are also available for neutron penetration through concrete slabs under slant incidence conditions (Chilton 1971; Wang and Faw 1995; ANS/ANSI 2006). In [▶ Fig. 30](#), the transmitted phantom-related dose equivalent for several slab thicknesses and incident angles is shown for a slab composed of a 5.5%-water calcareous concrete. These dose-equivalent results, which also included the capture-photon contribution, are normalized to a unit incident flow on the slab surface; that is, to an incident beam that irradiates each square centimeter of the surface with one neutron regardless of the beam direction. The transmitted dose equivalent when normalized this way is called the *transmission factor*. In ANSI/ANS-6.4-2006, tables are provided for the neutron and secondary-photon transmission factors for several thicknesses of concrete slabs uniformly illuminated by monoenergetic and monodirectional neutrons. Data for different concretes, incident energies, and incident directions can be found in the literature cited.

The transmission factor for a given slab thickness is seen from [▶ Fig. 30](#), to decrease by a multiplicative factor of between only 2–5 as the incident beam changes from normal incidence to a grazing incidence of 75° (from the normal), for a wide range of incident neutron energies. This variation of the transmission factor for neutrons, while appreciable, is not nearly as severe as it is for photons (see [▶ Table 14](#)).

Effect of the Aggregate

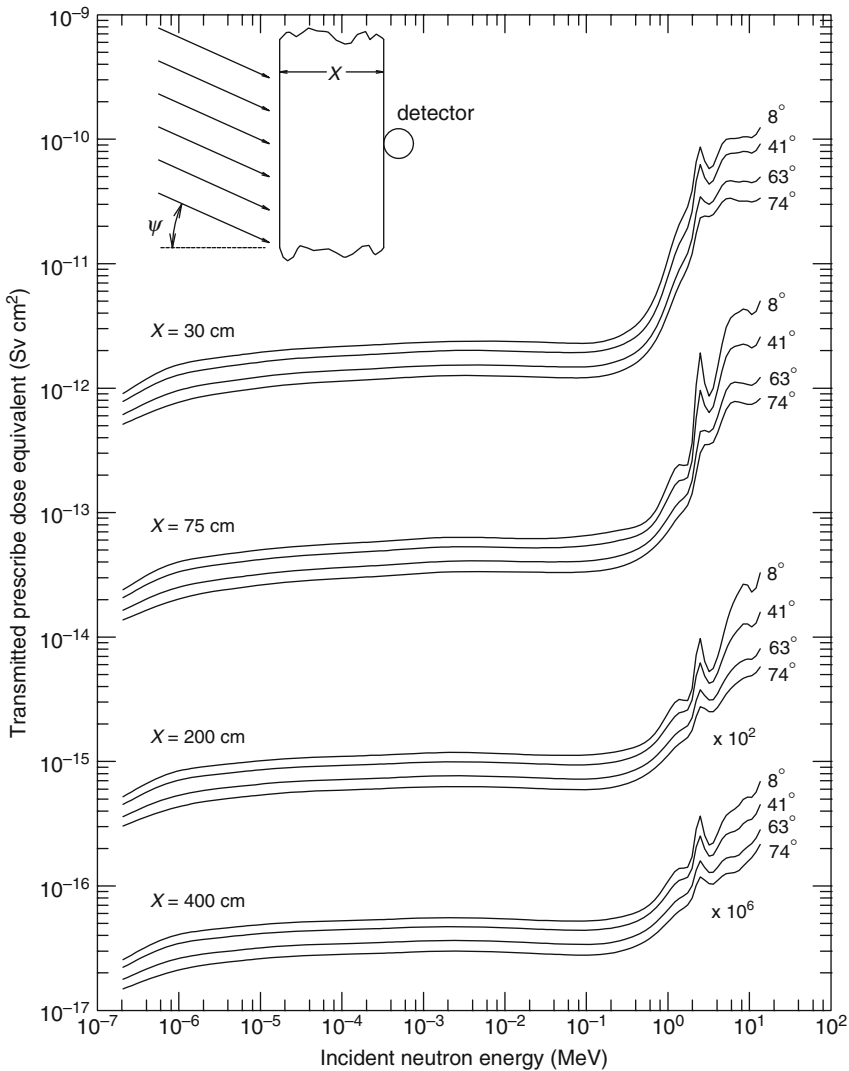
Aside from water variation, the other major change possible in the composition of ordinary concrete is the use of quartz-based sand and aggregate (SiO_2), instead of limestone in ordinary concrete. This siliceous type of concrete allows more dose-equivalent penetration than does the same mass thickness of calcareous concrete with the same water content; in general, it has neutron shielding properties about the same as calcareous concrete with about 2% less water (i.e., as if a 5.5% water content had been reduced to 3.5%) (Chilton 1971; Wyckoff and Chilton 1973).

It should be noted that none of the data presented in this section apply to “heavy concretes,” that is, to concretes with minerals containing high- Z elements included as part of the aggregate, nor to any other concrete of a composition deviating markedly from those proportions considered “ordinary.”

Effect of the Fluence-to-Dose Conversion Factor

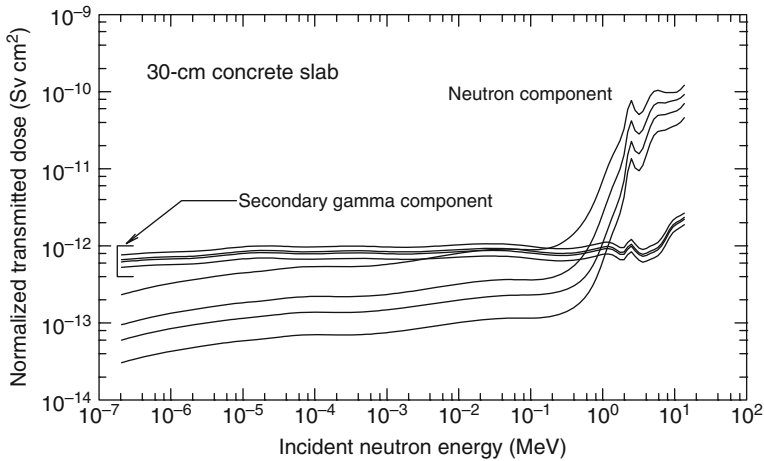
Finally, the dose units used to measure the transmitted dose can have an appreciable effect on the transmission factor, far more so for neutrons than for photons. In [▶ Fig. 31](#), the neutron and secondary-gamma-ray transmission factors are shown for four response functions. It is seen that the transmitted secondary-photon dose is insensitive to the type of response function when compared with the neutron dose. For this reason, it is very important to pay careful attention to the dose-conversion coefficient used when trying to apply results found in the literature to a particular neutron shielding problem.

One final comment on the data presented in this section is appropriate as a cautionary statement. The data presented here are based on results of theoretical calculations. No experimental verification is available. Under such circumstances, the data should be used with some caution, especially for the greater thicknesses, and a factor of safety of at least two in dose is advised.



■ Figure 30

Transmitted deep dose equivalent (including the capture-gamma-photon contribution) through a concrete slab illuminated obliquely at four angles as a function of the incident neutron energy. The transmitted dose is normalized to a unit flow on the slab surface. Note that the curves at $x = 200$ cm and $x = 400$ cm have been multiplied by factors of 10^2 and 10^6 , respectively. Concrete composition (in 10^{21} atoms cm^{-3}): H, 8.50; C, 20.20; O, 35.50; Mg, 1.86; Al, 0.60; Si, 1.70; Ca, 11.30; and Fe, 0.19; density is 2.31 g cm^{-3} and water (percent by weight) is 5.5%. From data of Chilton (1971)



■ Figure 31

Transmitted dose per unit incident fluence for neutrons normally incident on a 30-cm slab of ordinary concrete (NBS Type 03) for four different dose units. The four response functions (from top to bottom) are for the NCRP-38 phantom (ANS/ANSI 1977), and the ICRP-51 anthropomorphic phantom for AP, PA, and LAT irradiation conditions (ICRP 1987). Data courtesy of X. Wang, Kansas State University

6 The Albedo Method

The calculation of how radiation incident on a surface is reemitted through the surface toward some point of interest is a frequently encountered problem in radiation shielding. Transport techniques are generally required for detailed estimation of reflected doses. But under certain circumstances, a simplified approach based on the albedo concept can be used with great effect. These conditions are (1) that the displacement on the surface between the entrance and exit of the radiation is very small when compared with the problem dimensions, (2) that the reflecting medium is about two or more mean free paths thick, and (3) that scattering between the radiation source and surface and between the surface and point of interest is insignificant.

Of course, reflection does not take place exactly at the point of incidence, but results from scattering by nuclei or electrons within the medium, with perhaps very many interactions taking place before an incident particle emerges or is “reflected” from the surface, as indicated in ► Fig. 32. Nevertheless, in radiation shielding calculations in which the character of the incident radiation does not change greatly over the surface in distances of about one mean free path, as measured in the reflecting medium, a reasonably accurate assumption can be made that the particles emerging from an incremental area result directly from those incident on that same area. Similarly, it has been found that for a reflecting medium thicker than about two mean free paths, it is an excellent approximation to treat the medium as a half-space. For discussion of these approximations and for more advanced treatments, the reader is referred to Leimdorfer (1968) and Selph (1973). The use of albedo techniques is central to many radiation-streaming codes and has been widely used as an alternative to much more expensive transport calculations.

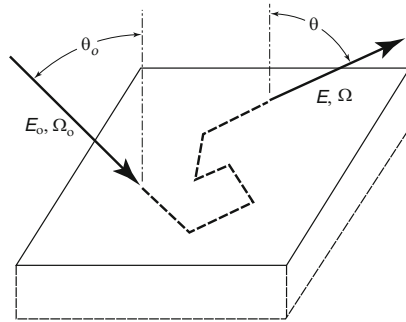


Figure 32
Particle reflection from a scattering medium

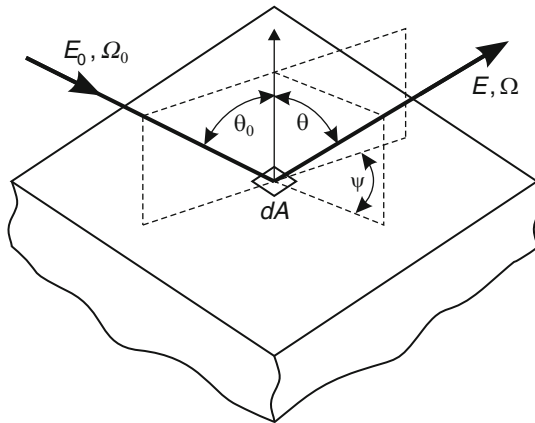


Figure 33
Angular and energy relationships in the albedo formulation

6.1 Differential Number Albedo

Radiation reflection may be described in terms of the geometry shown in Fig. 33. Suppose that a broad beam of incident particles, all of energy E_0 and traveling in the same direction, strike area dA in the reflecting surface at angle θ_0 measured from the normal to the surface. If Φ_0 is the fluence of the incident particles and J_{n0} is the corresponding flow, the number of incident particles striking dA is $dA J_{n0} = dA \Phi_0 \cos \theta_0$. Suppose that the energy spectrum of the angular distribution of the fluence of reflected particles emerging from the surface with energy E and direction characterized by angles θ and ψ is $\Phi_r(E, \theta, \psi)$ and the corresponding differential flow is $J_{nr}(E, \theta, \psi)$. The number of particles emerging from dA with energies in dE about E and with directions in solid angle $d\Omega$ about direction (θ, ψ) is $dA J_{nr}(E, \theta, \psi) dE d\Omega = dA \cos \theta \Phi_r(E, \theta, \psi) dE d\Omega$. The *number albedo* $\alpha(E_0, \theta_0; E, \theta, \psi)$ is defined as

$$\alpha(E_0, \theta_0; E, \theta, \psi) \equiv \frac{J_{nr}(E, \theta, \psi)}{J_{n0}} = \frac{\cos \theta \Phi_r(E, \theta, \psi)}{\cos \theta_0 \Phi_0}. \quad (117)$$

6.2 Integrals of Albedo Functions

Occasionally of interest as reference albedos or in verification of particle conservation in transport calculations are the following integrals over all possible energies and all possible directions:

$$\alpha_N(E_o, \theta_o; \theta, \psi) \equiv \int_0^{E_o} dE \alpha(E_o, \theta_o; E, \theta, \psi) \quad (118)$$

and


$$A_N(E_o, \theta_o) \equiv \int_0^{2\pi} d\psi \int_0^1 d(\cos \theta) \alpha_N(E_o, \theta_o; \theta, \psi). \quad (119)$$

Of much more interest and utility is the *differential dose albedo*, defined as the ratio of the reflected flow, in dose units, to the incident flow, also in dose units. If $\mathcal{R}(E)$ is the dose-conversion coefficient, then

$$\alpha_D(E_o, \theta_o; \theta, \psi) \equiv \frac{\int_0^{E_o} dE \mathcal{R}(E) J_{nr}}{\mathcal{R}(E_o) J_{no}} = \int_0^{E_o} dE \frac{\mathcal{R}(E)}{\mathcal{R}(E_o)} \alpha(E_o, \theta_o; E, \theta, \psi). \quad (120)$$

It is important to recognize that dose-conversion coefficients affect $\alpha_D(E_o, \theta_o; \theta, \psi)$ only in the *ratio* $\mathcal{R}(E)/\mathcal{R}(E_o)$. For this reason, the photon dose albedo is not strongly dependent on the nature of the response. Photon albedos are commonly evaluated for exposure as the dose, but used in estimation of dose-equivalent or even effective dose. However, greater care must be taken with neutron albedos because $\mathcal{R}(E)/\mathcal{R}(E_o)$ can be quite different for different conversion coefficients.

6.3 Application of the Albedo Method

Refer to  [Fig. 33](#) and suppose that a point isotropic and monoenergetic photon source of strength S_p is located at distance r_1 from area dA along incident direction Ω_o and that a dose point is located distance r_2 from area dA along emergent direction Ω . Suppose that an isotropic radiation detector at the dose point is a vanishingly small sphere with cross-sectional area δ . At area dA , the flow of incident photons is $J_{no} = (S_p/4\pi r_1^2) \cos \theta_o$. Since the solid angle subtended by the detector at dA is δ/r_2^2 , the number of photons emerging from dA with energies in dE and with directions intercepting the detector is $J_{nr}(E, \theta, \psi) dA (\delta/r_2^2)$. This quantity, divided by the cross-sectional area of the spherical detector, is just that part of the energy spectrum of the fluence at the detector attributable to reflection of photons from area dA , namely,

$$d\Phi(E) dE = J_{nr}(E, \theta, \psi) \frac{dA}{r_2^2} dE = J_{no} \alpha(E_o, \theta_o; E, \theta, \psi) \frac{dA}{r_2^2} dE \quad (121)$$

or

$$d\Phi(E) dE = \frac{S_p \cos \theta_o}{4\pi r_1^2} \alpha(E_o, \theta_o; E, \theta, \psi) \frac{dA}{r_2^2} dE. \quad (122)$$

That part dD_r of the dose D_r owing to reflection of photons from dA is $\int dE \mathcal{R}(E) d\Phi(E)$, namely,

$$dD_r = \frac{S_p \cos \theta_o}{4\pi r_1^2} \frac{dA}{r_2^2} \int_0^{E_o} dE \mathcal{R}(E) \alpha(E_o, \theta_o; E, \theta, \psi) \quad (123)$$

or

$$dD_r = \left[\frac{S_p \mathcal{R}(E_o)}{4\pi r_1^2} \right] \frac{dA \cos \theta_o}{r_2^2} \alpha_D(E_o, \theta_o; \theta, \psi). \quad (124)$$

If the source were not isotropic but had an angular distribution $S(\Omega)$, then

$$dD_r = \left[\frac{S(\theta_o) \mathcal{R}(E_o)}{r_1^2} \right] \frac{dA \cos \theta_o}{r_2^2} \alpha_D(E_o, \theta_o; \theta, \psi), \quad (125)$$

in which $S(\theta_o)$ denotes symbolically the source intensity per steradian, evaluated at the direction from the source to reflecting area dA . Note that the bracketed term on the right side of either of the two previous equations is just the dose D_o at dA due to incident photons. Thus,

$$dD_r = D_o \alpha_D(E_o, \theta_o; \theta, \psi) \frac{dA \cos \theta_o}{r_2^2}. \quad (126)$$

Determination of the total reflected dose D_r requires an integration over the area of the reflecting surface. In doing such an integration, it must be remembered that as the reflecting location on the surface changes, all the variables θ_o , θ , ψ , r_1 , and r_2 change as well.

6.4 Albedo Approximations

Key to the albedo technique is the availability of either a large set of albedo data or, preferably, an empirical formula that approximates the albedo over the range of source energies and incident and exit radiation directions involved in a particular problem. Many albedo approximations have been proposed over the past four decades. However, many of these must be used with caution because they are based on limited energy-angular ranges, a single reflecting material, old cross section data, and, for neutron albedos, obsolete fluence-to-dose conversion factors.

6.4.1 Photon Albedos

A two-parameter approximation for the photon-dose albedo was devised by Chilton and Huddleston (1963), later extended by Chilton, Davisson, and Beach (1965), in the following form:

$$\alpha_D(E_o, \theta_o; \theta, \psi) \approx \frac{C(E_o) \times 10^{26} [\sigma_{ce}(E_o, \theta_s)/Z] + C'(E_o)}{1 + \cos \theta_o / \cos \theta}, \quad (127)$$

in which $C(E_o)$ and $C'(E_o)$ are empirical parameters that depend implicitly on the composition of the reflecting medium. Here, θ_s is the scattering angle, whose cosine is

$$\cos \theta_s = \sin \theta_o \sin \theta \cos \psi - \cos \theta_o \cos \theta \quad (128)$$

and $\sigma_{ce}(E_o, \theta_s)$ is the Klein–Nishina *energy scattering* cross section

$$\sigma_{ce}(E, \theta_s) = Zr_e^2 q^2 [1 + q^2 - q(1 - \cos^2 \theta_s)]/2, \quad (129)$$

where $q = E/E_o$, r_e is the classical electron radius, and Z is the atomic number of the medium. The approximation of (127) was fit to data obtained by Monte Carlo calculations using modern dose units to produce the albedo parameters shown in ► Table 21.

Chilton (1967) found that albedo data for concrete could be fit even better by the formula

$$\alpha_D(E_o, \theta_o; \theta, \psi) = F(E_o, \theta_o; \theta, \psi) \frac{C(E_o) \times 10^{26} [\sigma_{ce}(E_o, \theta_s)/Z] + C'(E_o)}{1 + (\cos \theta_o / \cos \theta)(1 + 2E_o \text{ vers } \theta_s)^{1/2}}, \quad (130)$$

in which the factor F is a purely empirical multiplier, given by

$$F(E_o, \theta_o; \theta, \psi) = A_1(E_o) + A_2(E_o) \text{ vers}^2 \theta_o + A_3(E_o) \text{ vers}^2 \theta + A_4(E_o) \text{ vers}^2 \theta_o \text{ vers}^2 \theta + A_5(E_o) \text{ vers } \theta_o \text{ vers } \theta \text{ vers } \psi, \quad (131)$$

in which $\text{vers } \theta = 1 - \cos \theta$. The seven parameters in this approximation are tabulated by Shultis and Faw (2000).

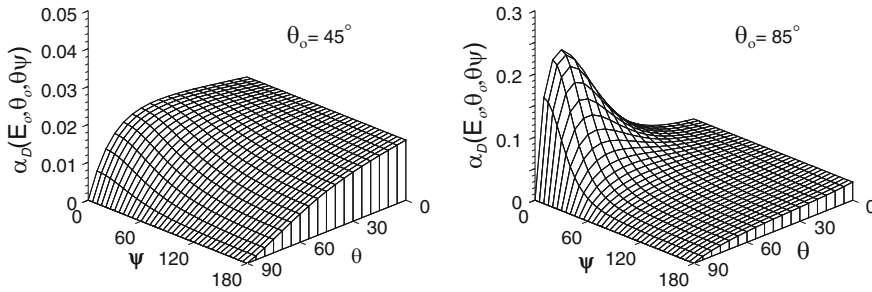
It should be emphasized that, to estimate an albedo for a photon energy between the tabulation energies, the interpolation should *not* be made with interpolated values of the parameters; rather, an interpolation of calculated albedos obtained with coefficients at bracketing tabulated energies should be used. Examples of the dose albedo from (130) are shown in ► Fig. 34.

■ Table 21

Parameters for the two-term Chilton–Huddleston approximation, (127), for the 10-mm H*(10) ambient-dose-equivalent albedo

Energy (MeV)	Water		Concrete		Iron		Lead	
	$10^3 C$	$10^3 C'$	$10^3 C$	$10^3 C'$	$10^3 C$	$10^3 C'$	$10^3 C$	$10^3 C'$
0.10	3.83956	156.682	15.0806	53.5702	6.01974	6.30725	-0.99254	71.4260
0.20	12.8933	95.1294	19.5317	56.3968	22.8818	4.52419	2.54139	13.6862
0.40	26.9251	49.4120	31.0515	34.8623	34.9866	10.5355	12.3140	-4.16344
0.60	36.2690	35.5403	38.5117	26.5358	44.7663	10.5212	23.0250	-6.35561
0.80	44.6428	27.7803	46.5630	20.9768	52.9704	9.63214	32.4332	-6.21926
1.00	52.7863	22.5602	54.4830	17.3114	55.7093	8.65893	41.5937	-5.71107
1.25	61.9729	18.5551	65.3668	14.2054	70.5985	7.65120	51.2948	-4.89882
2.00	86.5642	12.6338	86.5215	10.6027	91.4505	7.81777	72.0777	0.65892
4.00	137.182	8.63979	134.941	8.84981	131.920	10.5014	93.2920	7.47707
6.00	172.511	7.47389	162.904	8.47375	148.934	11.5784	107.474	8.80086
8.00	195.014	6.97739	178.589	8.36158	170.405	11.9144	125.587	9.07966
10.00	218.439	6.58747	196.888	8.15070	173.252	11.9926	139.207	9.03810

Source: Data courtesy of R.C. Brockhoff, Nuclear Engineering Department, Kansas State University



■ **Figure 34**
Ambient-dose-equivalent albedos for reflection of 1.25-MeV photons from concrete

6.4.2 Neutron Albedos

There is much data in the literature for neutron albedos and for the associated secondary-photon doses. For a review of these earlier studies, see Shultis and Faw (2000) and Brockhoff and Shultis (2007). Unlike compilations or formulas for albedos for monoenergetic incident photons, it is difficult to interpolate similar neutron albedos because of the many resonances in the neutron cross sections. To account for the usual continuous distribution of fast or intermediate-energy neutrons, it is preferable to obtain albedos for incident neutrons in various contiguous energy bins. However, many early albedo studies are for monoenergetic sources, and hence, are of limited practical utility. Moreover, most neutron-albedo approximating formulas are based on the very old neutron-interaction data, on only a few incident directions, and are available only for a single reflecting material. With rare exception, neutron-albedo studies consider only concrete, the material most frequently subject to reflection analyses.

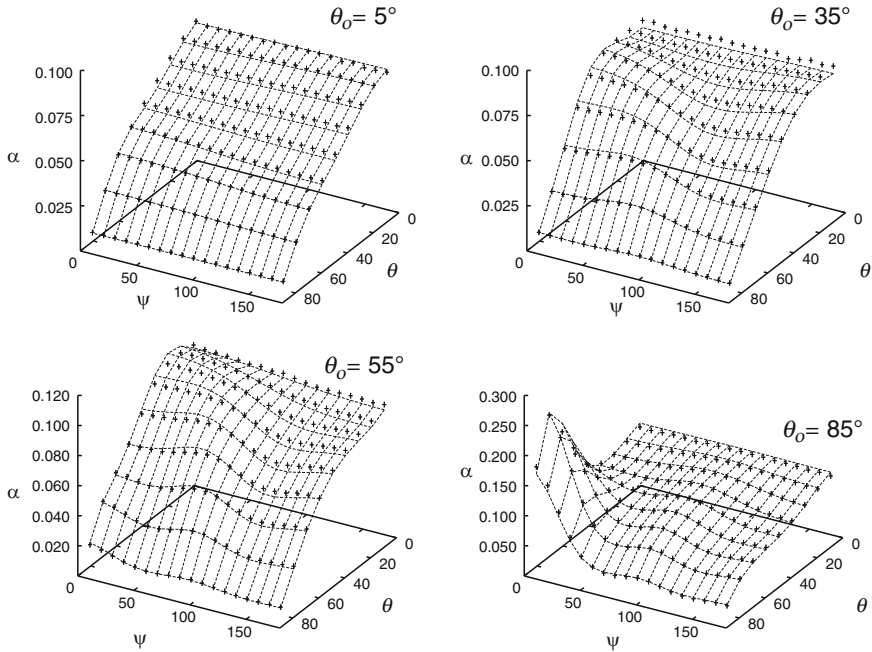
Recently, neutron dose albedos have been calculated for reflection from concrete, water, iron, and lead (Brockhoff and Shultis 2007). From these data, a variety of approximating formulas were adjusted to the calculated data. The formula that best fit the data for all materials and energy groups was

$$\alpha_D(\Delta E_o, \theta_o; \theta, \psi) = \frac{H(\kappa_1, \cos \theta_o)H(\kappa_2, \cos \theta)}{1 + K_1(E_o, \theta_o; \theta) / \cos \theta} \sum_{i=0}^N B_i P_i(\cos \theta_s), \quad (132)$$

where

$$K_1(E_o, \theta_o; \theta) = \sum_{i=0}^2 \cos^i \theta \sum_{j=0}^2 A_{ij} \cos \theta_o^j. \quad (133)$$

The number of fitting parameters is $N+12$ [$\kappa_1, \kappa_2, 9 A_{ij}$, and $(N+1) B_i$]. The number of terms used in the Legendre expansion, $N+1$, determines the accuracy of the approximation. For most reflecting media and neutron energies, the use of a 9-term expansion results in fits with a maximum deviation of less than 10%. However, for extreme cases such as 8–10 MeV neutrons incident on concrete, water, iron, and lead, an $N = 13$ (24 parameters) results in maximum deviations of 6.95, 9.08, 8.97, and 8.13% for the four reflecting media, respectively. Besides approximating the albedo for all the discrete fast-energy groups, the 24-parameter formula also worked well for thermal neutrons, ^{252}Cf fission neutrons, and 14-MeV neutrons. Tabulations of the 24 parameters are provided by Brockhoff and Shultis (2007) and by ANS/ANSI (2006). A sample comparison between the calculated albedo data and approximation is shown in ► [Fig. 35](#).



■ Figure 35

Neutron differential ambient-dose equivalent albedo $\alpha_D(E_o, \theta_o; \theta, \psi)$ for 6–8 MeV neutrons, incident on a slab of concrete for $\theta_o = 5, 35, 55,$ and 85 degrees. Comparison of MCNP results (crosses) and the results obtained using the approximation of (132) (surface)

Secondary-Photon Albedos


The secondary albedo arises from the production of inelastic and capture gamma rays that are radiated from the reflecting surface. In general, the secondary-photon albedo is independent of the azimuthal angle as a consequence of the isotropic emission of secondary gamma rays. Also of note is that the magnitude of the secondary-photon dose albedo is usually considerably less than that of the neutron dose albedo and, consequently, a high accuracy for the secondary-photon albedo is generally not needed.

Maerker and Muckenthaler provided detailed calculations for thermal neutrons incident on concrete, and proposed a relation to approximate the secondary-photon albedo, namely, (Maerker and Muckenthaler 1965)

$$\alpha_{D_2}^{(n,\gamma)}(\theta_o, \theta) = \cos^{A_1}(\theta) [A_2 + A_3 \cos(\theta_o) + A_4 \cos^2(\theta_o)] A_5, \quad (134)$$

where the parameters $A_1, A_2, A_3, A_4,$ and A_5 are functions of the reflecting media and the energy of the incident neutrons. This approximation was used by Shultis and Brockhoff (2007) to approximate their calculated secondary-photon albedos.

This approximation is not as accurate as the approximations presented for the neutron albedo. Use of this approximation can result in deviations in excess of 20% in some cases. Therefore, for problems in which the secondary-photon albedo needs to be calculated accurately over a small range of reflected directions, (134) should be used carefully. For most problems,

the secondary-photon albedo is usually small in comparison with the neutron albedo; and the use of this approximation should yield acceptable results. A sample comparison between the calculated albedo data and approximation is shown in  Fig. 36.

7 Skyshine

In many facilities with intense localized sources of radiation, the shielding against radiation that is directed skyward is usually far less than that for the radiation emitted laterally. However, the radiation emitted vertically into the air undergoes interactions and some secondary radiation is reflected back to the ground, often at distances far from the source. This atmospherically reflected radiation, referred to as *skyshine*, is of concern both to workers at a facility and to the general population outside the facility site.

A rigorous treatment of the skyshine problem requires the use of computationally expensive methods based on multidimensional transport theory. Alternatively, several approximate procedures have been developed for both gamma-photon and neutron-skyshine sources. See Shultis et al. (1991) for a review. This section summarizes one approximate method, which has been found useful for bare or shielded gamma-ray and neutron skyshine sources. This method, termed the *integral line-beam skyshine method*, is based on the availability of a *line-beam response function* (LBRF) $\mathcal{R}(E, \Phi, x)$ that gives the dose at a distance x from a point source

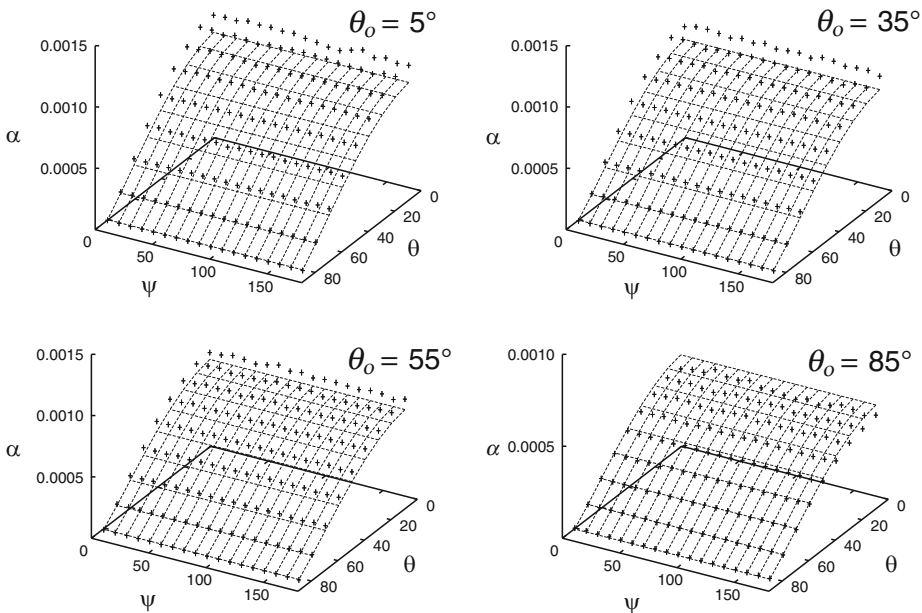


 **Figure 36**

The differential secondary-photon effective-dose-equivalent (AP) albedo $\alpha_D(E_o, \theta_o; \theta, \psi)$ for 1–2 MeV monidirectional neutrons, incident on a slab of concrete for $\theta_o = 5, 35, 55,$ and 85 degrees. Comparison of MCNP results (crosses) and the results obtained using the approximation of (134) (surface)

emitting a particle (neutron or photon) of energy E , at an angle Φ from the source-to-detector axis into an infinite air medium.

To obtain the skyshine dose $D(d)$ at a distance d from a bare collimated source, the line-beam response function, weighted by the energy and angular distribution of the source, is integrated over all source energies and emission directions. Thus, if the collimated source emits $S(E, \Omega)$ particles, the skyshine dose is

$$D(d) = \int_0^\infty dE \int_{\Omega_s} d\Omega S(E, \Omega) \mathcal{R}(E, \Phi, d), \quad (135)$$

where the angular integration is over all emission directions allowed by the source collimation Ω_s . Here Φ is a function of the emission direction Ω . To obtain this result, it has been assumed that the presence of an air-ground interface can be neglected by replacing the ground by an infinite air medium. The effect of the ground interface on the skyshine radiation, except at positions very near to a broadly collimated source, has been found to be small. At positions near the source (near-field), the ground augments slightly the dose, although at large distances from the source; it depresses slightly the dose when compared with results obtained with the infinite-air approximation. To account for the generally small air-ground interface effect, empirical *ground correction factors* are available to correct the infinite-air result of (135) (Kahn 1994; Gui, Shultis and Faw 1997a and 1997b).

Implicit in the integral line-beam approach is the assumption that the radiation source can be treated as a point source and that the source containment structure has a negligible perturbation on the skyshine radiation field, that is, once source radiation enters the atmosphere, it does not interact again with the source structure. With this assumption, the energy and angular distribution of source radiation penetrating any overhead source shield or escaping from the containment structure is independent of the subsequent transport of the radiation through the air to the detector. In most skyshine calculations at distances far from the source, this is true; however, for detectors near the source, this second assumption is not always valid.

7.1 Approximations for the LBRF

The LBRF for both photons, neutrons, and secondary photons from neutron interactions in the air can all be approximated over a large range of x by the following three-parameter empirical formula, for a fixed value of E and Φ (Lampley et al. 1988):

$$\mathcal{R}(x, E, \Phi) = \kappa E(\rho/\rho_o)^2 [\rho x/\rho_o]^b \exp[a - (c\rho x/\rho_o)], \quad (136)$$

in which ρ is the air density in the same units as the reference density $\rho_o = 0.0012 \text{ g cm}^{-3}$ and κ is a constant that depends on the dose unit used. The parameters a , b , and c depend on the neutron or photon source energy E (in MeV), the emission direction Φ , and dose unit employed. Various compilations of the parameters a , b , and c have been produced by fitting (136) to results of Monte Carlo calculations of the LBRF.

A double linear interpolation scheme can be used to obtain the logarithm of $\mathcal{R}(E, \Phi, x)$ for any E or Φ in terms of values at the discrete tabulated energies and angles. In this way, the approximate line-beam response function can be rendered completely continuous in the x , E , and Φ variables. With these approximate LBRFs, the skyshine dose is readily evaluated from (135) using standard numerical integration.

7.1.1 Photon LBRF Approximation

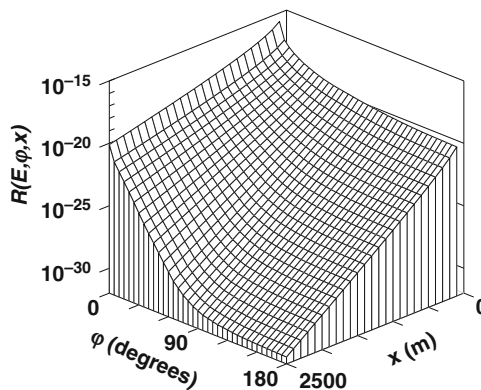
Tables of the parameters for (136), suitable for estimating the LBRF $\mathcal{R}(E, \Phi, x)$, were provided first by Lampley et al. (1988) and later, in more modern dosimetric units, by Shultis and Faw (1994) for a source-to-detector range of about $1 \text{ m} < x < 3000 \text{ m}$ for 12 discrete energies from 0.04 to 10 MeV and for 20 discrete angles Φ are available. Brockhoff et al. (1996) later extended to the energy range from 20 to 100 MeV. These later compilations are available from the Radiation Safety Information Computational Center (RSICC) as part of the Data Library Collection DLC-188/SKYDATA-KSU. \blacktriangleright Figure 37 illustrates $\mathcal{R}(E, \Phi, x)$ for 6.13-MeV photons. Such high-energy photons arise from decay of ^{16}N and are important in the design of water-cooled nuclear power plants.

7.1.2 Neutron LBRF Approximation

The neutron and secondary-photon LBRFs have been evaluated with the MCNP code at 14 discrete energies from 0.01 to 14 MeV, at 18 emission angles from 1 to 170 degrees, and at 24 source-to-detector distances from 10 to 2450 m (Gui et al. 1997a). Equation (136) was fit to these data and a compilation of the fitting parameters for modern neutron dosimetry units produced and is also part of the RSICC Data Library Collection DLC-188/SKYDATA-KSU. Examples of these approximate neutron LBRFs are shown in \blacktriangleright Fig. 38.

7.2 Open Silo Example

The general result of (135) can be reduced to explicit forms suitable for calculation for special geometries and source characteristics (Shultis et al. 1991). As an example, consider the case in which an isotropic, monoenergetic point source [(i.e., $S(E', \Omega) = S_p \delta(E' - E)/4\pi$), is located on the vertical axis of a cylindrical-shell shield (silo) of inner radius r (see \blacktriangleright Fig. 39). The wall of the silo is assumed to be *black* (i.e., no source radiation penetrates it). The source is distance h_s



\blacksquare Figure 37

Line-beam response function for 6.13-MeV photons in the atmosphere

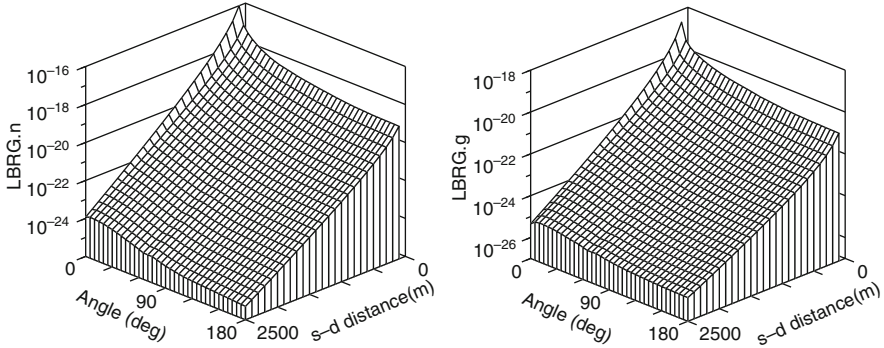


Figure 38

The neutron line-beam response functions (Sv/source-neutron) for a 14-MeV source in an infinite air medium. The left figure shows the neutron dose as a function of the source-to-detector distance and the angle of neutron emission with respect to the source–detector axis. The right figure shows the dose from secondary photons

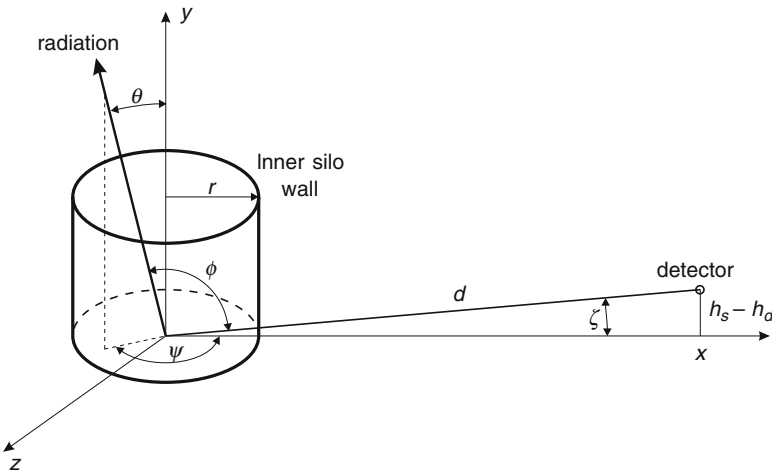


Figure 39

Geometry for skyshine analysis of an isotropic point source in an open silo

below the horizontal top of the silo which collimates the emergent radiation into a cone with a polar angle θ_{max} measured from the vertical axis and defined by

$$\omega_o \equiv \cos \theta_{max} = 1 / \sqrt{1 + r^2 / h_s^2}. \tag{137}$$

A detector (dose point) is located in air at radial distance x from the silo axis and at distance h_d below the silo top. If h_d is above the top of the silo wall, this distance is negative. The distance

from the source to the detector is

$$d = \sqrt{x^2 + (h_s - h_d)^2} \quad (138)$$

and the angle ζ between the horizontal and the source-to-detector axis is

$$\zeta = \tan^{-1}[(h_s - h_d)/x]. \quad (139)$$

Consider a particle emitted at polar angle θ , measured from the silo axis, and at azimuthal angle ψ , measured from the vertical plane through the source and detector. The cosine of the angle of emission Φ between the photon direction and the source–detector axis is the dot product of the unit vector in the emission direction and a unit vector along the source–detector axis, namely,

$$\cos \Phi = \sin \theta \cos \psi \cos \zeta + \cos \theta \sin \zeta. \quad (140)$$

For this unshielded-silo, monoenergetic-source problem, the skyshine dose at the detector is given by (135), which, upon using the azimuthal symmetry of the geometry and the monoenergetic nature of the source, reduces to

$$D(d) = \frac{S_p}{2\pi} \int_0^\pi d\psi \int_{\omega_o}^1 d\omega \mathcal{R}(E, \Phi, d). \quad (141)$$

This double integral is readily evaluated using standard numerical integration techniques.

7.3 Shielded Skyshine Sources

Most skyshine sources have some shielding over them, for example, a building roof, that reduces the amount of radiation escaping into the atmosphere. Such shielding causes some of the source radiation penetrating the shield to be degraded in energy and angularly redirected before entering the atmosphere. The effect of an overhead shield on the skyshine dose far from the source can be accurately treated by a two-step hybrid method (Shultis et al. 1991; Stedry et al. 1996; Shultis 2000). First, a transport calculation is performed to determine the energy and angular distribution of the radiation penetrating the shield, and then, with this distribution as an effective point, bare, skyshine source, the integral line-beam method is used to evaluate the skyshine dose at distances far from the source.

Although the two-step hybrid method can give very accurate results (e.g., Hertel et al. (2005)) the shield transport calculation requires considerable effort when compared with the subsequent integral line-beam calculation. A simpler, albeit less-accurate method to account for an overhead shield for photon skyshine is to assume that source photons are exponentially attenuated and that the buildup of secondary radiation can be estimated by an infinite-medium buildup factor for the source-energy photons (Shultis et al. 1991). In this simplified method, the energy and angular redistribution of the photons scattered in the shield is ignored (i.e., the scattered photons are assumed to emerge from the shield with the same energy and direction as the uncollided photons). The skyshine dose rate for a shielded source is thus

$$D(d) = \int_0^\infty dE \int_{\Omega_s} d\Omega e^{-\lambda} B(E, \lambda) S(E, \Omega) \mathcal{R}(E, \Phi, d), \quad (142)$$

where λ is the mean-free-path length that a photon emitted in direction Ω travels through the shield without collision. Clearly, when there is no source shielding ($\lambda = 0$), this result reduces to the unshielded result of (135).

An alternative approach for skyshine sources of photons shielded by a horizontal slab shield is to use a simple one-dimensional Monte Carlo calculation to determine the scattered and annihilation photons that subsequently escape into the atmosphere. These escaping photons are then transported through the air with the LBRF to the point of interest far from the source (Stedry et al. 1996). In this approach, the exact energy and angular distributions of the photons are used and very accurate results can be obtained with minimal computational effort.

The integral line-beam method for photon and neutron skyshine calculations has been applied to a variety of source configurations and found to give generally an excellent agreement with benchmark calculations and experimental results (Shultis et al. 1991; Shultis and Faw 1994; Hertel et al. 2005).

7.4 Computational Resources for Skyshine Analyses

As an alternative to computationally expensive transport calculations of far-field skyshine doses, several codes, based on the line-beam response function, are available that allow evaluation of skyshine doses with minimal computational effort. SKYSHINE-III, developed by Lampley, Andrews, and Wells (1988), is the original photon LBRF code, and can be obtained from RSICC. MicroSkyshine is a commercially available code (Grove 1987) for photon skyshine using improved LBRFs (Shultis and Faw 1987). More recent photon skyshine codes include SKYDOSE, which treats source energies between 0.4 and 100 MeV and distances out to 2500 m, and McSKY, which treats shielded skyshine sources by the Monte Carlo shield approach discussed above. For neutron skyshine problems there is SKYNEUT, which computes skyshine dose out to 2500 m from an arbitrary spectrum of neutron energies, and SKYCONES, which treats sources with polar angle variations and is used in the hybrid method discussed in the previous section. With the exception of MicroSkyshine, all these codes are available from RSICC.

8 Radiation Streaming Through Ducts

Except for the simplest cases, the analysis of radiation streaming through gaps and ducts in a shield requires advanced computational procedures. Because neutron albedos, especially for thermal neutrons, are generally much higher than those for photons, multiple scattering from duct walls is more severe for neutrons than for photons, for which a single scatter analysis is often sufficient. Moreover, placing bends in a duct, which is very effective for reducing gamma-ray penetration, is far less effective for neutrons. Fast neutrons entering a duct in a neutron shield become thermalized and, thereafter, are capable of scattering many times, allowing neutrons to stream along the duct, even one with several bends. Also, unlike gamma-ray streaming, the duct need not be a void (or gas filled) but can be any part of a heterogeneous shield that is “transparent” to neutrons. Neutrons can navigate many bends and twists of the streaming channel, and consequently, the design of neutron shields containing ducts or regions with low hydrogen content must be done with great care.

The albedo concept has been found useful for simple duct analyses, and even for more complex geometries in which Monte Carlo techniques are used. Albedo methods are widely used in

the treatment of streaming, and special data sets, primarily for photons, have been developed for such use. Among these are SAIL (Simmons et al. 1979) and BREESE-II (Cain and Emmett 1979). The STORM method (Gomes and Stevens 1991) was especially devised to account for random variations in the displacement between point of entry and point of emergence in particle reflection, an important consideration in the analysis of radiation streaming. Among the few codes that deal exclusively with radiation streaming through ducts are DCTDOS (Spencer 1987) and ALBEDO/ALBEZ (Baran and Grun 1990).

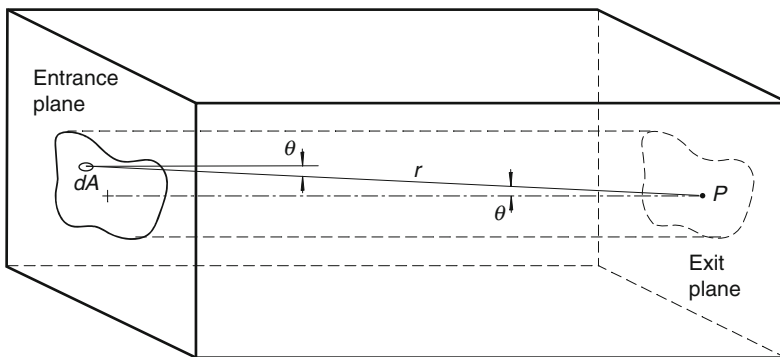
This section provides an introduction to the topic of radiation streaming through ducts, with emphasis on axisymmetric illumination of straight cylindrical ducts and two-legged ducts void of any attenuating medium. First addressed are techniques that can be applied to both neutrons and photons, and then later methods are presented that were developed for a specific type of radiation.

8.1 Characterization of Incident Radiation

Here it is assumed that radiation incident upon a duct is uniform across the entrance plane (☛ Fig. 40). The incident radiation intensity may vary with polar angle θ , but it is assumed that it does not vary azimuthally about the duct axis. The natural polar axis for describing the angular variation is the duct axis. If the angular fluence of the incident radiation at the duct entrance plane is $\Phi_o(\theta)$, then the angular flow in the plane is just $J_{no}(\theta) = \cos \theta \Phi_o(\theta)$. It is often useful to use $\omega \equiv \cos \theta$ rather than θ as the independent angular variable so that $J_{no}(\omega) = \omega \Phi_o(\omega)$. Note that θ varies from 0 to $\pi/2$ and ω from 0 to 1. The flow J_n^+ within this range, which is the total flow into the duct (per unit area of the entrance plane), is given by

$$J_n^+ = 2\pi \int_0^1 d\omega J_{no}(\omega) = 2\pi \int_0^1 d\omega \omega \Phi_o(\omega), \quad (143)$$

in which the positive superscript designates directions within the hemisphere toward the duct entrance.



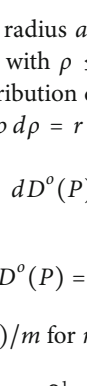
■ Figure 40
Detector response at point P on duct axis due to passage of particles through area dA in duct-entrance plane

Now suppose that the incident angular flow $J_{no}(\omega)$ is expanded in a power series. Each portion of the incident radiation characterized by a single term in a power series may be treated independently. Thus, suppose that $J_{no}(\omega) = (m+1)\omega^m J_n^+ / 2\pi$. The corresponding angular fluence is $\Phi_o(\omega) = (m+1)\omega^{m-1} J_n^+ / 2\pi$. Also, suppose that the incident radiation has energy E_o . The dose at the entrance plane is denoted by $D^o(0)$, where the superscript denotes incident radiation and the zero argument denotes the entry plane. Here,

$$D^o(0) = 2\pi \mathcal{R}(E_o) \int_0^1 d\omega \Phi_o(\omega) = \frac{m+1}{m} \mathcal{R} J_n^+, \quad (144)$$

where $\mathcal{R}(E_o)$ is the fluence-to-dose conversion factor for particles of energy E_o .

8.2 Line-of-Sight Component for Straight Ducts

Consider a dose point P in the exit plane of a straight duct illustrated in  Fig. 40. The dose at P in the exit plane, caused by radiation incident from an element of area dA in the entrance plane, is $dD^o(P) = \mathcal{R} dA J_{no}(\omega)/r^2$, in which the zero superscript denotes uncollided radiation and r is the distance from dA to point P . The uncollided dose from the entire entrance plane is


$$D^o(P) = \mathcal{R} \int_A \frac{dA}{r^2} J_{no}(\omega), \quad (145)$$

in which the integration is over the total area A of the source plane covering the duct entrance. Because $dA \omega/r^2$ is the solid angle $d\Omega$ subtended by dA at P , the dose can be expressed as an integration over the solid angle Ω subtended by the entrance area A at point P , namely,

$$D^o(P) = \mathcal{R} \int_A d\Omega \omega^{-1} J_{no}(\omega) = \mathcal{R} \int_{\Omega} d\Omega \Phi_o(\omega). \quad (146)$$

It is an important but subtle point that the line-of-sight dose *in the exit plane* of a duct is given by integrating the angular distribution of the fluence *in the entrance plane*.

8.2.1 Line-of-Sight Component for the Cylindrical Duct

Consider a duct of length Z , radius a , and aspect ratio $\beta \equiv a/Z$ as shown in  Fig. 41, but, for the line-of-sight analysis, with $\rho \leq a$, that is, with the element of area $2\pi\rho d\rho$ inside the duct entrance. The dose contribution $dD^o(P)$ at point P due to the differential annular area is $2\pi\rho d\rho \mathcal{R} J_n(\theta)/r^2$. Because $\rho d\rho = r dr$, $r = Z/\omega$, $\omega = \cos\theta$, and $dr = -Zd\omega/\omega^2$, it follows that

$$dD^o(P) = (m+1) J_n^+ \mathcal{R} d\omega \omega^{m-1}, \quad (147)$$

and upon integrating,

$$D^o(P) = (m+1) J_n^+ \mathcal{R} \int_{\omega_o}^1 d\omega \omega^{m-1}. \quad (148)$$

Because $D^o(0) = J_n^+ \mathcal{R}(m+1)/m$ for $m > 0$, this result may be written as

$$\frac{D^o(P)}{D^o(0)} = m \int_{\omega_o}^1 d\omega \omega^{m-1} = 1 - \omega_o^m = 1 - (1 + \beta^2)^{-m/2}. \quad (149)$$

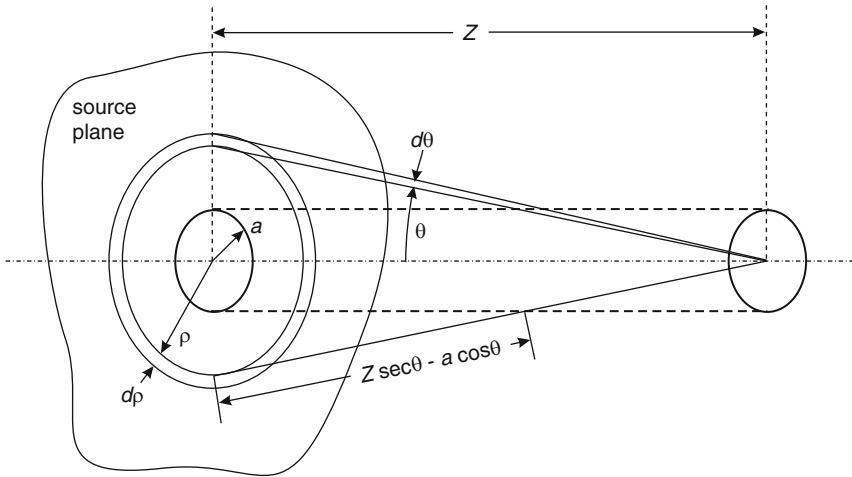


Figure 41

Geometry for evaluation of the line-of-sight and wall-penetration components of dose for a straight cylindrical duct

For the special case of $m = 1$, that is, for isotropic incident fluence, $D^o(P)/D^o(0) = \Omega/(2\pi)$, where Ω is the solid angle subtended by the duct entrance at the center of the duct exit.

The line-of-sight component of the dose at the exit of a cylindrical duct is illustrated in Figs. 42 and 44. As is quite evident from these figures, for $a \ll Z$, $D^o(P)/D^o(0) \simeq (m/2)\beta^2$, which is just the inverse-square law for attenuation of radiation from a point source.

8.2.2 Line-of-Sight Component for the Rectangular Duct

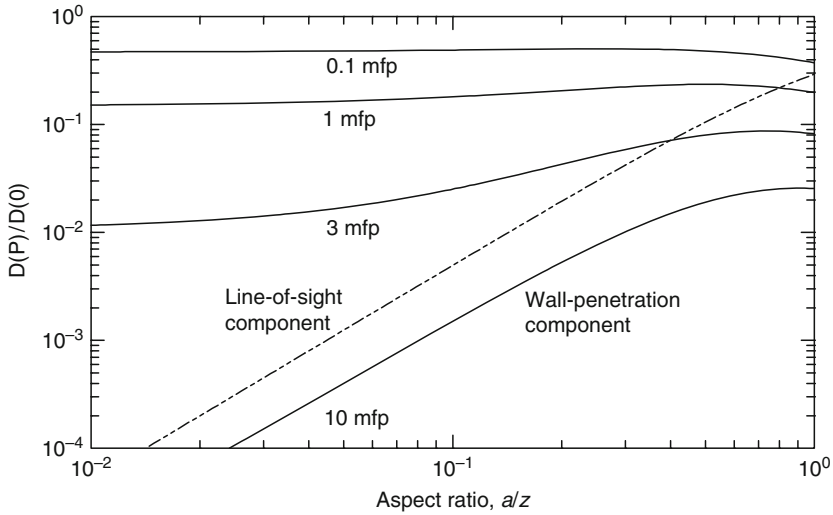
The line-of-sight component for a rectangular ducts with dimensions $W \times L$, for $J_{no}(\omega) = (m+1)\omega^m J_n^+/2\pi$, is given by (Shultis and Faw 2000)

$$D^o(P) = \frac{2}{\pi} \mathcal{R}(m+1) J_n^+ \int_0^{L/2} dy \int_0^{W/2} dx Z^m (x^2 + y^2 + Z^2)^{-(m+2)/2}. \quad (150)$$

For the special case of $m = 1$, that is, for isotropic incident fluence and just as for the cylindrical duct, $D^o(P)/D^o(0) = \Omega/(2\pi)$, where Ω is the solid angle subtended by the duct entrance at the center of the duct exit.

8.3 Wall-Penetration Component for Straight Ducts

The following discussion applies to photons, or to fast neutrons penetrating a duct wall with sufficient hydrogen content so that removal theory can be used. In the later case, the photon-attenuation coefficient μ is replaced by the appropriate removal coefficient μ_r . However, for



■ Figure 42

Line-of-sight and wall-transmission components for photons incident with isotropic fluence on a straight cylindrical duct. The independent variable is β , the aspect ratio, and the parameter is the wall thickness expressed as μZ , the number of mean free paths

thermal neutrons emitted by the source plane at the duct entrance, no simple formulas for the wall-penetration component exist.

Consider the cylindrical duct illustrated in [Fig. 41](#). Of interest is the radiation penetrating the wall through the lip of the duct entrance. This component $D^w(P)$ may be evaluated in a way very similar to that for the line-of-sight component, (147) through (149), except that $\rho \geq a$ and attenuation in the wall material must be accounted for, as is illustrated in the figure. Suppose that the effective linear-interaction coefficient for the wall material is μ . Then, the attenuation factor for a ray toward P from radius ρ is $\exp[-\mu(Z \sec \theta - a \csc \theta)]$. The analog of (149) is

$$\frac{D^w(P)}{D^o(0)} = m \int_0^{\omega_0} d\omega \omega^{m-1} \exp\left[-\mu Z \left(\frac{1}{\omega} - \frac{\beta}{\sqrt{1-\omega^2}}\right)\right]. \quad (151)$$

This ratio, which depends on *both* β as well as the mean free paths μZ of wall thickness, is illustrated in [Fig. 42](#). Obviously, for thinner walls and narrower ducts, the wall-penetration component can dominate the dose at the duct exit.

8.4 Single-Scatter Wall-Reflection Component

To evaluate this component, it is assumed that the particles entering the duct at its entrance may be treated as though coming from a point source on the duct axis. Only singly reflected particles are taken into account. Although this is a reasonable approximation for gamma rays, which

experience relatively very low albedos peaked in directions along the duct axis, it is not reasonable for thermal neutrons, which experience relatively very high albedos with more nearly isotropic reflection.

The geometry and notation for duct-wall reflection are illustrated in **Fig. 43**. The equivalent point source on the axis is located at point P_0 at the duct entrance, and dose is evaluated at point P on the axis at the other end of the duct. The source emits $S(\theta)$ monoenergetic particles per steradian, with azimuthal symmetry about the duct axis. If $J_n(\theta) = [(m + 1)/2\pi]J_n^+ \cos^m \theta$ is the fluence at the duct-entry plane, then $S(\theta) = \pi a^2 J_n(\theta) = [(m + 1)/2]a^2 J_n^+ \cos^m \theta = [(m + 1)/2]a^2 J_n^+ \omega^m$. In accord with (124), the incident flow J_{n0} at reflecting area $dA = 2\pi a dz$ is given by $\cos \theta_1 S(\theta)/4\pi r_1^2$, and because $\cos \theta_1 = a/r_1$, it follows that the portion of the dose at P due to reflection from area dA is given by

$$dD^1 = \frac{2\pi a^2 dz \mathcal{R} S(\theta)}{r_1^3 r_2^2} \alpha_D(E_o, \theta_1; \theta_2, 0). \tag{152}$$

Note that all reflections leading to the dose point require zero change in azimuthal angle ψ . The total reflected dose is given by

$$D^1(P) = 2\pi a^2 \mathcal{R} \int_0^Z dz \frac{S(\theta)}{r_1^3 r_2^2} \alpha_D(E_o, \theta_1; \theta_2, 0). \tag{153}$$

By using dimensionless variables, namely, $u \equiv z/Z$ and the aspect ratio $\beta \equiv a/Z$, this result can be expressed as

$$D^1(P) = \pi(m + 1)J_n^+ \mathcal{R} \beta^4 \int_0^1 du u^m \frac{\alpha_D(E_o, \theta_1; \theta_2, 0)}{(\beta^2 + u^2)^{(m+3)/2} [\beta^2 + (1 - u)^2]}. \tag{154}$$

For $m > 0$, this can be expressed in terms of the dose at the source plane $D^0(0)$. From (144), $D^0(0) = [(m + 1)/m] \mathcal{R} J_n^+$ for the broadly illuminated duct entrance, and because $\omega = \cos \theta = z/\sqrt{z^2 + a^2} = 1/\sqrt{1 + \beta^2/u^2}$, the ratio of the single-reflection dose at the duct exit to the dose at the center of the broadly illuminated duct entrance is, for $m > 0$,

$$\frac{D^1(P)}{D^0(0)} = \pi m \beta^4 \int_0^1 du u^m \frac{\alpha_D(E_o, \theta_1; \theta_2, 0)}{(\beta^2 + u^2)^{(m+3)/2} [\beta^2 + (1 - u)^2]}, \tag{155}$$

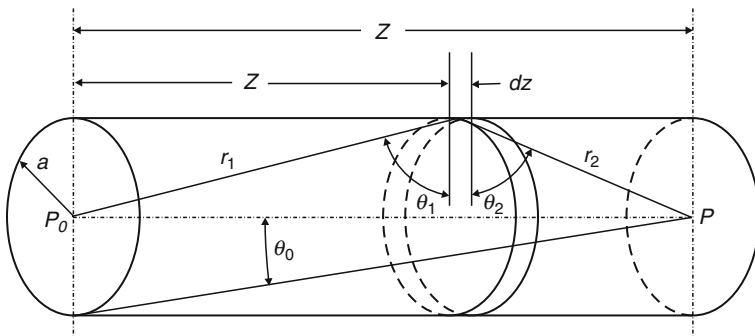
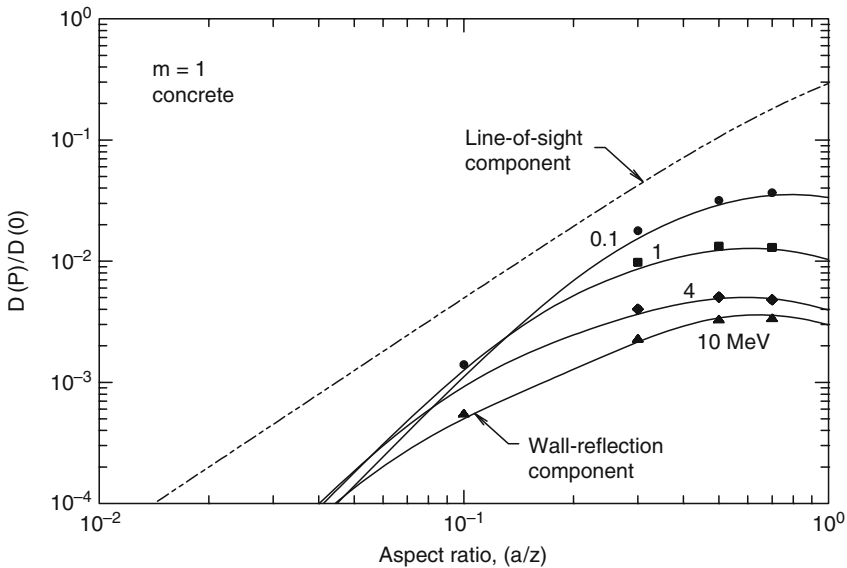


Figure 43
Geometry for evaluation of single-wall reflection in a straight cylindrical duct



■ Figure 44

Line-of-sight and single wall-reflection component for photons incident with isotropic fluence on a straight cylindrical duct in a concrete wall. The independent variable is β , the aspect ratio, and the parameter is the photon energy. The data points represent the multiple-reflection dose for a 0.1-MeV equivalent point source at the entry of a cylindrical duct in a 2-m-thick concrete wall, computed using the MCNP Monte Carlo radiation-transport computer code

in which $\theta_1 = \cot^{-1}[\beta/u]$ and $\theta_2 = \cot^{-1}[\beta/(1-u)]$. The reader will note that, for specified photon energy and wall material, the reflection component of the exit dose is a function of only the aspect ratio. Representative results are illustrated in [► Fig. 44](#). Even for concrete, which has higher albedos than iron or lead, the wall-reflection component of the dose is generally much less than the line-of-sight component.

8.5 Photons in Two-Legged Rectangular Ducts

Photon transmission through multiple-legged ducts of arbitrary cross section is beyond the scope of this chapter. However, an albedo approach that might be employed in general cases is illustrated here for a two-legged rectangular duct. Details of this analysis and refinements to account for lip and corner penetration are described by LeDoux and Chilton (1959).

The geometry is illustrated in [► Fig. 45](#). It is assumed here that the lengths of the duct's legs are appreciably greater than the widths and heights of the legs and that the duct walls are of uniform composition and at least two mean-free-path-lengths thick. The dose $D(P)$ is evaluated at the center of the duct exit. Photons entering the duct are approximated by an anisotropic source $S(\theta)$ at the center of the duct entrance. For example, if the axisymmetric angular flow at the duct entrance plane is $J_n(\theta)$ and the cross-sectional area of the duct entrance is A ,

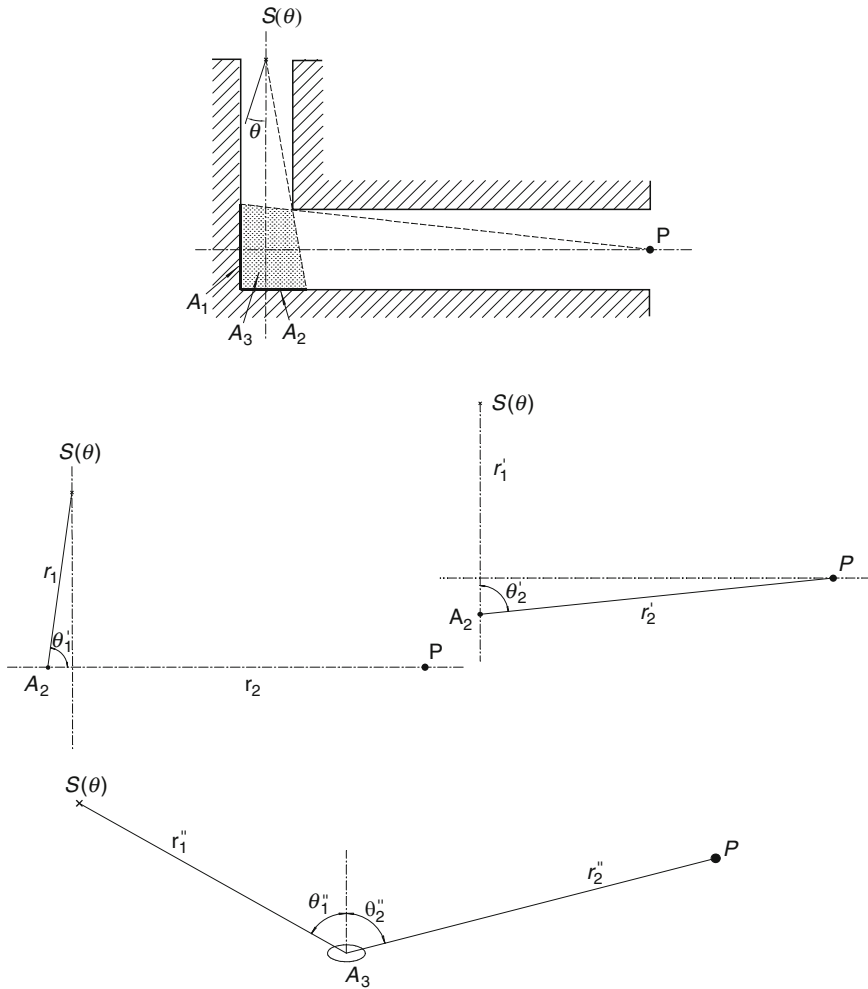


Figure 45
Prime scattering areas in radiation transmission through two-legged rectangular ducts

$S(\theta) = AJ_n(\theta)$. Here a monoenergetic photon source is assumed, although generalization of the method to polyenergetic sources is straightforward.

The analysis by LeDoux and Chilton is based on the approximation that the dose at P , $D(P)$, consists principally of responses to radiation reflected from *prime scattering areas*, that is, areas on the duct walls visible to both source and detector and from which radiation may reach the detector after only a single reflection. There are four prime scattering areas as can be seen in **► Fig. 45**, namely, areas A_1 and A_2 on the walls, and areas A_3 and A_4 on the floor and ceiling (considering the figure to be a plan view). Photon reflection from each area is treated as though it occurred from the centroid of the area. Thus, the transmitted dose may be expressed as

$$D(P) = D_1(P) + D_2(P) + 2D_3(P). \quad (156)$$


According to (124),

$$D_1(P) = \frac{\mathcal{R}A_1S(\pi/2 - \theta'_1) \cos \theta'_1 \alpha_D(E_o, \theta'_1; 0, 0)}{(r_1 r_2)^2}, \quad (157)$$

$$D_2(P) = \frac{\mathcal{R}A_2S(0) \alpha_D(E_o, 0; \theta'_2, 0)}{(r'_1 r'_2)^2}, \quad (158)$$

and


$$D_3(P) = \frac{\mathcal{R}A_3S(\pi/2 - \theta''_1) \cos \theta''_1 \alpha_D(E_o, \theta''_1; \theta''_2, \pi/2)}{(r''_1 r''_2)^2}, \quad (159)$$

in which the various arguments of the albedo function α_D are identified in  Fig. 45. Penetration of radiation through the corner lip can also be estimated in a similar manner (Shults and Faw 2000).

8.6 Neutron Streaming in Straight Ducts

Neutron streaming in straight ducts can be treated in the same context as gamma-ray streaming (see (148) and (150)). Neutron streaming may be treated similarly if the material surrounding the duct is a hydrogenous medium for which removal theory can be applied by replacing the attenuation coefficient μ for photons by the appropriate removal coefficient μ_r . However, for thermal neutrons no simple approximation is available. In this section, the albedo method is used to estimate the wall-scattered component. First, single-wall scattering is considered for neutrons.

Single-Wall Scattering

To describe the neutron albedo from the duct walls, it is assumed that neutrons are reflected partially isotropically and partially with a cosine distribution. In particular, the differential-wall dose albedo is approximated (using the notation of  Fig. 43) as

$$\alpha_D(E_o, \theta_1; \theta_2, 0) \simeq A_D \frac{\gamma + 2(1 - \gamma) \cos \theta_2}{2\pi}, \quad (160)$$

where A_D is the *dose reflection factor*, the fraction of incident dose reemitted in all outward directions from the wall surface, γ is the fraction of neutrons reemitted isotropically, and $(1 - \gamma)$ is the fraction reemitted with a cosine distribution. With this albedo approximation, the single-scatter dose given by (154) can be written as

$$D^1(P) = \frac{1}{2} J_n^+ \mathcal{R} \beta^2 A_D [\gamma I_{0,m} + 2\beta(m+2)(1-\gamma)I_{1,m}], \quad (161)$$

where the $I_{n,m}$ integral is defined for $n = 0, 1$ and $m \geq 0$ as

$$I_{n,m}(\beta) \equiv \beta^2 \frac{m+1}{(m+2)^n} \int_0^1 du \frac{u^m}{(\beta^2 + u^2)^{(m+3)/2} [\beta^2 + (1-u)^2]^{(n+2)/2}}. \quad (162)$$

The integral $I_{n,m}$ approaches unity (Chilton et al. 1984), as the aspect ratio becomes very small (i.e., for $\beta \equiv a/Z \ll 1$). For such ducts, illuminated by an isotropic source plane ($m = 0$), (161) reduces to

$$D^1(P) = \frac{1}{2} J_n^+ \mathcal{R} \beta^2 A_D [\gamma + 4\beta(1 - \gamma)]. \quad (163)$$

This result is known as the Simon and Clifford (1956) single-scatter duct formula.

Multiple-Wall Scattering

Because of the relatively high albedo for neutrons, they can scatter many times from a duct wall before reaching the duct exit. An analytical estimation of the multiple wall-scatter component is a formidable task. Simon and Clifford (1956) showed that, for the albedo of (160) and a long cylindrical duct ($Z \gg a$) illuminated by a source plane with isotropic incident fluence, that the wall-scattered component, including all orders of scatters, is given by (163), with the total albedo A_D replaced by

$$A'_D = 1 + A_D + A_D^2 + A_D^3 + A_D^4 + \dots = \frac{A_D}{1 - A_D}. \quad (164)$$

Thus, the dose from both the line-of-sight and multiple wall-scattered components at the duct exit is

$$D(P) = J_n^+ \mathcal{R} \beta^2 \left\{ 1 + \frac{A_D}{1 - A_D} [\gamma + 4(1 - \gamma)\beta] \right\}. \quad (165)$$

Here the line-of-sight component is obtained by treating the entrance as a disk source of radius a and evaluating the uncollided dose at a distance Z from the disk's center. The result is $D^0(P) \simeq J_n^+ \mathcal{R} \beta^2$ (Shultis and Faw 2000).


The result above holds for cylindrical ducts with a small aspect ratio a/Z . For larger ratios, the importance of the infinite number of internal reflections implied by (164) becomes less. Artigas and Hungerford (1969) have produced a more complicated version of (165), which gives better results for $a/Z > 0.3$ (Selph 1973).

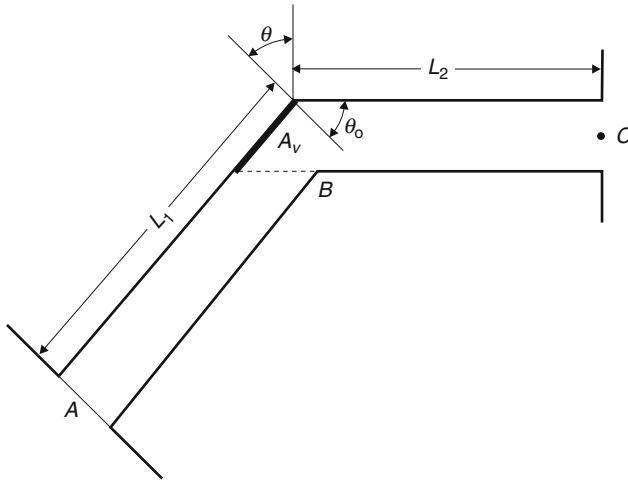
8.7 Neutron Streaming in Ducts with Bends

To reduce radiation reaching the duct exit, shield designers often put one or more bends in the duct. Analyzing the effect of bends is an important but difficult task for the designer. However, a few simplified techniques are available for estimating transmitted neutron doses through ducts with bends. Albedo methods are widely used for treating neutron streaming through bent ducts. These methods range from simple analytical models, such as those presented in this section, to Monte Carlo methods that use albedos to reflect neutrons from duct walls and, thereby, allow them to travel large distances along the duct (Brockhoff and Shultis 2007).

8.7.1 Two-Legged Ducts

Neutron Streaming in a Two-Legged Cylindrical Duct

A two-legged cylindrical duct of radius a , shown in  Fig. 46, is first considered. The two legs are bent at an angle θ such that neutrons emitted from the source plane across the duct



■ **Figure 46**
Geometry for the two-legged duct model

entrance at A cannot stream directly to the duct exit at C . Both legs are assumed to have small aspect ratios, that is, $a/L_1 \ll 1$ and $a/L_2 \ll 1$. The uniform source plane emits neutrons into the duct with a general cosine flow distribution $J_n^+(\psi) = (m+1)J_n^+ \cos^m \psi / (2\pi)$, where ψ is the angle with respect to the normal to the source plane.

The uncollided dose on the duct centerline at the duct bend B arising from the disk source at the duct entrance is, for $a/L_1 \ll 1$, (Shultis and Faw 2000)

$$D^o(B) = (m+1)\mathcal{R}(E_o) \frac{J_n^+}{2} \left(\frac{a}{L_1} \right)^2. \quad (166)$$

Neutrons that reach the bend enter the duct-wall material, interact, and some are scattered back into the duct. Those neutrons reaching the duct exit at C are those that are reradiated from the portion of the duct wall visible from C , namely from the area $A_v = \pi a^2 / \sin \theta$. With the albedo concept [cf. (122)], the reflected or reradiated dose at C can be expressed as (recall that $a/L_2 \ll 1$)

$$D(C) = D^o(B) \cos \xi \widehat{\alpha}_D(\theta_o) \frac{A_v}{L_2^2}, \quad (167)$$

where ξ is some effective incident angle at the bend, and $\theta_o = (\pi/2) - \theta$ is the angle with respect to the normal to A_v at which reradiated neutrons reach the duct exit. Here $\widehat{\alpha}_D$ is a *differential reradiation probability*, analogous to the differential dose albedo. Assume that a fraction γ of the reradiated neutron flow from A_v is isotropic and a fraction $(1-\gamma)$ has a cosine distribution, so that

$$\widehat{\alpha}_D(\theta_o) = \widehat{A}_D \frac{\gamma + 2(1-\gamma) \cos \theta_o}{2\pi}. \quad (168)$$

The quantity \widehat{A}_D is the fraction of all the neutrons incident on the wall surfaces at the bend that are reradiated from A_v .

Finally, substitution of (166) and (168) into (167), along with the relation $\cos \theta_o = \sin \theta$, gives the transmitted dose at C as

$$D(C) = (m+1)J_n^+ K \mathcal{R}(E_o) \left(\frac{a^2}{2L_1^2} \right) \left(\frac{a^2}{2L_2^2} \right) \frac{\gamma + 2(1-\gamma) \sin \theta}{\sin \theta}, \quad (169)$$

where $K \equiv \widehat{A}_D \cos \xi$ is treated as an empirical constant. This result for the case of isotropic source flow ($m = 0$) was first obtained by Simon and Clifford (1956). Although cylindrical ducts have been used in this somewhat heuristic derivation, any simple duct shape could be used and only a slightly different expression would result.

Neutron Streaming in a Two-Legged Rectangular Duct

The LeDoux–Chilton albedo analysis of a two-legged L-shaped duct discussed in Section 8.5 cannot be applied directly to the neutron duct problem because of the importance of multiple scattering from the duct walls for the neutron case. However, Chapman (1962) extended the LeDoux–Chilton model to include second-order scattering effects, and Song (1965) used this refined model successfully to treat neutron transmission.

8.7.2 Neutron Streaming in Ducts with Multiple Bends

The Simon–Clifford model for a two-legged cylindrical duct can be extended to a duct with N legs. With this extension, the dose at the exit of the N th leg is

$$D(L_N) = (m+1)J_n^+ \mathcal{R}(E_o) \left(\frac{a^2}{2L_1^2} \right) \times \prod_{i=2}^N \left[K \left(\frac{a^2}{2L_i^2} \right) \left(\frac{\gamma + 2(1-\gamma) \sin \theta_i}{\sin \theta_i} \right) \right]. \quad (170)$$

This result can be applied to a duct that makes a curved path through the shield by dividing the duct into a series of straight-line segments of length equal to the maximum chord length that can be drawn internal to the duct (Selph 1973). In particular, if the duct is conceptually represented by a series of N equal-length (L) and equally bent (θ) legs, the dose at the duct exit is

$$D(L_N) = (m+1)J_n^+ \mathcal{R}(E_o) \left(\frac{a^{2N} K^{N-1}}{2^N L^{2N}} \right) \left(\frac{\gamma + 2(1-\gamma) \sin \theta}{\sin \theta} \right)^{N-1}. \quad (171)$$

8.8 Empirical and Experimental Results

There is much literature on experimental and calculational studies of gamma-ray and neutron streaming through ducts. In many of these studies, empirical formulas, obtained by fits to the data, have been proposed. These formulas are often useful for estimating duct-transmitted doses under similar circumstances. As a starting point for finding such information, the interested reader is referred to Rockwell (1956), Selph (1973), NCRP (1977, 1984), and Weise (1994).

9 Shield Design

9.1 Shielding Design and Optimization

Shielding design embodies essentially the same considerations as shielding analysis. Both require thorough characterization of radiation sources and receptors as well as comprehensive information on shield properties. Such properties encompass not only the nuclear characteristics but also the thermal properties and certainly, structural properties. Shield optimization may have the goal of minimizing weight, volume, or cost. Minimum weight is a common goal, but it is easy to envision cases where shield volume or shield cost might control.

Source characterization is a major task. Usually, the source emits gamma rays or a mixture of neutrons and gamma rays. In either case, the energy spectra and spatial distributions must be known. On occasion, a surface such as the outside of a nuclear reactor pressure vessel is identified as a “(secondary) source surface.” Then, it is necessary to specify angular distribution as well as energy spectrum. When thermal effects are important, it may be necessary to account for charged particles or low-energy X-rays or Auger electrons released from the primary source. Similarly, such low energy particles may be released in the course of reactions taking place as primary radiations are attenuated.

Receptor characterization is another important task. What are dose and dose rate limitations and are they specified at a point or averaged over a region? Does the dose apply to a physical or anthropomorphic phantom? Is the shielding designed to protect workers, individual members of the public, or population groups? Otherwise, is the shielding designed to protect materials or equipment?

Materials characterization poses broad demands for information ranging from nuclear properties to structural properties. Some materials are effective in attenuating gamma rays but ineffective in attenuating neutrons. Therefore, in many instances, composite materials, perhaps homogenous and perhaps layered, are demanded. Thereby, shield geometry – numbers and thicknesses of layers – enters into the shield-optimization problem. Elemental compositions and densities of material components must be known. Cross sections must be known by element. In some cases, for example, dealing with boron- or lithium-shield components, isotopic compositions and cross sections must also be known. Structural properties, including thermal expansion characteristics, must also be known. Other considerations include sensitivity to heat, relative humidity, and radiation damage. Long-term composition changes such as water loss from concrete may also play a role in material selection and shield optimization.

Shield optimization may well be a “brute force” trial-and-error procedure, tempered by experience. As computational resources continue to improve, the trial-and-error approach gains favor. However, there are elegant, well-known optimization procedures calling on the application of variational principles to find an optimal design for the given design criteria and constraints. Blizard (1962) describes shield optimization by weight using methods of variational calculus. Mooney and Schaeffer (1973) also address variational methods and cite a number of applications. Claiborne and Schaeffer (1973) integrate the many design considerations into a comprehensive review of the three distinct phases in reactor shielding design: (1) preliminary conceptual design, (2) correlation of phase (1) with mechanical design to obtain a final conceptual design, and (3) translation of the final conceptual design into a detailed engineering design. In doing so, they draw on the experience of Hungerford (1966) in the design of the shielding for the Enrico Fermi sodium-cooled nuclear power plant. Hungerford (1968) put forth six

principles of shield design to be followed in developing the shield system for a nuclear power reactor:

1. *Reactor Shield Unity*: A shield is an integral part of a reactor system and must be designed at the same time as, and as an entity with, the overall reactor system.
2. *Shield Integrity*: Adjacent parts of a shield, having the same design criteria, must be designed with equal performance characteristics.
3. *Shield Safety*: Because the reactor shield is a safety device and must be considered as a part of the safety system of the reactor, there can be no compromise with expediency in its design.
4. *Shield Accommodation*: A shield should be adapted to provide for the mechanical requirements of the reactor, its supporting structure, and its component systems, without sacrificing the principles of reactor shield unity, shield integrity, or shield safety.
5. *Shield Economy*: The best possible shield should be designed at the lowest possible cost, consistent with the overall reactor design, without sacrificing safety, integrity, or accommodation.
6. *Shield Simplicity*: A shield should be designed to be as simple in configuration as possible, with the minimum number of voids, ducts, and cutouts for the reactor components and auxiliary systems, consistent with the principle of shield accommodation.

Two comprehensive resources for shielding design are Vols. II and III of the Engineering Compendium on Radiation Shielding (Jaeger et al. 1975, 1970). Volume III (1970) addresses the following individual topics in shielding design: the design of shielding for research and testing reactors, stationary power reactors, and ship-propulsion reactors. Also addressed are the design of shipping and storage containers, hot cells, medical irradiation facilities, accelerators, and nuclear fuel processing plants. In the preface to the volume, Jaeger points out that radiation attenuation analysis is a design tool in two states: first, in an approximate comparative assessment of design alternatives, then, in complex engineering considerations reaching a balance between the aspects of safety and economy and the functional requirements of nuclear facilities. Volume II (1975) provides a wealth of information on mechanical, thermal, and technological properties of gamma-ray and neutron shields, as well as optimal choices of shielding materials. Two American National Standards, ANSI/ANS-6.4-2006 and ANSI/ANS-6.4.2-2006, not only address shielding standards but also provide comprehensive guidance on shielding materials and fabrication, especially for concrete.

9.2 Shielding Materials

In this section, essential properties and compositions of shielding materials are summarized. These materials include natural materials such as air, water, and soil as well as materials of construction. Specialized materials for X-ray facilities are addressed, as are special materials for neutron shielding.

9.2.1 Natural Materials

Air and water, the most natural of materials, require an understanding of their shielding properties. Air properties are critical in dealing with design or analysis involving atmospheric skyshine and when irradiated by neutrons. Dry air, at 1 atmosphere and 20°C has a density of 0.00120 g/cm³. Ordinarily ideal gas laws may be applied to account for different temperatures

■ **Table 22**
Compositions of Five Representative Soil Types

	Weight Fractions for Soil Types				
	Nominal	Dry porous	Dry dense	Wet porous	Wet dense
Hydrogen	0.023	0.015	0.015	0.030	0.030
Oxygen	0.559	0.529	0.529	0.585	0.585
Silicon	0.223	0.243	0.243	0.206	0.206
Aluminum	0.065	0.071	0.071	0.060	0.060
Iron	0.040	0.044	0.044	0.037	0.037
Calcium	0.029	0.032	0.032	0.027	0.027
Potassium	0.021	0.023	0.023	0.019	0.019
Sodium	0.023	0.025	0.025	0.021	0.021
Magnesium	0.017	0.018	0.018	0.015	0.015

Source: Shue et al. (1998)

■ **Table 23**
Characteristics of Five Representative Soil Types

	Soil Type				
	Nominal	Dry porous	Dry dense	Wet porous	Wet dense
Porosity ^a	0.5	0.6	0.4	0.6	0.4
Free water content ^b	0.2	0.1	0.1	0.3	0.3
Bound water content ^c	0.05	0.05	0.05	0.05	0.05
Mineral density (g/cm ³) ^d	2.684	2.684	2.684	2.684	2.684
In situ density (g/cm ³)	1.610	1.181	1.771	1.396	2.094

^aFraction of total volume occupied by water and air.

^bRatio of free water mass to mineral mass.

^cRatio of bound water mass to mineral mass.

^dMineral density includes bound water.

Source: Shue et al. (1998)

or pressures as well as to account for humidity. In dry air, weight fractions by element are N: 0.7553, O: 0.2318, C: 0.0001, and Ar: 0.0128. ⁴⁰Ar, present at 0.996 atomic fraction, captures thermal neutrons with the cross section of 0.66 b. The product ⁴¹Ar decays with a half-life of 110 m, releasing a beta particle and, with 99.6% frequency, a 1.293-MeV gamma ray.

Hydrogen present in water with 0.112 weight fraction, captures thermal neutrons with a cross section of 0.33 b and, in the process, releases a 2.23-MeV-capture gamma ray. In a complementary reaction with 2.23-MeV threshold, photoneutrons are produced in the interaction of gamma rays with deuterium.

Soils often find use as radiation shields; however, water content is highly variable, depending on environmental conditions. ➤ [Tables 22](#) and [23](#) list characteristics of a range of soil types. Similarly, untreated wood, though useful for neutron attenuation, loses water over time and is, therefore, generally found unacceptable as a shield material.

9.2.2 Concrete

Cost, density, compressive strength, ease of placement, and effectiveness in attenuation of both neutrons and gamma rays make concrete a highly desirable shielding material. Neutron shielding by concrete and the importance of water (hydrogen) content are addressed earlier in this chapter and is not repeated here. Types of concrete are characterized by the type of aggregate, *siliceous* referring to quartz based aggregate and *calcareous* referring to limestone based aggregate. Table 24 lists components of three types of “ordinary” concrete: NBS Type 03, Type 04, and the current NIST ordinary concrete (Hubbell & Seltzer 2004). Type 04 is commonly cited and appears to be accepted as “representative.” High-density concrete is often used to provide greater attenuation for a given thickness. Additives for this type of concrete include scrap metal such as steel punchings and metallic ores. Magnetite concrete ($\rho = 3.53 \text{ g/cm}^3$) contains in the mix iron oxide to the extent 4900 lb/yd³. Barite concrete ($\rho = 3.35 \text{ g/cm}^3$) contains barium sulfate ore to the extent 5000 lb/yd³. ANSI/ANS-6.4-2006 lists other high-density concretes plus a low-density ($\rho = 2.1 \text{ g/cm}^3$) serpentine concrete for high temperature applications.

Reinforcing steel, or *rebar*, provides tensile strength and adds density to concrete. For gamma-ray shielding, it is generally satisfactory to conceptually homogenize the reinforced concrete. For neutron shielding, however, channeling effects very often call for treatment of the reinforced concrete as a combination of a continuous concrete phase with steel heterogeneities.

Table 24
Compositions of Types 03 and 04 and NIST Ordinary
Concretes

Elemental Composition (partial g/cm ³)			
Element	Type 03	Type 04	NIST
Hydrogen	0.020	0.013	0.051
Carbon	0.118		0.006
Oxygen	1.139	1.171	1.322
Sodium		0.040	0.035
Magnesium	0.057	0.006	0.003
Calcium	0.582	0.194	0.099
Aluminum	0.085	0.107	0.046
Sulfur	0.007	0.003	
Silicon	0.342	0.742	0.701
Potassium	0.004	0.045	0.023
Iron	0.003	0.029	0.015
Nickel	0.026		
Phosphorus	0.007		
Total	2.39	2.35	2.300

Source: ANL-5800 (2nd ed.), ANSI/ANS-6.4-2006, Hubbell and Seltzer (2004)

9.2.3 Metallic Shielding Materials

Very often it is necessary to address shielding properties of alloy (carbon) steels and stainless steels. Alloy steel has a nominal density of 7.86 g/cm^3 , contains 0.2 to 0.4% carbon by weight plus varying concentrations of Si, Mn, Cr, Ni, Mo, P, and S. Stainless steel, with density typically $7.9\text{--}8.0 \text{ g/cm}^3$, contains up to about 0.08% carbon by weight and large concentrations of Mn, Cr, Ni, and Mo. In the presence of neutrons, cobalt must be held to the lowest concentration possible to prevent activation yielding the gamma-ray emitter ^{60}Co .

Other important metallic shielding materials are lead, tungsten, and uranium. Next to concrete, lead is no doubt the most common shield material. It has low strength, a low melting point (327°C), and a high density (11.34 g/cm^3). Tungsten has high strength and a high melting point (3410°C). Uranium, especially uranium depleted in ^{235}U , has high strength, intermediate melting point (857°C), and a high density ($18.5\text{--}19.0 \text{ g/cm}^3$).

9.2.4 Special Materials for Neutron Shielding

Shielding of epithermal or fast neutrons requires a two stage process. Fast neutrons can rarely be captured or absorbed; thus, it is first necessary to slow neutrons to thermal energies, as the first step, and then to absorb them. The slowing-down process itself may be in two stages. Neutrons with many MeV of energy may be slowed by inelastic scattering with atoms of, for example, iron. This is the removal process discussed in [5.3](#). At neutron energies below about 6 MeV, the elastic scattering cross section of hydrogen exceeds the inelastic scattering cross section of iron. Thus, in addition to a component such as iron, a hydrogenous component is needed for efficient neutron thermalization. Thermal neutrons are readily captured, unfortunately, in most instances releasing high-energy capture-gamma rays. Thus, for an effective neutron shield, a strong absorber such as boron or lithium, perhaps indium or cadmium, is needed to avoid significant capture-gamma rays.

Boron for Neutron Attenuation

Natural boron contains 19.9 atomic percent ^{10}B and 80.1 percent ^{11}B , the former with a 3840-b (2200-m/s) absorption cross section, the latter with only 5 mb. The absorption of a neutron by ^{10}B releases a 0.48-MeV gamma ray – significant, but of lower energy than most capture gamma rays. Boron shielding materials are available in the form of boron carbide, B_4C , with density 2.51 g/cm^3 , borated graphite, boron carbide mixed in graphite, and boral (a mixture of boron carbide in aluminum cladding). Plates or sheets of boral commonly contain 35% boron by weight and are available up to 1 by 3 m^2 in area and thicknesses of 0.125 and 0.25 in. Boron shielding is also available as borated polyethylene in a wide range of shapes and compositions, in a wide range of boron concentrations, and even in castable form. For mixed neutron and gamma-ray shielding, lead-loaded borated polyethylene is also available.

Lithium for Neutron Attenuation

Natural lithium contains 7.5 atomic percent ^6Li and 92.5 percent ^7Li . The former has an exceptionally high cross section (941 b) for thermal-neutron absorption and

produces no secondary gamma rays. It is light in weight and available enriched in ^6Li . It is offered commercially as lithium polyethylene, with 7.5% lithium by weight and in a variety of shapes.

9.2.5 Materials for Diagnostic X-Ray Facilities

There are six materials of prime concern in the design of diagnostic facilities. Of these, concrete, steel, and lead have already been addressed. Others are wood, plate glass, and gypsum wallboard. Shielding design considerations are documented by Jaeger et al. (1975), Archer et al. (1994), and NCRP (2005).

Depending on hydrogen content, wood density varies from 0.5 to 0.8, nominally 0.55 g/cm^3 , and is essentially cellulose, water, and lignin. Crown glass, a silica soda lime glass, is durable and has a low index of refraction. Density is $2.5\text{--}2.7\text{ g/cm}^3$. Lead oxide may be added at up to about 0.75 weight fraction Pb to yield lead glass with density up to about 6.2 g/cm^3 . Sheets are available with lateral dimensions up to about 140 cm and thicknesses up to about 40 cm. Plaster board, or gypsum wallboard, has a density typically 2.32 g/cm^3 . By weight fraction, gypsum composition is H 0.0234, O 0.5576, S 0.1862, and Ca 0.2328. Typical thickness is 14 mm of gypsum plus 1 mm of paper. Sheets may be lined with lead in thicknesses 1/32 in to 1/8 in.

9.3 A Review of Software Resources

Listed below are selected software packages of interest in shielding design and analysis. All are available from the Radiation Safety Information Computational Center, accessible on line at <http://www-rsicc.ornl.gov/>.

- **QAD-CGGP**: point kernel code featuring combinatorial 3D geometry and source options with geometric progression buildup factors for gamma rays
- **QADMOD-GP**: point kernel code featuring faster 3D geometry and source options with geometric-progression buildup factors for gamma rays
- **G-33**: point kernel code featuring multi-group gamma-ray scattering with QAD geometry and GP-buildup factors
- **ISOSHL**: point kernel code featuring multiple isotope sources, limited geometry, and source description
- **DOORS**: discrete ordinates code package incorporating ANISN, DORT, and TORT codes for 1, 2, and 3D discrete ordinates calculations
- **PARTISN**: discrete ordinates code featuring multidimensional, time-dependent, multigroup discrete ordinates transport code system
- **COHORT**: Monte Carlo code featuring radiation transport; flexible geometry
- **MORSE**: Monte Carlo code featuring multigroup neutron and gamma-ray transport; combinatorial geometry
- **MCNP**: Monte Carlo code featuring continuous energy, neutral particle transport; flexible geometry
- **ORIGEN**: neutron activation code featuring neutron activation, radioactive decay, and source-term analysis

9.4 Shielding Standards

Listed below are ANSI/ANS standards pertinent to shielding design. Standards 6.4 and 6.4.2 cite standards of other sponsors such as ASME and IEEE as well as selected international standards.

- ANSI/ANS-5.1-2005: Decay Heat Power in Light Water Reactors
- ANSI/ANS-6.1.2-1999: Neutron and Gamma-Ray Cross Sections for Nuclear Radiation Protection Calculations for Nuclear Power Plants
- ANSI/ANS-6.3.1-1987;R1998;R2007 (R=Reaffirmed): Program for Testing Radiation Shields in Light Water Reactors (LWR)
- ANSI/ANS-6.4-2006: Nuclear Analysis and Design of Concrete Radiation Shielding for Nuclear Power Plants
- ANSI/ANS-6.4.2-2006: Specification for Radiation Shielding Materials
- ANSI/ANS-6.6.1-1987;R1998;R2007 (R=Reaffirmed): Calculation and Measurement of Direct and Scattered Gamma Radiation from LWR Nuclear Power Plants
- ANSI/ANS-18.1-1999: Radioactive Source Term for Normal Operation for Light Water Reactors
- ANSI/ANS-19.1-2002: Nuclear Data Sets for Reactor Design Calculations
- ANSI/ANS-19.3.4-2002: The Determination of Thermal Energy Deposition Rates in Nuclear Reactors

10 Health Physics

As it passes through biological tissue, radiation interacts with ambient atoms and produces chemical free radicals that, in turn, cause oxidation–reduction reactions with cell biomolecules. However, how such reactions affect the cell and produce subsequent detrimental effects to an organism is not easily determined. Because of the obvious concern about the biological effects of radiation, much research has been directed toward understanding the hazards associated with ionizing radiation.

There are two broad categories of radiation hazards to humans. *Hereditary effects* result in damage to the genetic material in germ cells that, although not detrimental to the individual exposed, may result in hereditary illness to succeeding generations. *Somatic effects* affect the individual exposed and are further classified by the nature of the exposure, for example, *acute* or *chronic*, and by the time scale of the hazard, for example, short term or long term. The short-term acute effects on the gastrointestinal, respiratory, and hematological systems are referred to as the *acute radiation syndrome*.

The effects of human exposure to ionizing radiation depend on both the exposure as well as its duration. Acute, life-threatening exposures lead to *deterministic* consequences requiring medical treatment. For such exposures, illness is certain, with the type and severity depending on the exposure and the physical condition of the individual exposed.

By contrast, minor acute or chronic low-level exposures produce stochastic damage to cells and subsequent ill effects are quantifiable only in a probabilistic sense; hereditary illness or cancer may or may not occur. Only the probability of illness, not its severity, is dependent on the radiation exposure. Such consequences are, thus, *stochastic* as distinct from *deterministic*. Although the effects of low-level radiation exposures to a large number of individuals can be estimated, the effect to a single individual can be described only probabilistically.

10.1 Deterministic Effects from Large Acute Doses

There are two circumstances under which a person can receive high doses of ionizing radiation. The first is accidental, and most likely involves a single exposure of short duration. The second is from medical treatments, and often involves doses delivered daily for several weeks and which may be delivered under conditions designed to intensify the response of certain organs and tissues to the exposures. Here, only single acute exposures to all or part of the body are considered. Issues such as fractionation and effect modification, which pertain largely to medical exposures, are not addressed.

10.1.1 Effects on Individual Cells

The probability that a particular radiation exposure kills a cell or prevents it from dividing depends on many factors. The two most important factors are the dose rate and the LET of the radiation. Doses delivered at low dose rates allow the cell's natural repair mechanism to repair some of the damage, so that the consequences are generally not as severe as if the doses were delivered at high dose rates. High LET radiation, like alpha particles, creates more ion–electron pairs closer together than does low LET radiation. Consequently, high LET radiation produces more damage to a cell it passes through than would, say, a photon.

The position in a cell's life cycle at the time of exposure also greatly affects the damage to the cell. Cell death is more likely if the cell is in the process of division than if it is in a quiescent state. Thus, radiation exposure results in more cell death in organs and tissues with rapidly dividing cells, such as the fetus (especially in the early stages of gestation), the bone marrow, and the intestinal lining. Whole-body absorbed doses of several Gy are life-threatening largely because of stem cell killing in the bone marrow and lining of the intestines. However, in these tissues and in most other tissues and organs of the body, there are ample reserves of cells, and absorbed doses of much less than one Gy are tolerable without significant short-term effect. Similarly, radiation doses which would be fatal if delivered in minutes or hours may be tolerable if delivered over significantly longer periods of time. Age, general health, and nutritional status are also factors in the course of events following radiation exposure.

For those tissues of the body for which cell division is slow, absorbed doses which might be fatal if delivered to the whole body may be sustained with little or no effect. On the other hand, much higher absorbed doses may lead ultimately to such a high proportion of cell death that, because replacement is so slow, structural or functional impairment appears perhaps long after exposure and persists perhaps indefinitely.

10.1.2 Deterministic Effects in Organs and Tissues

In this section, only deterministic somatic effects – effects in the person exposed – are considered. These effects have well-defined patterns of expression and thresholds of dose, below which the effects do not occur. The severity of the effect is a function of dose. The stochastic carcinogenic and genetic effects of radiation are addressed later.

The risk, or probability of suffering a particular effect or degree of harm, as a function of radiation dose above a threshold dose D_{th} , can be expressed in terms of a 50th-percentile dose D_{50} , or median effective dose, which would lead to a specified effect or degree of harm in half the persons receiving that dose. The D_{50} dose depends, in general, on the rate at which the dose is received. For doses below a threshold dose D_{th} , the effect does not occur.

A summary of important deterministic effects is given in [Table 25](#). Information about these and other effects on particular organs and tissues can be found in the following sources: Information is taken from the following sources: (Langham 1967; Upton and Kimball 1967; Wald 1967; NCRP 1971a; Vogel and Motulsky 1979; Pochin 1983; ICRP 1984, 1991; UN 1988; Shultis and Faw 2008).

10.1.3 Potentially Lethal Exposure to Low-LET Radiation

The question of what constitutes a *lethal dose* of radiation has, of course, received a great deal of study. There is no simple answer. Certainly, the age and general health of the exposed person are key factors in the determination. So, too, are the availability and administration of specialized medical treatment. Inadequacies of dosimetry make interpretation of sparse human data difficult. Data from animal studies, when applied to human exposure, are subject to uncertainties in extrapolation. Delay times in the response to radiation, and the statistical variability in response have led to expression of the lethal dose in the form, for example, $LD_{50/60}$, meaning the dose is fatal to 50% of those exposed within 60 days. The *dose* itself requires a careful interpretation. One way of defining the *dose* is the free-field exposure, in roentgen units, for gamma or

■ **Table 25**

Median effective absorbed doses D_{50} and threshold doses D_{th} for exposure of different organs and tissues in the human adult to gamma photons at dose rates $\leq 0.06 \text{ Gy h}^{-1}$

Organ/Tissue	Endpoint	D_{50} (Gy)	D_{th} (Gy)
Skin	Erythema	6 ± 1	3 ± 1
	Moist desquamation	30 ± 6	10 ± 2
Ovary	Permanent ovulation suppression	3 ± 1	0.6 ± 0.4
Testes	Sperm count suppressed for 2 y	0.6 ± 0.1	0.3 ± 0.1
Eye lens	Cataract	3.1 ± 0.9	0.5 ± 0.5
Lung	Death ^a	70 ± 30	40 ± 20
	Vomiting	2 ± 0.5	0.5
	Diarrhea	3 ± 0.8	1
GI system	Death	15 ± 5	8
	Death	3.8 ± 0.6	1.8 ± 0.3

^aDose rate 0.5 Gy/h

Source: Scott and Hahn (1989)

X-rays. A second is the average absorbed dose to the whole body. A third is the *mid-line* absorbed dose, that is, the average absorbed dose near the abdomen of the body. For gamma rays and X-rays, the mid-line dose, in units of rads, is about two-thirds the free-field exposure, in units of roentgens. The evaluation by Anno et al. (1989) for the lethal doses of ionizing radiation are given in ► [Table 26](#). The effects of large doses below the threshold for lethality are summarized in NCRP Report 38 (1971) and by Anno et al. (1989). For extremely high doses (>500 Gy), death is nearly instantaneous, resulting from enzyme inactivation or possibly from immediate effects on the electrical response of the heart (Kathren 1985). Lesser, but still fatal doses, lead promptly to symptoms known collectively as the *prodromal syndrome*. The symptoms, which are expressed within a 48-h period are primarily gastrointestinal (e.g., nausea, diarrhea, cramps, and dehydration) and neuromuscular (e.g., fatigue, sweating, fever, headache, and hypotension). For high doses with potential survival, the prodromal stage is followed by a latent stage, a stage of manifest illness, and a recovery stage beyond 6–8 weeks post-exposure.

10.2 Hereditary Illness

In 1927, Hermann Muller discovered that fruit flies receiving high doses of radiation could produce offspring with genetic abnormalities. Subsequent animal and plant studies have demonstrated a nearly linear relationship between dose and mutation frequency, for doses as low as 3 mSv. However, there is almost no evidence of radiation-induced mutations in humans. Indeed, the only unequivocal evidence relates to chromosomal rearrangement in spermatoocytes. Nevertheless, animal studies clearly indicate that radiation can produce heritable mutational effects in the humans. Because radiation-induced mutation rates in humans are unknown, even for atom bomb survivors, estimation of risks to human populations are based largely on extrapolation of studies of radiation effects in other mammals, notably the mouse. The estimation of human hereditary risks from animal studies involve many assumptions, and the estimates turn out to be a very small fraction of the natural incidence of such illness, thereby, explaining why radiation-induced hereditary illness has not been observed in humans.

■ **Table 26**
Lethal doses of radiation

Lethality	Mid-line absorbed dose (Gy)
$LD_{5/60}$	2.0–2.5
$LD_{10/60}$	2.5–3.0
$LD_{50/60}$	3.0–3.5
$LD_{90/60}$	3.5–4.5
$LD_{99/60}$	4.5–5.5

10.2.1 Classification of Genetic Effects

► *Table 27* reports estimates of the natural incidence of human hereditary or partially hereditary traits causing serious handicap at some time during life. Inheritance of a deleterious trait results from mutation(s) in one or both maternal and paternal lines of germ cells. Here a mutation is either a microscopically visible chromosome abnormality or a submicroscopic disruption in the DNA making up the individual genes within the chromosomes. Mutations take place in both germ cells and somatic cells, but only mutations in germ cells are of concern here.

Regularly inherited traits are those whose inheritance follows Mendelian laws. These are autosomal dominant, X-linked, and recessive traits. Examples of autosomal dominant disorders, that is, those which are expressed even when the person is heterozygous for that trait, are certain types of muscular dystrophy, retinoblastoma, Huntington's chorea, and various skeletal malformations. Examples of recessive disorders, that is, those which are expressed only when the individual is homozygous for the trait, include Tay–Sachs disease, phenylketonuria, sickle-cell anemia, and cystic fibrosis. X-linked disorders, that is, those traits identified with genes in the X chromosome of the X–Y pair and which are expressed mostly in males, include hemophilia, color blindness, and one type of muscular dystrophy. In the X–Y chromosome pair, otherwise recessive genetic traits carried by the “stronger” maternal X chromosome are expressed as though the traits were dominant. *Chromosome abnormalities* are of two types:

■ **Table 27**

Genetic risks from continuing exposure to low-LET, low-dose, or chronic radiation as estimated by the BEIR and UNSCEAR committees on the basis of a doubling-dose of 1 Gy

Type of Disorder	Per million progeny		
	Natural frequency	Cases/Gy in first generation	Cases/Gy in second generation ^a
Mendelian autosomal			
Dominant and X-linked	16,500	750–1500	1300–2500
Recessive	7,500	0	0
Chromosomal	4,000	^b	^b
Irregularly inherited traits			
Chronic multifactorial	650,000	250–1200	250–1200
Congenital abnormalities	60,000	2000	2400–3000
Total	738,000	3000–4700	3950–6700
Total risk (% of baseline)		0.41–0.64	0.53–0.91

^aRisk to the second generation includes that to the first except for congenital abnormalities for which it is assumed that between 20% and 50% of the abnormal progeny in the first generation may transmit the damage to the second post-radiation generation, the remainder causing lethality.

^bAssumed to be included with Mendelian diseases and congenital abnormalities.

Source: UN (2001); adopted by NAS (2006) and ICRP (2007)

those involving changes in the numbers of chromosomes and those involving the structure of the chromosomes themselves. Down syndrome is an example of the former. With natural occurrence, numerical abnormalities are more common. By contrast, radiation-induced abnormalities are more frequently structural abnormalities.

There is a very broad category comprising what are variously called *irregularly inherited traits*, multifactorial diseases, or traits of complex etiology. This category includes abnormalities and diseases to which genetic mutations doubtlessly contribute, but which have inheritances much more complex than result from chromosome abnormalities or mutations of single genes. They are exemplified by inherited predispositions for a wide variety of ailments and conditions. One or more other multifactorial disorders, including cancer, are thought to afflict nearly all persons sometime during life; however, the mutational components of these disorders are unknown even as to orders of magnitude (NAS 1990). Also included in [Table 27](#) is a subgroup of irregularly inherited traits identified as *congenital abnormalities*. These are well-identified conditions such as spina bifida and cleft palate, with reasonably well-known degrees of heritability.

10.2.2 Estimates of Hereditary Illness Risks

[Table 27](#) also summarizes the 2001 UNSCEAR genetic risk estimates. The results are for low LET radiation (quality factor $Q = 1$); thus, the absorbed dose and dose equivalent are the same. These estimates are based on a population-averaged *gonad*-absorbed dose of 1 Gy (100 rad) to the reproductive population which produce one-million live-born. Because of the linearity of the dose-effect models used, these estimated hereditary risks are the same whether the gonad dose is received in a single occurrence or over the 30-year reproduction interval. The population for these results is assumed static in number, so that one million born into one generation replace one million in the parental generation.

Data in [Table 27](#) give the expected number of genetic illness cases appearing in the first and second generations, each receiving radiation exposure. Except as indicated, cases in the second generation include the new cases from exposure of the first generation plus cases resulting from exposure of the previous generation, for example, 550–1000 cases of autosomal dominant and X-linked class and no cases of the autosomal recessive class. The ICRP (2007) suggests overall risk coefficients for heritable disease up to the second generation as 0.002 Sv^{-1} for the whole population and 0.001 Sv^{-1} for adult workers.

10.3 Cancer Risks from Radiation Exposures

A large body of evidence leaves no doubt that ionizing radiation, when delivered in high doses, is one of the many causes of cancer in the human. Excess cancer risk cannot be observed at doses less than about 0.2 Gy and, therefore, risks for lower doses cannot be determined directly (UN 1988). At high doses, in almost all body tissues and organs, radiation can produce cancers that are indistinguishable from those occurring naturally. Consequently, radiation-induced cancer can be inferred only from a statistical excess above natural occurrence. [Table 28](#) summarizes natural incidence and mortality for the male and female. ICRP Report 103 (2007) provides comprehensive age and gender dependent incidence and mortality data for Euro-American and Asian populations.

■ **Table 28**

Annual cancer incidence and death rates per 100,000 population in the 2002 United States population

Primary site	Incidence per 10 ⁵ per year		Deaths per 10 ⁵ per year	
	Males	Females	Males	Females
Leukemia	14.6	8.8	10.1	5.7
Lymphoma	25.1	17.9	10.2	6.5
Respiratory	94.7	55.8	76.2	42.2
Digestive	106.9	71.4	59.1	35.9
Breast		124.9		25.5
Genital	167.3	48.9	28.6	16.7
Urinary	56.3	19.1	13.9	5.3
Other	80.6	58.2	41.8	24.9
Total	545.5	405.0	239.9	162.7

Source: HHS (2005)

There is a large variation in the sensitivity of tissues and organs to cancer induction by radiation. For whole-body exposure to radiation, solid tumors are of greater numerical significance than leukemia. The excess risk of leukemia appears within a few years after radiation exposure and largely disappears within 30 years after exposure. By contrast, solid cancers, which occur primarily in the female breast, the thyroid, the lung, and some digestive organs, characteristically have long latent periods, seldom appearing before 10 years after radiation exposure and continuing to appear for 30 years or more. It is also apparent that age at exposure is a major factor in the risk of radiation-induced cancer. Various host or environmental factors influence the incidence of radiation-induced cancer. These may include hormonal influences, immunological status, and exposure to various oncogenic agents.

10.3.1 Estimating Radiogenic Cancer Risks

Our knowledge about radiation-induced cancer is based on epidemiological studies of people who have received large radiation doses. These populations include atomic bomb survivors, radiation therapy patients, and people who have received large occupational doses. Some 91,000 survivors of the atomic weapon attacks on Hiroshima and Nagasaki and their offspring remain under continuing study, and much of our knowledge about radiation-induced cancer derives from this group. Occupational groups include medical and industrial radiologists and technicians, women who ingested large amounts of radium while painting instrument dials during World War I, and miners exposed to high concentrations of radon and its daughter radionuclides. Finally, radiation therapy patients have provided much information on radiation carcinogenesis. These include many treated with X-rays between 1930 and 1950 for severe spinal arthritis, Europeans given ²²⁶Ra injections, and many women given radiation therapy for cervical cancer.

10.4 The Dose and Dose-Rate Effectiveness Factor

Assessment of cancer risks from radiation exposure is concerned primarily with exposures of population groups to low doses at low dose rates. As just indicated, however, there is little choice but to base risk estimates on consequences of exposures at high doses and dose rates. Furthermore, organizations such as the ICRP and the NCRP have endorsed, and government organizations have agreed, to base risk estimates on a linear no-threshold relationship between cancer risk and radiation dose. An exception applies to radiation-induced leukemia, for which a quadratic, no-threshold relationship has been adopted. How does one reconcile low-dose risk estimates based on high-dose data? The answer is addressed in [Fig. 47](#). Symbols display a limited base of data for high doses and dose rates. A central curved line displays what may be the true dose response (say a linear quadratic relationship). The upper straight line, with slope α_H is the linear, no-threshold approximation for the high-dose data. The lower straight line, with slope α_L is tangent to the true response curve in the limit of low dose and low-dose rate, conditions allowing for partial repair of radiation damage. Risks at low doses and dose rates, if computed on the basis of α_H , need to be corrected by division by the ratio α_H/α_L defined as the *DDREF*, the *dose and dose rate correction factor*.

10.4.1 Dose-Response Models for Cancer

Evidence is clear that absorbed doses of ionizing radiation at levels of 1 Gy or greater may lead stochastically to abnormally high cancer incidence in exposed populations. However, there is no direct evidence that chronic exposure to low levels of ionizing radiation may likewise lead to abnormally high cancer incidence. Risk estimates for chronic, low-level exposure requires extrapolation of high-dose and high-dose-rate response data to low doses. Methods used for extrapolation are often controversial, any one method being criticized by some as overpredictive and by others as underpredictive.

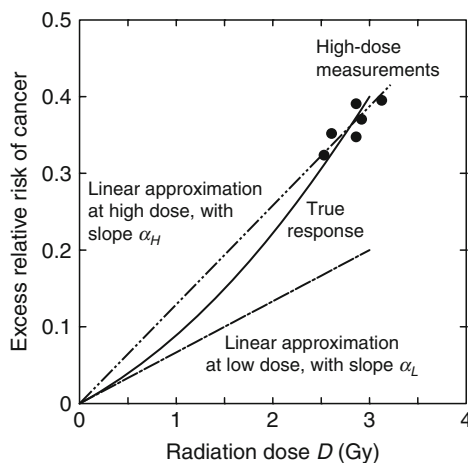


Figure 47
Basis for the dose and dose-rate effectiveness factor

Current risk estimates for cancer have as the basic elements dose responses that are functions of the cancer site or type, the age a_o (y) at exposure, the age a (y) at which the cancer is expressed or the age at death, and the sex s of the subject. The radiogenic cancer risk is expressed as

$$\text{risk} = R_o(s, a) \times EER(D, s, a_o, a). \quad (172)$$

Here, R_o is the natural cancer risk as a function of sex, site, and age at cancer expression, for both incidence and mortality; and EER is the *excess relative risk* function that is determined by fitting a model to observed radiogenic cancer incidence or mortality for cancer at a particular site. For example, the excess relative risk for all solid cancer, except thyroid and nonmelanoma skin cancer, is expressed as (NAS 2006)

$$ERR(D, s, a_o, a) = \beta_s D \exp[e^* \gamma] (a/60)^\eta, \quad (173)$$

in which D is the dose in Sv. In this particular model, the empirical parameter $e^* = (a_o - 30)/10$ for $a_o < 30$ and zero for $a_o \geq 30$. Parameters β_s , γ , and η depend on whether the estimate is for incidence or mortality. For example, for cancer incidence, $\gamma = -0.30$, $\eta = -1.4$, and $\beta_s = 0.33$ for males and 0.57 for females.

To use (172), the natural risk $R_o(s, a)$ for the type of cancer of concern must be known. Data for natural risk are available, but are too extensive to be presented here. They may be found in publications of the Centers for Disease Control (HHS 2005) and on-line at <http://www.cdc.gov/cancer/ncpr/uscs> or <http://seer.cancer.gov/statistics>. For example, US death rates per 100,000 US males, for all races and all cancer sites combined increase from 2.1 for infants to 11.3 at age 30–34, and 520 at age 60–64. For females, the corresponding rates are 1.6, 13.8, and 382, respectively.

It should be emphasized that, in examining these risks of cancer from radiation exposure, one should keep in mind the overall or natural risk of cancer. As indicated in **► Table 28**, two persons per thousand in the United States die each year from cancer. As will be seen in the next section, the overall lifetime risk of cancer mortality is about one in five for males and about one in six for females.

10.4.2 Average Cancer Risks for Exposed Populations

The BEIR-VII Committee of the National Academy of Sciences (NAS 2006) made various estimates of the risk of excess cancer incidence and mortality resulting from low-LET (gamma-ray) exposures. These risks are summarized in **► Table 29** by sex and by age at exposure. Although the data are for conditions of low dose and dose rate, they were generated in large part from cancer incidence and mortality experienced by survivors of atomic weapons at Hiroshima and Nagasaki. At lower doses and dose rates, risks are somewhat less because biological repair mechanisms can repair a greater fraction of the genetic damage produced by the radiation. This effect is accounted for in risk estimates for leukemia, which are based on a linear-quadratic dose–response model. For solid cancers, risks have been modified by application of a dose and dose-rate effectiveness factor, namely, by dividing high-dose and dose-rate data by the DDREF value of 1.5. The ICRP (1991, 2007) continues to recommend a DDREF value of 2.0.

The BEIR-VII Committee also calculated risks to the US population under three low-LET exposure scenarios: (1) single exposure to 0.1 Gy, (2) continuous lifetime exposure to 1 mGy

■ **Table 29**

Excess lifetime cancer incidence and mortality for the US population by age at exposure for a whole-body dose of 0.1 Gy (10 rad) from low LET radiation to populations of 10^5 males or females

	Age at exposure (years)								
	0	10	20	30	40	50	60	70	80
Females									
Incidence									
Leukemia	185	86	71	63	62	62	57	51	37
All solid	4592	2525	1575	1002	824	678	529	358	177
Mortality									
Leukemia	53	53	51	51	52	54	55	52	38
All solid	1717	1051	711	491	455	415	354	265	152
Males									
Incidence									
Leukemia	237	120	96	84	84	84	82	73	48
All solid	2326	1325	881	602	564	507	407	270	126
Mortality									
Leukemia	71	71	67	64	67	71	73	69	51
All solid	1028	641	444	317	310	289	246	181	102

Source: based on (NAS 2006)

per year, and (3) exposure to 10 mGy per year from age 18 to age 65. Results are summarized in ► [Table 30](#). The first scenario is representative of accidental exposure of a large population (the 1999 US population), the second of chronic exposure, and the third of occupational exposure. For example, for leukemia mortality, with 95% confidence limits (not given in ► [Table 30](#)), for a single exposure of the US population to 0.1 Gy, the risk per 100,000 is 70 (20–220) for the male and 50 (10–190) for the female. For nonleukemia mortality per 100,000 fatalities are 410 (200–830) for the male and 610 (300–1200) for the female. For this case, the total low-dose cancer mortality risk for the US population is $0.5 \times (480 + 660) / (0.1 \text{ Gy} \times 10^5) = 0.057$ per Gy, which can be rounded to 0.05 per Gy, or 5×10^{-4} per rem. This risk should be used as an overall cancer risk factor for environmental exposures, that is, small exposures obtained at low dose rates. The ICRP (2007) nominal risk recommendations are 0.055 Sv^{-1} for the whole population and 0.041 Sv^{-1} for adult workers.

10.5 Radiation Protection Standards

It was recognized near the beginning of the twentieth century that standards were needed to protect workers and patients from the harmful consequences of radiation. Many sets of standards, based on different philosophies, have been proposed by several national and international

■ Table 30

Excess cancer incidence and mortality per 100,000 males and 100,000 females in the stationary US population for three low-dose exposure scenarios

Cancer Type	Cases per 10 ⁵		Deaths per 10 ⁵	
	Males	Females	Males	Females
Single Exposure to 0.1 Gy (10 rad):				
Radiation Induced:				
leukemia	100	70	70	50
nonleukemia	800	1300	410	610
total	900	1370	480	660
Natural Expectation:				
leukemia	830	590	710	530
nonleukemia	45500	36900	22100	17500
total	46330	37490	22810	18030
Continuous Lifetime Exposure to 1 mGy (100 mrad) per year:				
Radiation Induced:				
leukemia	67	51	47	38
nonleukemia	554	968	285	459
total	621	1019	332	497
Continuous Exposure to 10 mGy (1 rad) per year from age 18 to 65:				
Radiation Induced:				
leukemia	360	270	290	220
nonleukemia	2699	4025	1410	2169
total	3059	4295	1700	2389

Source: based on (NAS 2006)

standards groups. The earliest standards were based on the concept of *tolerable doses* below which no ill effects would occur. This was replaced in 1948 by the National Council on Radiation Protection and Measurements (NCRP) in the United States which introduced standards based on the idea of *permissible doses*, that is, a dose of ionizing radiation which was not expected to cause appreciable body injury to any person during his or her lifetime.

10.5.1 Risk-Related Dose Limits

Today it is understood that low-level radiation exposure leads to stochastic hazards and that modern radiation standards should be based on probabilistic assessments of radiation hazards.

This new line of thinking is exemplified by a 1972 report to the ICRP by the Task Group on Dose Limits. Key portions of the report are summarized as follows. It must be noted that the report is unpublished and not necessarily reflective of the official ICRP position. The tentative dose limits examined in the report were not based on explicit balancing of risks and benefits, then thought to be an unattainable ideal. Rather, they were based on the practical alternative of identifying acceptable limits of occupational radiation risk in comparison with risks in other occupations generally identified as having a high standard of safety and also having risks of environmental hazards generally accepted by the public in everyday life.

Linear, no-threshold dose-response relationships were assumed for carcinogenic and genetic effects, namely, a 1×10^{-4} probability per rem whole-body dose equivalent for malignant illness or a 4×10^{-5} probability per rem for hereditary illness within the first two generations of descendants (ICRP 1977). For other radiation effects, absolute thresholds were assumed.

To illustrate the reasoning for risk-based limits, consider the occupational whole-body dose-equivalent limit of 5 rem/y. For occupational risks, it was observed that “occupations with a high standard of safety” are those in which the average annual death rate due to occupational hazards is no more than 100 per million workers. An *acceptable risk* was taken as 50 per million workers per year, or a 40-year occupational lifetime risk of 2 fatalities per 1000 workers, that is, 0.002. It was also observed that in most facilities in which radiation may expose workers, the average annual doses are about 10 percent of the doses of the most highly exposed individuals, with the distribution highly skewed toward the lower doses. To ensure an *average* lifetime risk limit of 0.002, an upper limit of 10 times this value was placed on the lifetime risk for any one individual. The annual whole-body dose-equivalent limit for stochastic effects was thus taken as $(10 \times 0.002)/(40 \text{ y} \times 0.01 \text{ malignancies/Sv}) = 0.05 \text{ Sv}$ (5 rem) per year. Similar reasoning is used to set public dose limits and limits for nonstochastic effects (Shultis and Faw 2008).

10.5.2 The 1987 NCRP Exposure Limits

The concept of “risk-based” or “comparable-risk” dose limits provides the rationale for the 1977 ICRP and the 1987 NCRP recommendations for radiation protection, and which serve as the present basis for the US radiation protection standards. A summary of these dose limits is given in [▶ Table 31](#).

Acknowledgments

The authors of this chapter gratefully acknowledge the guidance and support of their colleagues and mentors in the field of radiation shielding and radiation protection. The late Arthur Chilton, our colleague and friend, will be known to readers of this chapter for his breadth of interest and experience in radiation shielding. He was the coauthor of and the inspiration for our first book on radiation shielding. Of the many who taught us, we particularly acknowledge Lewis Spencer, Martin Berger, Herbert Goldstein, and Norman Schaeffer. We acknowledge the American Nuclear Society too for their continuing publication of our textbooks on radiation shielding and radiological assessment, from which much of the material in this chapter has been taken.

■ **Table 31**
The 1987 NCRP recommendations for exposure limits

Type of Dose	mSv	rem
<i>Occupational exposures (annual):</i>		
1. Limit for stochastic effects	50	5
2. Limit for nonstochastic effects:		
a. Lens of the eye	150	15
b. All other organs	500	50
3. Guidance: cumulative exposure age (y) ×	10	1
<i>Public exposures (annual):</i>		
1. Continuous or frequency exposure	1	0.1
2. Infrequent exposure	5	0.5
3. Remedial action levels	5	0.5
4. Lens of the eyes, skin and extremities	50	5
<i>Embryo–fetus exposure:</i>		
1. Effective-dose equivalent	5	0.5
2. Dose-equivalent limit in a month	0.5	0.05
<i>Negligible individual risk level (annual):</i>		
1. Effective-dose equivalent per source or practice	0.01	0.001

Source: NCRP (1987)

References

- Albert RD, Welton TA (1950) A simplified theory of neutron attenuation and its application to reactor shield design. USAEC Report WAPD-15 (Del.), Westinghouse Electric Corporation, Atomic Power Division, Pittsburgh, PA
- Alsmiller RG Jr, Mynatt RR, Barish J, Engle WW Jr (1969) Shielding against neutrons in the energy range 50 to 400 MeV. Nucl Instrum Methods 72:213
- Anno GH, Baum SJ, Withers HR, Young RW (1989) Symptomatology of acute radiation effects in humans after exposure to doses of 0.5–30 Gy. Health Phys 56:821–838
- ANSI/ANS-6.1.1-1977, American National Standard (1977) Neutron and gamma-ray flux-to-dose-rate factors. American Nuclear Society, La Grange Park, IL
- ANSI/ANS-6.6.1-1987, American National Standard (1987) Calculation and measurement of direct and scattered gamma radiation from LWR nuclear power plants. American Nuclear Society, La Grange Park, IL
- ANSI/ANS-6.4.3-1991, American National Standard (1991) Gamma ray attenuation coefficients and buildup factors for engineering materials. American Nuclear Society, La Grange Park, IL (Available as Data Library Collection DLC-129/ANS-643 from the Radiation Shielding Information Center, Oak Ridge National Laboratory, Oak Ridge, TN)
- ANSI/ANS-5.1-2005, American National Standard (2005) Decay heat power in light water reactors. American Nuclear Society, La Grange Park, IL
- ANSI/ANS-6.4-2006, American National Standard (2006) Nuclear analysis and design of concrete

- radiation shielding for nuclear power plants. American Nuclear Society, La Grange Park, IL
- ANSI/ANS-6.4.2-2006 (2006) Specification for radiation shielding materials. American Nuclear Society, La Grange Park, IL
- Archer BR, Fewell TR, Conway BJ, Quinn PW (1994) Attenuation properties of diagnostic X-ray shielding materials. *Med Phys* 21:1499–1507
- Archer BR, Thornby JL, Bushong SC (1983) Diagnostic X-ray shielding design based on an empirical model of photon attenuation. *Health Phys* 44:507–517
- Artigas R, Hungerford HE (1969) A numerical treatment of the attenuation of neutrons by air ducts in shields. *Nucl Sci Eng* 36:295
- Avery AF, Bendall DE, Butler J, Spinney KT (1960) Methods of calculation for use in the design of shields for power reactors. Report AERE-R 3216, Atomic Energy Research Establishment, Oxfordshire, England
- Baran A, Grun M (1990) ALBEDO/ALBEZ: PC-programs for the calculation of the attenuation of radiation in single and double bends. NUKEM GmbH informal document (RSIC Code Collection CCC-555), Alzenau, Germany
- Bendall DE (1962) RASH D-A mercury programme for neutron shielding calculations. Report AEEW-M 261, Atomic Energy Weapons Establishment, Winfrith, Dorset, England
- Blizard EP (1962) Shield optimization with respect to weight. In: Blizard EP (ed) *Reactor handbook, Part B: shielding*, 2nd edn, vol III. Interscience, New York
- Blizard EP, Abbott LS (eds) (1962) *Reactor handbook, Part B: shielding*, 2nd edn, vol III. Interscience, New York
- Blizard EP, Foderaro A, Goussev NG, Kovaiev EE (1968) Extended radiation sources (point kernel integrations). In: Jaeger RG (ed) *Engineering compendium on radiation shielding*, chap 6, vol I. Springer, New York
- Brockhoff RC, Shultis JK (2007) A new approximation for the neutron Albedo. *Nucl Sci Eng* 155:1–17
- Brockhoff RC, Shultis JK, Faw RE (1996) Skyshine line-beam response functions for 20- to 100-MeV photons. *Nucl Sci Eng* 123:282–288
- Broder DL, Kayurin Yu P, Kutrezov AA (1962) An iterative method for calculating gamma-ray buildup factors in multi-layer shields. *Sov J At Energy* 12:26–31
- Broder DL, Tsypin SG (1968) Attenuation in non-hydrogenous media. In: Jaeger RG (ed) *Engineering compendium on radiation shielding*, vol I. Springer, New York, p 322
- Brynjolfsson A (1975) Water. In: Jaeger RG (ed) *Engineering compendium on radiation shielding*, vol II. Springer, New York, p 288
- Bünemann D, Richter G (1968) Multilayered shields. In: Jaeger RG (ed) *Engineering compendium on radiation shielding*, vol I. Springer, New York, p 230
- Burrus WR (1968a) Random voids and lumps. In: Jaeger RG (ed) *Engineering compendium on radiation shielding*, vol I. Springer, New York, p 490
- Burrus WR (1968b) Regular geometric void shapes. In: Jaeger RG (ed) *Engineering compendium on radiation shielding*, vol I. Springer, New York, p 495
- Casper AW (1960) Modified fast neutron attenuation functions. USAEC Report XDC-60-276, General Electric Corporation, Atomic Products Division, Cincinnati, OH
- Chapman GT, Storrs CL (1955) Effective neutron removal cross sections for shielding. USAEC Report ORNL-1843 (AECD-3978), Oak Ridge National Laboratory, Oak Ridge, TN
- Chapman JM (1962) Computer calculation of dose rates in two-legged ducts using the Albedo concept. USAEC file number NP-13652 (TR-264), Naval Civil Engineering Laboratory, Port Hueneme, CA
- Chen MF, Faw RE (1994) Build-up factors for gamma rays obliquely incident on slab shields of concrete, iron and lead. *Radiat Protect Dosimetry* 51:27–33
- Chilton AB (1967) A modified formula for differential exposure Albedo for gamma rays reflected from concrete. *Nucl Sci Eng* 27:481–482
- Chilton AB (1971) Effect of material composition on neutron penetration of concrete slabs. Report 10425, National Bureau of Standards, Washington, DC
- Chilton AB (1977) Optimized Taylor parameters for concrete buildup factor data. *Nucl Sci Eng* 64:799–800
- Chilton AB (1979) Tschebycheff-fitted Berger coefficients for Eisenhower-Simmons gamma-ray buildup factors in ordinary concrete. *Nucl Sci Eng* 69:436–438
- Chilton AB, Davisson CM, Beach LA (1965) Parameters for C-H Albedo formula for Gamma rays reflected from water, concrete, iron, and lead. *Trans Amer Nucl Soc* 8:656
- Chilton AB, Eisenhower CM, Simmons GL (1980) Photon point source buildup factors for air, water, and iron. *Nucl Sci Eng* 73:97–107
- Chilton AB, Huddleston CM (1963) A semi-empirical formula for differential dose Albedo for gamma rays on concrete. *Nucl Sci Eng* 17:419

- Chilton AB, Shultis JK, Faw RE (1984) Principles of radiation shielding. Prentice Hall, Englewood Cliffs, NJ
- Claiborne HC, Schaeffer NM (1973) Shield design. In: Schaeffer NM (ed) Reactor shielding for nuclear engineers, USAEC, TID-25951. (Available from NTIS, U.S. Department of Commerce, Springfield, VA)
- Courtney JC (ed) (1975) A handbook of radiation shielding data. A Publication of the Shielding and Dosimetry Division of the American Nuclear Society, La Grange Park, IL
- Cristy M, Eckerman KF (1987) Specific absorbed fractions of energy at various ages from internal photon sources. Report ORNL/TM-8381 (6 vols), Oak Ridge National Laboratory, Oak Ridge, TN
- Dillman LT (1980) EDISTR – A computer program to obtain a nuclear data base for nuclear dosimetry. Report ORNL/TM-6689, Oak Ridge National Laboratory, Oak Ridge, TN
- Dunn WL, Yacout AM, O’Foghluda F, Riel G (1992) Gamma-Ray and neutron dose-equivalent buildup factors for infinite slabs. Nucl Sci Eng 110:134–156
- Dunn WW (1957) Transmission of fast neutrons through aluminum, iron and lead. Dissertation, Air Force Institute of Technology (Armed Services Technical Information Agency 124760)
- Eckerman KF, Westfall RJ, Ryman JC, Cristy M (1994) Availability of nuclear decay data in electronic form, including beta spectra not previously published. Health Phys 67:338–345. (Available as DLC-172, NUCDECAY Data Library, Radiation Shielding Information Center, Oak Ridge National Laboratory, Oak Ridge, TN)
- Eisenhauer CM, Simmons GL (1975) Point isotropic buildup factors in concrete. Nucl Sci Eng 46:263–270
- EPA (1986) A citizen’s guide to radon. Report OPA-86-004 of the U.S. Environmental Protection Agency and the Centers for Disease Control of the U.S. Department of Health and Human Services, U.S. Government Printing Office
- Evans RD (1955) The atomic nucleus. McGraw-Hill, New York
- Fano U, Spencer LV, Berger MJ (1959) Penetration and diffusion of X rays. In: Flügge S (ed) Handbuch der physik, vol 38/2. Springer, Berlin
- Faw RE, Shultis JK (1993a) Absorbed dose buildup factors in air for 10- to 100-MeV photons. Nucl Sci Eng 114:76–80
- Faw RE, Shultis JK (1993b) Radiological assessment. Prentice Hall, Englewood Cliffs, NJ
- Fewell TR, Shuping RE (1978) Handbook of mammographic X-ray spectra. HEW Publication (FDA) 79-8071, U.S. Department of Health, Education, and Welfare, Rockville, MD
- Fewell TR, Shuping RE, Hawkins KR Jr (1981) Handbook of computed tomography X-ray spectra. HHS Publication (FDA) 81-8162, U.S. Department of Health and Human Services, Rockville, MD
- Firestone RB et al (1996) Table of isotopes, 8th edn, the book and CD-ROM. Wiley, New York
- Foderaro A, Hall RJ (1981) Application of three-exponential representation of photon buildup factors to water. Nucl Sci Eng 78. (Data are also tabulated in Chilton, Shultis, and Faw (1984))
- Fournie EM, Chilton AB (1981) Gamma-ray buildup factors for concrete slab shields under slant incidence conditions. Nucl Sci Eng 77: 66–69
- Fröhner FH (1990) Evaluation of ^{252}Cf prompt fission neutron data from 0 to 20 MeV by Watt spectrum fit. Nucl Sci Eng 106:345–352
- Geiger KW, Van der Zwan L (1975) Radioactive neutron source spectra from $^{11}\text{B}(\alpha, n)$ cross section data. Nucl Instrum Methods 131:315
- George DC et al (1980) Delayed photon sources for shielding applications. Trans Am Nucl Soc 35:463
- Glasstone S, Sesonske A (1963) Nuclear reactor engineering. Van Nostrand, Princeton, NJ
- Goldstein H (1959) Fundamental aspects of reactor shielding. Addison-Wesley, Reading, MA (Reprinted by Johnson Reprint Corporation, New York, 1971)
- Goldstein H, Aronson R (1954) Effective removal cross sections – theory. React Sci Technol 4:149 (USAEC Report TID-2015)
- Goldstein H, Wilkins JE Jr (1954) Calculations of the penetrations of gamma rays, NDA/AEC Report NYO-3075, U.S. Government Printing Office, Washington, DC
- Gopinath DV, Subbaiah KV, Trubey DK (1987) Gamma-ray transport in a shield-tissue composite system and the buildup factor implications. Nucl Sci Eng 97:362–373
- GPO (1970) Radiological health handbook. U.S. Government Printing Office, Washington, DC
- Gronroos H (1968) Energy dependent removal cross-sections in fast neutron shielding theory. In: Jaeger RG (ed) Engineering compendium on radiation shielding, vol I. Springer, New York, p 305
- Grotenhuis M (1962) Lecture notes on reactor shielding. Report ANL-6000, Argonne National Laboratory, Argonne, IL
- Grove (1987) Engineering, MicroSkyshine user’s manual. Grove Engineering, Rockville, MD

- Gui AA, Shultis JK, Faw RE (1997a) Response functions for neutron skyshine analyses. *Nucl Sci Eng* 125:111–127
- Gui AA, Shultis JK, Faw RE (1997b) Neutron skyshine calculations with the integral line-beam method. *Nucl Sci Eng* 127:230–237
- Harima Y (1983) An approximation of gamma-ray buildup factors for two-layer shields. *Nucl Sci Eng* 85:45–79
- Harima Y (1986) An approximation of gamma-ray buildup factors by modified geometric progression. *Nucl Sci Eng* 83:299–309
- Harima Y, Hirayama H (1993) Detailed behavior of exposure buildup factor in stratified shields for plane-normal and point isotropic sources, including the effects of Bremsstrahlung and fluorescent radiation. *Nucl Sci Eng* 113: 367–378
- Harima Y, Sakamoto Y, Tanaka S, Kawai M (1986) Validity of the geometric progression gamma-ray buildup factors. *Nucl Sci Eng* 94:24–35
- Harima Y, Tanaka S, Sakamoto Y, Hirayama H (1991) Development of new gamma-ray buildup factors and applications to shielding calculations. *J Nucl Sci Technol* 28:74–78
- Hermann OW, Westfall RM (1995) ORIGEN-S: SCALE system module to calculate fuel depletion, actinide transmutation, fission product buildup and decay, and associated radiation source terms, Sec F7 of SCALE: a modular code system for performing standardized computer analyses for licensing evaluation, Report NUREG/CR-0200, Revision 5(draft), vol 2, Oak Ridge National Laboratory, Oak Ridge, TN. Reference data libraries are from J.C. Ryman, ORIGEN-S Data Libraries, Sec M6 of SCALE: a modular code system for performing standardized computer analyses for licensing evaluation, Report NUREG/CR-0200, Oak Ridge National Laboratory, Oak Ridge, TN, vol 3, Revision 5 (draft) 1995
- Hertel NE, Sweezy JE, Shultis JK, Warkentin JK, Rose ZJ (2005) A comparison of skyshine computational methods. *Radiat Protect Dosimetry* 116:525–533
- HHS (2005) U.S. Cancer Statistics, 2002 incidence and mortality, U.S. Cancer Statistics Working Group, U.S. Department of Health and Human Services, Center for Disease Control and Prevention and National Cancer Institute
- Hirayama H (1987) Exposure buildup factors of high-energy gamma rays for water, concrete, iron, and lead. *Nucl Technol* 77:60–67
- Hjärne L (1964) A user's manual for the N.R.N. shield design method, Report AE-145, AB Atomenergi, Stockholm
- Hubbell JH, Seltzer SM (2004) Tables of X-ray mass attenuation coefficients and mass energy-absorption coefficients, (version 1.4). Available online: <http://physics.nist.gov/xaamdi>, National Institute of Standards and Technology, Gaithersburg, MD. Accessed 2 Nov 2009
- Hungerford HE (1966) Shielding. In: Yevick JG, Amorosi A (eds) Fast reactor technology: plant design. MIT Press, Cambridge, MA
- Hungerford HE (1968) Problems in design of fast reactor shields. *Trans Amer Nucl Soc* 11:702
- ICRP (1977) Recommendations of the international commission on radiological protection. *Annals of the ICRP, Publication 26*, International commission on radiological protection, vol 1, no 3. Pergamon Press, Oxford
- ICRP (1984) Nonstochastic effects of ionizing radiation, Publication 41, International commission on radiological protection. Pergamon Press, Oxford
- ICRP (1987) Data for use in protection against external radiation. *Annals of the ICRP, Publication 51*, International commission on radiological protection, vol 17, no 2/3. Pergamon Press, Oxford
- ICRP (1991) 1990 recommendations of the international commission on radiological protection, *Annals of the ICRP, Publication 60*, International commission on radiological protection, vol 21, no 1–3. Pergamon Press, Oxford
- ICRP (1996) Coefficients for use in radiological protection. *Annals of the ICRP, Publication 74*, International commission on radiological protection, vol 26, no 3–4
- ICRP (2007) Recommendations of the ICRP, *Annals of the ICRP, Publication 103*, International commission on radiological protection, vol 37, no 2–4
- ICRU (1971) Radiation quantities and units. Report 19, International commission on radiation units and measurements, Washington, DC
- ICRU (1979) Average energy required to produce an ion pair. Report 31, International commission on radiation units and measurements, Washington DC
- ICRU (1988) Determination of dose equivalents from external radiation sources – Part 2. Report 43, International commission on radiation units and measurements, Bethesda, MD
- ICRU (1992) Phantoms and computational models in therapy, diagnosis and protection. Report 48, International commission on radiation units and measurements, Bethesda, MD
- Jaeger RG (ed) (1968) Engineering compendium on radiation shielding. *Shielding fundamentals and methods*, vol I. Springer, New York

- Jaeger RG et al (eds) (1970) *Engineering compendium on radiation shielding. Shield design and engineering*, vol III. Springer, New York
- Jaeger RG et al (eds) (1975) *Engineering compendium on radiation shielding. Shielding materials*, vol II. Springer, New York
- Keepin GR (1965) *Physics of nuclear kinetics*. Addison-Wesley, Reading, MA
- Keriakes JG, Rosenstein M (1980) *Handbook of radiation doses in nuclear medicine and diagnostic X ray*. CRC Press, Boca Raton, FL
- Kitazume M (1965) Some considerations of buildup factors in γ ray penetration for multiple layers. *Nippon Genshiryoku Gakkaishi* 7:496
- Knoll GF (1989) *Radiation detection and measurement*, 2nd edn. Wiley, New York
- Kocher DC (1981) *Radioactive decay data tables. DOE/TIC-11026*, Technical Information Center, U.S. Department of Energy, Washington, DC
- Kramer R, Zankl M, Williams G, Drexler G (1982) The calculation of dose from external photon exposures using reference human phantoms and Monte Carlo methods, Part I: the male (Adam) and female (Eva) adult mathematical phantoms. Report GSF-Bericht S-885, Gesellschaft für Umweltforschung, Munich (Reprinted 1986)
- LaBaue RJ, England TR, George DC, Maynard CW (1982) Fission product analytic impulse source functions. *Nucl Technol* 56:322-339
- Lamarsh JR (1966) *Introduction to nuclear reactor theory*. Addison-Wesley, Reading, MA
- Lampley CM, Andrews MC, Wells MB (1988) The SKYSHINE-III procedure: calculation of the effects of structure design on neutron, primary gamma-ray and secondary gamma-ray dose rates in air. RRA T8209A (RSIC Code Collection CCC-289), Radiation Research Associates, Fort Worth, TX
- Langham WH (ed) (1967) *Radiobiological factors in manned space flight*. Report of the Space Radiation Study Panel, National Academy of Sciences, National Research Council, Washington, DC
- LeDoux JC, Chilton AB (1959) Gamma-ray streaming through two-legged rectangular ducts. *Nucl Sci Eng* 11:362-368
- Légaré JM, Carrieres PE, Manseau A, Bibeau C, Robert J, Robidoux N (1977) Blindage contre les grands champs de rayons X primaires et diffusés des appareils triphasés au moyen de panneaux de verre, de gypse et de plomb acoustique. *Radio-protection* 13:79-95
- Leimdorfer M (1968) The backscattering of photons. In: Jaeger RG (ed) *Engineering compendium on radiation shielding*, vol I. Springer, New York
- Maerker RE, Muckenthaler FJ (1965) Calculation and measurement of the fast-neutron differential dose Albedo for concrete. *Nucl Sci Eng* 22:455
- Mooney LG, Schaeffer NM (1973) Shield heating, air transport shield materials, and shield optimization. In: Schaeffer NM (ed) *Reactor shielding for nuclear engineers*, USAEC, TID-25951. Available from NTIS, U.S. Department of Commerce, Springfield, VA
- NAS, National Research Council, Advisory Committee on the Biological Effects of Ionizing Radiations (1990) Health effects of exposure to low levels of ionizing radiation. National Academy of Sciences, Washington, DC. (The BEIR-V Report)
- NCRP (1971a) Basic radiation protection criteria. NCRP Report 39, National Council on Radiation Protection and Measurements, Washington, DC
- NCRP (1971b) Protection against neutron radiation, Recommendations of the National Council on Radiation Protection and Measurements. Report 38, National Council on Radiation Protection and Measurements, Washington, DC
- NCRP (1976) Structural shielding design and evaluation for medical use of X rays and gamma rays of energies up to 10 MeV. Report 49, National Council on Radiation Protection and Measurements, Washington, DC
- NCRP (1977) Radiation protection design guidelines for 0.1-100 MeV Particle accelerator facilities. NCRP Report 51, National Council on Radiation Protection and Measurements, Washington, DC
- NCRP (1984) Neutron contamination from medical accelerators. Report 79, National Council on Radiation Protection and Measurements, Bethesda, MD
- NCRP (1987) Radiation exposure of the U.S. population from consumer products and miscellaneous sources. Report 95, National Council on Radiation Protection and Measurements, Washington, DC
- NCRP (1989) Medical X-ray, electron beam, and gamma-ray Protection for energies up to 50 MeV. Report 102, National Council on Radiation Protection and Measurements, Bethesda, MD
- NCRP (1993) Recommendations on limits for exposure to ionizing radiation. Report 116, National Council on Radiation Protection and Measurements, Bethesda, MD
- NCRP (2004) Structural shielding design for medical X-ray imaging facilities. Report 147, National Council on Radiation Protection and Measurements, Bethesda, MD (Rev 2005)

- Peele RW, Maienschein FC (1970) The absolute spectrum of photons emitted in coincidence with thermal-neutron fission of Uranium-235. ORNL-4457, Oak Ridge National Laboratory, Oak Ridge, TN
- Peterson EG (1962) MAC – a bulk shielding code. USAEC Report HW-73381, Hanford Atomic Products Operation, Hanford, WA
- Pochin E (1983) Nuclear radiation risks and benefits. Clarendon Press, Oxford
- Reilly D, Ensslin N, Smith H Jr, Kreiner S (1991) Passive nondestructive assay of nuclear materials. NUREG/CR-5550, U.S. Nuclear Regulatory Commission, Washington, DC
- Rockwell T, III (ed) (1956) Reactor shielding design manual. D Van Nostrand, Princeton, NJ
- Roussin RW, Alsmiller RG Jr, Barish J (1973) Calculations of the transport of neutrons and secondary gamma-rays through concrete for incident neutrons in the energy range 15 to 75 MeV. Nucl Eng Des 24:2
- Roussin RW, Schmidt FAR (1971) Adjoint Sn calculations of coupled neutron and gamma-ray transport calculations through concrete slabs. Nucl Eng Des 15:319
- Roussin RW, Weisbin CR, White JE, Green NM, Wright RQ, Wright JB (1980) VITAMIN-C: the CRT processed multigroup cross section library for neutronics studies. Report ORNL/RSIC-37 (ENDF-296), Radiation Shielding Information Center, Oak Ridge National Laboratory, Oak Ridge, TN
- RSIC (1991) ORIGEN 2.1: isotope generation and depletion code matrix exponential method. Code Package CCC-371, Radiation Shielding Information Center, Oak Ridge National Laboratory, Oak Ridge, TN
- Schaeffer NM (ed) (1973) Reactor shielding for nuclear engineers. USAEC, TID-25951. Available from NTIS, U.S. Department of Commerce, Springfield, VA
- Scott BR, Hahn FF (1989) Early occurring and continuing effects. In: Health effects models for nuclear power plant accident consequence analysis – low LET radiation, Part II: scientific bases for health effects models. Report NUREG/CR-4214, Rev. 1, Part II, U.S. Nuclear Regulatory Commission
- Selph WE (1973) Albedos, ducts and voids. In: Schaeffer NM (ed) Reactor shielding for nuclear engineers, TID 25951, Chap 7. National Technical Information Service, U.S. Department of Commerce, Springfield, VA
- Shin K, Hirayama H (1994) A new approximating model for gamma-ray buildup factors of stratified shields. Nucl Sci Eng 118:91–102
- Shin K, Hirayama H (1995) Approximating model for multilayer gamma-ray buildup factors by transmission matrix method: application to point isotropic source geometry. Nucl Sci Eng 120:211–222
- Shue S (1994) Calculating specific absorbed fractions using finite-medium buildup factors. M.S. Thesis, Nuclear Engineering Department, Kansas State University, Manhattan, KS
- Shue SL, Faw RE, Shultis JK (1998) Thermal-neutron intensities in soils irradiated by fast neutrons from point sources. Chem Geol 144:47–61
- Shultis JK (2000) Hybrid Skyshine calculations for complex neutron and gamma-ray sources. Nucl Sci Eng 136:294–304
- Shultis JK, Faw RE (1987) Improved line-beam response functions for the MicroSkyshine method. Report 189, Engineering Experiment Station, Kansas State University, Manhattan, KS
- Shultis JK, Faw RE (1994) Extensions to the integral line-beam method for gamma-ray Skyshine analyses, SAND94-2019, Sandia National Laboratory, Albuquerque, NM
- Shultis JK, Faw RE (2000) Radiation shielding. American Nuclear Society, La Grange Park, IL
- Shultis JK, Faw RE (2008) Fundamentals of nuclear science and engineering, 2nd edn. CRC Press, Boca Raton, FL
- Shultis JK, Faw RE, Bassett MS (1991) The integral line-beam method for gamma Skyshine analyses. Nucl Sci Eng 107:228–245
- Shure KJ, O'Brien KA, Rothberg DM (1969) Neutron dose rate attenuation by iron and lead. Nucl Sci Eng 35:371
- Shure K, Wallace OJ (1988) Taylor parameters for gamma-ray buildup factors in the proposed American National Standard. Report WAPD-TM-1628, Bettis Atomic Power Laboratory, West Mifflin, PA. (See data tabulation in ANSI/ANS (1991))
- Simmons GL, Albert TE, Gritzner ML (1979) The SAI/EPRI Albedo information library. Report SAI-013-79-525-LJ (RSIC Code Collection DLC-57), Science Applications, La Jolla, CA
- Simon A, Clifford CE (1956) The attenuation of neutrons by air ducts in shields. Nucl Sci Eng 1:156–166
- Simpkin DJ (1987a) A general solution to the shielding of medical X and γ rays by the NCRP Report 49 methods. Health Phys 52:431–436
- Simpkin DJ (1987b) Shielding requirements for mammography. Health Phys 53:267–279
- Simpkin DJ (1989) Shielding requirements for constant potential diagnostic X-ray beams determined by a Monte Carlo calculation. Health Phys 56:151–154

- Simpkin DJ (1990) Transmission of scatter radiation from computed tomography (ct) scanners determined by a Monte carlo calculation. *Health Phys* 58:363–367
- Simpkin DJ (1995) Transmission data for shielding diagnostic X-ray facilities. *Health Phys* 68:704–709
- Song YT (1965) Fast neutron streaming through two-legged concrete ducts. Report AD-457746 (TR-354), Naval Civil Engineering Laboratory, Port Hueneme, CA
- Spencer LV (1962) Structure shielding against fallout radiation from nuclear weapons. NBS Monograph 42, National Bureau of Standards, Washington, DC
- Stedry MH, Shultis JK, Faw RE (1996) Effect of an overhead shield on gamma-ray Skyshine. *Nucl Sci Eng* 123:289–294
- Stevens PA, Trubey DK (1968) Methods for calculating neutron and gamma ray attenuation. In: Weapons radiation shielding handbook, chap 3. USAEC Report DASA-1892-3, Oak Ridge National Laboratory, Oak Ridge, TN
- Su M, Jiang S (1989) Gamma-ray buildup factors for a point isotropic source in stratified spherical shields. *Nucl Sci Eng* 102:64–73
- Subbaiah KV, Natarajan A (1987) Effect of fluorescence in deep penetration of gamma rays. *Nucl Sci Eng* 96:330–342
- Subbaiah KV, Natarajan A, Gopinath DV, Trubey DK (1982) Effect of fluorescence, Bremsstrahlung, and annihilation radiation on the spectra and energy deposition of gamma rays in bulk media. *Nucl Sci Eng* 81:172–195
- Swanson WP (1979) Radiological safety aspects of the operation of electron linear accelerators. Report 188, International Atomic Energy Agency, Vienna
- Takeuchi K, Tanaka S (1984) Buildup factors of gamma rays including Bremsstrahlung and annihilation radiation for water, concrete, iron, and lead. *Nucl Sci Eng* 87:478–489
- Takeuchi K, Tanaka S, Kinno M (1981) Transport calculations of gamma rays, including Bremsstrahlung by the discrete ordinates code PALLAS. *Nucl Sci Eng* 78:272–283
- Tanaka M, Takeuchi K (1986) Detailed investigation of the buildup factors and spectra for point isotropic gamma-ray sources in the vicinity of the k-edge in lead. *Nucl Sci Eng* 93:376–385
- Taylor JJ (1951) Report WAPD-23, Westinghouse Corporation, Pittsburgh, PA. (See Rockwell (1956) for a summary of this technique)
- Tsypin SG, Kukhtevich VI (1968) Removal theory. In: Jaeger RG (ed) Engineering compendium on radiation shielding, vol I. Springer, New York
- UN (1988) Sources, effects and risks of ionizing radiation. United Nations Scientific Committee on the Effects of Atomic Radiation, New York
- UN (2001) Hereditary effects of radiation. United Nations Scientific Committee on the Effects of Atomic Radiation, New York
- Upton AC, Kimball RF (1967) Radiation biology. In: Morgan KZ, Turner JE (eds) Principles of radiation protection. Wiley, New York
- USNRC (1991) Standards for protection against radiation, Title 10, Code of Federal Regulations, Part 20, 56FR23360. U.S. Nuclear Regulatory Commission, Washington, DC
- Vogel F, Motulsky AG (1979) Human genetics. Springer, Berlin
- Wald N (1967) Evaluation of human exposure data. In: Morgan KZ, Turner JE (eds) Principles of radiation protection, Wiley, New York
- Walsh RL (1989) Spin-dependent calculation of fission neutron spectra and fission spectrum integrals for six fissioning systems. *Nucl Sci Eng* 102:119–133
- Wang X, Faw RE (1995) Transmission of neutrons and secondary gamma rays through concrete slabs. *Radiat Protect Dosimetry* 60:213–222
- Weber DA, Eckerman KF, Dillman LT, Ryman JC (1989) MIRD: radionuclide data and decay schemes. Society of Nuclear Medicine, New York
- Weise H-P (1994) Neutron leakage from the entrance maze of medical electron accelerators. In: Proceedings of the 8th international conference on radiation shielding, American Nuclear Society, La Grange Park, IL, p 934
- Wyard SJ (1952) Intensity distribution of Bremsstrahlung from beta rays. *Proc Phys Soc London* A65:377
- Wyckoff JM, Chilton AB (1973) Dose due to practical neutron energy distributions incident on concrete shielding slabs. In: Proceedings of the 3rd international congress IRPA, Washington, DC, p 694
- Zoller LK (1964) Fast-neutron removal cross sections. *Nucleonics* 22:128